Computational modelling of cellular mechanics and signalling in intramyocardial biomaterial injectates for myocardial infarction therapies

Yawovi Dodzi Motchon

Thesis presented for the degree of

DOCTOR OF PHILOSOPHY

In the Department of Human Biology

UNIVERSITY OF CAPE TOWN

June 2022

Supervisors

Professor Thomas Franz

Department of Human Biology, University of Cape Town

Associate Professor Neil H Davies

Department of Surgery, University of Cape Town

Dr Kevin Sack

Department of Human Biology, University of Cape Town

Declaration

I, Yawovi Dodzi Motchon, declare that this thesis titled "Computational modelling of cellular mechanics and signalling in intramyocardial biomaterial injectates for myocardial infarction therapies" and the work presented in it are my own, unless stated otherwise in the thesis (see section 2.1.1). I confirm that this work was done wholly or mainly while in candidature for a doctoral research degree at this University. I know the meaning of plagiarism and declare that all the work in the document, save for that which is properly acknowledged, is my own. I confirm that neither the whole work nor any part of it is being or is to be submitted for another degree in this or any other university. Where I have consulted the published work of others or included collaborative work, this is always clearly attributed.

Yawovi Dodzi Motchon

Acknowledgements

Firstly, I would like to thank my supervisor Professor Thomas Franz for his invaluable advice and guidance through this research. Tom, thank you for offering me this opportunity and giving me the chance to achieve this PhD. I am incredibly grateful for the attention and the trust you put in me during the whole research period. You made these stressful periods more enjoyable for me.

I am thoroughly grateful to my co-supervisor, Associate Professor Neil Davies, for the technical support provided when needed. Thank you, Neil, for you, for your guidance in cellular signalling and biochemical-related works.

I cannot fully express my gratitude to my second co-supervisor, Dr Kevin Sack, for his handy advice and helps. Kevin, you always assisted with finite element issues, cardiac computational modelling problems, even the basics.

My gratitude goes to my colleagues and friends in the Mechanobiology team at the University of Cape Town. I would also like to thank all the students and staff members in the division of Biomedical Engineering.

I am fortunate to have the full support of my parents, essentially my father, Yawovi Kaliowofe Motchon, who remains a model for me. The only regret I have is that of not being able to present this degree to my mum Mawulawoe Tsronu who passed away a few weeks before I submitted my PhD. She never stopped encouraging me through this journey. For their warm supports, I am grateful to my brothers and sisters.

I would also like to thank my friend of every day, Dr Folly Serge Tomety, who was always there for me since our first years at Université de Lomé in Togo. Thank you, Dr Mesmin Awo, for your encouraging messages when things were uncertain.

I would also like to thank all AIMS alumni at the division of Biomedical Engineering. Riham Ahmed, Juliet Nagawa, John Nchejane, Dr Jean-Rassaire Fouefack, Nicolas Nbonsou Tegang.

My biggest gratitude goes to my beloved wife, Abide Pinewayi, who took the biggest part of the load. You were always present and encouraging despite the distance, the stresses, or the struggles we went through.

This research would not have been possible without the financial support of Dr. Leopold und Carmen Ellinger Stiftung, Germany.

Abstract

Intramyocardial delivery of biomaterials and stem cells is a promising concept to treat acute myocardial infarction. The delivered biomaterials provide mechanical support, attenuating wall thinning and elevated stress levels in the infarct region, whereas the stem cells induce cardioprotective effects through paracrine signalling. However, the mechanical and biochemical mechanisms, and their interactions, underlying the therapeutic benefits require further clarification towards optimisation and personalising the treatment approach.

A subject-specific biventricular finite element model of a rat heart with left ventricular infarct and acellular biomaterial injectate was developed from μCT data. The model featured the *in situ* dispersion of the biomaterial delivered one week after the infarction. A finite element sub-model represented a mid-wall equatorial geometry (748 μm x 748 μm x 772 μm) from the infarct region. The sub-model captured the microstructure of the infarcted myocardium, biomaterial injectate and nine cells numerically seeded at random locations in the injectate domain. The spherical cells with an outer diameter of 65 μm represented stem cells therapeutically delivered with the biomaterial. The two finite element models were coupled to quantify the deformation of the injected stem cells in the infarcted heart during a cardiac cycle. Finally, a mathematical relationship of cellular strain and TGF-β expression was developed using experimental data from the literature and a single-cell finite element model.

The effect of the injectate stiffness on deformation and TGF-β expression in the therapeutically delivered stem cells was determined with parametric simulations varying the elastic modulus of the biomaterial from E_{inj} = 4.1 to 405,900 kPa. The strain range and strain-induced TGF-β expression in the therapeutic stem cells during a cardiac cycle increased initially with increasing injectate stiffness (from E_{inj} = 4.1 to 7.4 kPa) and decreased as the injectate stiffness was increased further. The stem cell's mechanics and TGF-β expression were more sensitive to changes in the injectate stiffness for softer biomaterials ($E_{inj} \leq$ 738 kPa) than for stiffer biomaterials.

The cardioprotective or tissue-regenerative signalling of delivered stem cells in the infarcted heart can be tailored by varying the *in situ* mechanical properties of soft deliverable biomaterials. The results indicate that the strain and TGF-β expression of the stem cells due to mechanical activity of the infarcted heart was largest when the elastic modulus of the injectate matched that of the cells, and both an increase and decrease of the injectate modulus led to a decrease in the cellular strain and TGF-β expression. This relationship can provide flexibility for multi-objective optimising the injectate stiffness, also taking into account wall mechanics and function of the infarcted left ventricle. The developed computational and mathematical models provide a framework to expand the investigations into biomaterial and cell injections therapy.

Table of Contents

List of Figures

List of Tables

Abbreviations

Abbreviations	Definition
2D	Two-dimensional
3D	Three-dimensional
AFM	Atomic force microscopy
BMC	Bone marrow-derived stem cells
BMMSC	Bone marrow mesenchymal stem cells
BV	Biventricular
CT	Computed thomography
CVD	Cardiovascular disease
DNA	Deoxyribonucleic acid
DT-MRI	Diffusion tensor magnetic resonance imaging
EC	Endothelial cell
ECM	Extracellular matrix
ED	End-diastole, end-diastolic
EDPVR	End-diastolic pressure-volume relationship
EF	Ejection fraction
ES	End-systole, end-systolic
ESPVR	End-systolic pressure-volume relationship
FE	Finite element
FEM	Finite element model
FGF	Fibroblast growth factor
GF	Growth factor
IQR	Interquartile range

LV	Left ventricle, left ventricular
LVAD	Left ventricular assist device
LVEF	Left ventricular ejection fraction
MMP	Matrix metalloproteinases
MRI	Magnetic resonance imaging
MSC	Mesenchymal stem cell
PCL	Polycaprolactone
PEG	Polyethylene glycol
PEUU	Polyester-urethane-urea
PV	Pressure-volume
Q	Quartile
Q_1	First quartile
Q_3	Third quartile
RNA	Ribonucleic acid
RV	Right ventricle, right ventricular
TGF-β	Transforming growth factor-beta
V	Volume
VA	Volume averaged
VEGF	Vascular endothelial growth factor
VEGFR2	Vascular endothelial growth factor receptor 2
μCT	Micro-computed thomography

Nomenclature

Symbol	Description
a	Material parameter, dimension of stress
a_{fs}	Material parameter defining coupling from in the fibre and sheet directions, with a dimension of stress
a_i	Material parameter, defined for i = f and s in the fibre and sheet directions, respectively, with stress dimension
B	Governs the shape of peak isometric tension-sarcomere length relation
b	Dimensionless material parameter in Holzapfel model
b_{fs}	Material parameter defining coupling from in the fibre and sheet directions, dimensionless
b_i	Material parameter, defined for i = f and s in the fibre and sheet directions, respectively, dimensionless
C_{10}	Coefficient used in Abaqus to describe the material stiffness in a Neo-Hookean strain energy density function
Ca_0	Peak intracellular calcium concentration
D_1	Parameter for elastic materials defining the compressibility of the material
E	Elastic modulus
ECa_{50}	Length-dependent calcium sensitivity
H	Parameter to define the pathological degree of the tissue
I_{4f}	Transversely isotropic invariant in the fibre direction
I_{4s}	Transversely isotropic invariant in the sheet direction
I_{8fs}	Orthotropic invariant from coupling in fibre and sheet direction
I_i	Isotropic invariants in principal directions
J	Measures the volume change of compressible materials

P	Parameter scaling the isotropic response of the diseased tissue
T	Stress tensor
$T^{(a)}$	Active stress tensor
$T^{(p)}$	Passive stress tensor
u_c	Unit vector in the circumferential direction
u_l	Unit vector in the longitudinal direction
W	Strain energy density function
α_h	Helix angle
α_t	Transverse angle
ε_{Cell}	Cell strain
ε_{Sub}	Substrate strain
κ	Bulk modulus
λ	Stretch
ν	Poisson's ratio
σ	Stress

Chapter 1 Introduction and background

1.1 Problem identification

Cardiovascular disease (CVD) is the leading cause of death worldwide. About 17.3 million individuals are concerned per year globally (Mendis *et al.* 2011). The current trends predict an increase of CVD related deaths from 17.5 million (i.e. 31% of global deaths) in 2012 to 22.2 million by 2030, representing an increase of 26.9%. Alarmingly, in the working-age population of low-and-middle incoming countries, including South Africa, the rate of people affected is becoming considerably high (Finegold *et al.* 2013, Opie and Mayosi 2005). Unfortunately, access to healthcare facilities in most sub-Saharan countries is not affordable for most populations. This situation affects the global economy and therefore influences the social cohesion in the communities.

Myocardial infarction (MI) originates from coronary occlusion, causing a lack of oxygenated blood supply to a specific myocardial region. This absence of oxygen results in cardiac cell death. The inflammatory response induced by the cardiac cell death initiates collagen production that gradually replaces the contractile tissue. In the long term, the cardiomyocyte death is followed by a scar formation, causing excessive load to the heart, creating dysfunctions and can lead to heart attacks. To date, there is no effective and controlled treatment for MI. However, temporary solutions have been developed, and many others are still under investigation.

Current treatments include reperfusion (drugs administration or surgery), mechanical device assistance (e.g. left ventricle assist device) and heart transplantation. The main objective of these treatments is to help arteries for dilatation, assist the left ventricle in pumping blood, or replace the damaged heart. New therapies based on polymer or biomaterial injections and

therapeutic cell delivery are emerging in research as alternatives for current treatments. Clinical studies showed promising results with the use of alginate-based biomaterial. Several studies have shown the mechanical beneficial effects of biomaterial injectates (particularly hydrogels) on the adverse ventricular remodelling that follows the post-MI inflammatory response (Christman *et al.* 2004a, Fan *et al.* 2019, Johnson and Christman 2013, Silveira-Filho *et al.* 2021). Other studies proposed the implantation of cardiac or stem cells to the impaired heart. More importantly, several investigations revealed the multipotent abilities of stem cells, including the differentiation into cardiac-like cells (Beltrami *et al.* 2003, Guo *et al.* 2011, Robinton and Daley 2012). Enhanced neovascularisation and angiogenesis were observed with reduced myocardiocyte deaths following intravenously or intramyocardially injected stem cells through paracrine or autocrine signalling (Kocher *et al.* 2001, Shudo *et al.* 2013).

Despite the advances and the considerable number of studies dedicated to cellular and biomaterial therapies, many questions remain unanswered. The mechanisms underlining the cardioprotective impact of injectates and cell-based therapies remain unclear.

1.2 Biomaterial therapies for myocardial infarction

1.2.1 Biomaterial injection: pre-clinical research studies

Biomaterials have gained increasing attention in research as an alternative for traditional treatments for myocardial infarction over the past two decades. The employed biomaterials are polymer-based gels that are biocompatible and can be loaded with drugs or therapeutic cells.

Christman *et al.* (2004a) introduced the possible use of biomaterial as a treatment for MI to attenuate the infarct expansion due to the adverse remodelling. A fibrin-based biomaterial was developed to prevent infarct wall thinning and improve cardiac functions after MI. Several studies followed and used various biomaterials, including synthetic and natural gels (see Table 1 and Table 2).

Natural biomaterial

Natural biomaterials present advantages because they are biocompatible, highly reactive with resident cells or eventual therapeutic cells, and biodegradable. Moreover, natural biomaterials can react effectively with cell membrane receptors, promoting cell activity (e.g. collagen or gelatine polymers have strong interaction with membrane proteins for adhesion). These characteristics are essential for resident and delivered cells involved in MI therapies. Many extracellular matrix components can be used in the composition of natural biomaterials, including collagen, fibrin, gelatin, keratin, fibroin and sericin (Gasperini *et al.* 2014, Saludas *et al.* 2017, Toh and Loh 2014).

Biomaterials can also be loaded with additional regenerative growth factors to promote vascularisation or angiogenesis (Blatchley and Gerecht 2015). Despite the advantageous characteristics of natural biomaterials, they present some drawbacks, such as the complexity in manufacturing. This complexity represents a limitation in large scale production. Furthermore, the use of naturally-based components limits the ability to tune the mechanical properties of the biomaterial (Sepantafar *et al.* 2016).

Synthetic biomaterials

Synthetic biomaterials are developed from artificial proteins, and their cardioprotective capabilities have been demonstrated in several studies. They have a higher production potential compared to natural biomaterials. Their mechanical properties are well controlled compared to natural biomaterials (Sepantafar *et al.* 2016). Due to their chemical composition, synthetic biomaterials have less bioactivity and biocompatibility compared to natural biomaterials. Dobner *et al.* (2009) injected a synthetic non-degradable polyethylene glycol (PEG) hydrogel intramyocardially in a rat heart infarcted region. They reported a left ventricle post-infarct dilation for the first time. Synthetic biomaterials have been shown to improve LV wall properties (i.e. alter the wall thinning and reduce the stress) and showed their importance in heart tissue structural repairing (Christman *et al.* 2004a).

Table 1. Mechanical properties of cardiac tissue and injectable biomaterials (Sepantafar *et al.* 2016).

Material	**Stiffness (Pa)**	**References**
Normal human cardiac muscle	50,000	(Omens 1998)
Failed human cardiac muscle	200,000 -300,000	(Omens 1998)
Fibrin	50	(Semler *et al.* 2000, Urech *et al.* 2005)
Matrigel	30-120	(Semler *et al.* 2000)
Collagen (type I)	20-80	(Barocas *et al.* 1995)
PNIPAm	100-400	(Kim and Healy 2003)
Alginate	100-6,000	(Stokke *et al.* 2000)
PEG	1,000-3,000	(Rizzi *et al.* 2006)

PNIPAm: poly(N-isopropyl acryl amide); PEG: poly(ethylene glycol).

The biomaterial mechanical and biochemical properties are essential for optimising MI therapy. Therefore, synthetic polymers are often added to the naturally-based biomaterials to increase the ability to tune the mechanical properties while keeping all the biochemical characteristics of the natural biomaterial (Ravichandran *et al.* 2012, Sepantafar *et al.* 2016). Several studies used biomaterials that combine synthetic polymers with well-tunable mechanical properties and components based on extracellular matrix (ECM) with biological and physiological advantages (Krupnick *et al.* 2002, Ravichandran *et al.* 2011, Stankus *et al.* 2004). Stankus *et al.* (2004) reported enhancement in smooth muscle cell adhesion and mechanical properties when injecting polyester-urethane-urea (PEUU) polymer combined with collagen I compared to injecting collagen I only. A hydrogel-based scaffold consisting of polytetrafluoroethylene, polylactide mesh, and collagen (type I and IV) was successfully transplanted in a myocardial-damaged (congenital heart) rat heart left ventricle (Krupnick *et al.* 2002). The authors demonstrated that this biomaterial increased end-systolic and end-diastolic volume compared to animals without scaffold implantation.

Biomaterial injections are known to alter the adverse ventricular remodelling and prevent infarct expansion. A decrease in wall stress and a significant slowdown in the LV wall thinning have mainly been observed following biomaterial injection. Several biomaterials have been developed in pre-clinical studies and shown beneficial effects and promising results for therapeutic applications.

Alginate hydrogels serving as scaffolds contribute to wall stress reduction and prevent further LV expansion (Di Franco *et al.* 2018, Leor *et al.* 2009). Eleven patients were enrolled in a study with advanced heart failure (New York heart association class 3, 4 criteria) to investigate the feasibility and the safety of administrating alginate-based biomaterial (Algisyl-LVR) (Lee *et al.* 2015). The feasibility and safety were demonstrated for LV augmentation through open-heart surgery. Another alginate-based biomaterial was tested in the AUGMENT-HF clinical trial to compare the Algisyl-LVR therapy and optimal evidence-based medical devices (Anker *et al.* 2015, Mann *et al.* 2016). The use of Algisyl-LVR on 78 patients with advanced heart failure demonstrated continuous long-term beneficial effects on LV augmentation (Mann *et al.* 2016).

Singelyn *et al.* (2009) developed an ECM biomaterial derived from porcine tissue. This naturally derived biomaterial has demonstrated LV remodelling mitigation and reduced (EF) in a rodent model. The results of pre-clinical studies on animals encouraged clinical trials on humans. The safety and feasibility of an ECM-based biomaterial (VentriGel) were evaluated with patients with LVEF between 25% and 45% (Traverse *et al.* 2019).

Table 2. Summary of biomaterial injectates and the outcomes (Sepantafar *et al.* 2016)

Biomaterial injectate	**Outcomes**
Fibrin	Better results in FS and wall thickness (Christman *et al.* 2004b), tissue regeneration and enhanced neo-vascularisation (Ryu *et al.* 2005), reduced myocardial scar formation and increased angiogenesis (Atluri *et al.* 2014), improved cell viability, cardiac differentiation (Guo *et al.* 2011)
Matrigel	Enhance result in FS and wall thickness, better G/I ratio and wall thinning (Kofidis *et al.* 2004, Kofidis *et al.* 2005)
Chitosan	Better results in G/I ratio, FS, EF, wall thickness, infarct size and angiogenesis (Lu *et al.* 2008), improvement in the viability and engrafted cells, reduced infarct size and improved heart functions, wall thickness and angiogenesis (Liu *et al.* 2012), enhancement in the survival and engrafted ADSCs, decrease infarct size and fibrotic area, improved heart functions, wall thickness and angiogenesis (Wang *et al.* 2014)
SIS-Extracellular matrix	Non-significant difference between SIS-only and cell-SIS injections was reported (Toeg *et al.* 2013)
OPF	Better G/I ratio, reduced infarct size and collagen deposition, improved heart functions, and decreased MMP-2 and MMP-9 expression (Wang *et al.* 2012)
PEG-PCL-PEG	LV remodelling and dilation prevention, improvement in local diastolic and systolic functions (Chen *et al.* 2014a)
Self-assembling peptides nanofibers	Reduced scar formation and improvement in cell retention, angiogenesis and cardiac function (Lin *et al.* 2010)
RGD modified self-assembling peptide	Reduced fibrosis ratio and improved cell engraftment, EF and FS (Ban *et al.* 2014)
Col-SH and OAC-PEG-OAC	Improved wall thickness, EF, vessel density and less infarct size (Xu *et al.* 2015)
Collagen-alginate	A perceptibly improved cardiac function (Zhang *et al.* 2006)

FS: fractional shortening; G/I: graft/infarct; EF: ejection fraction; LV: left ventricle; SIS: small intestinal submucosa; OPF: oligo[poly(ethylene glycol) fumarate]; PEG–PCL–PEG: poly(ethylene glycol)–poly(caprolactone)–poly(ethylene glycol); Col-SH: thiolated collagen; OAC: oligo(acryloyl carbonate)

1.2.2 Computational modelling of biomaterial mechanics for myocardial infarction treatment

The beneficial effects of biomaterials for the treatment of MI have been demonstrated in many studies (Christman *et al.* 2004b, Dobner *et al.* 2009, Kadner *et al.* 2012, Leor *et al.* 2009, Plotkin *et al.* 2014, Sabbah *et al.* 2013). Many studies addressing the mechanical, biological, or biochemical mechanisms involved in biomaterial therapies for MI are experimentally based. One of the common blockages in experiments is the cost of resources and the invasive aspect of the experimental protocols. Computational modelling appeared as an alternative or a supplementary tool to investigate aspects that are not easily accessible in experimental and *in vivo* studies. Therefore, the mechanical impact of therapeutic biomaterial injections in infarcted hearts has been investigated considerably with computational models (Kortsmit *et al.* 2013a, Wall *et al.* 2006, Wang *et al.* 2017, Wenk *et al.* 2011, Wenk *et al.* 2009, Wise *et al.* 2016).

Finite element-based methods for large non-linear elastic deformations were used to study the impact of biomaterial injections for the treatment of MI. Many parameters were tested, including the material stiffness, the biomaterial delivery location, the injection volume, and the injection pattern (Cai *et al.* 2017, Kadner *et al.* 2012, Kortsmit *et al.* 2013b, Wall *et al.* 2006, Wenk *et al.* 2009).

Wall *et al.* (2006) reported a reduction in the wall stress, affecting the ESPVR, EDPVR and EF using a FE model where a non-contractile injected biomaterial was implemented in the LV wall of an ovine heart geometry by modifying a few nodes in the mesh. The results obtained were dependant on the volume, the location, and the material stiffness.

The pattern of the injectate is not always controlled -mainly for post solidified materials- following the injection (morphology and dispersion). Wang *et al.* (2017) have shown the impact of injectate stiffness and volume on myofiber stress and LV wall thickness. Their findings suggest that a stiffer material with a higher volume contributes to the LV myofibre stress reduction and wall thickness increase, essential to alter the remodelling. Computational models can help optimise the pattern of injections (Wenk *et al.* 2009). Wise *et al.* (2016)

identified a threshold volume of injected biomaterial from which the treatment efficacy is reduced.

1.3 Cellular therapies for myocardial infarction

1.3.1 Potential of cells and stem cells in regenerative therapies

Cell-based therapies have gained increasing interest during the last decades. In general, cell therapy can be considered as a strategy, using autologous or allogeneic cells to replace, repair or enhance biological functions in damaged tissues or organs (Bordignon *et al.* 1999). The development of treatments based on stem cell delivery is motivated by their capability to differentiate into several cell types and induce regenerative signalling (Beltrami *et al.* 2003, Eschenhagen *et al.* 2017, Fernández-Avilés *et al.* 2017, Kikuchi and Poss 2012). |Stem cells represent additional therapeutic potential through their ability to inhibit inflammation or cell death, improve angiogenesis, and differentiate (Mousaei Ghasroldasht *et al.* 2022).

The potential of stem cells for use in MI has been demonstrated in numerous studies with different cell types (Atluri *et al.* 2014, Beltrami *et al.* 2003, Chen *et al.* 2014b, Nishikawa *et al.* 2008). Despite the advanced methods developed, the implementation of cells in MI therapy in clinical studies results in several challenges, including cell delivery, retention, or proliferation (Strauer and Steinhoff 2011). For example, Atluri *et al.* (2014) proposed a hydrogel-based approach consisting of endothelial progenitor cell-mediated therapy to enhance cell delivery, cell retention, vasculogenesis, and preservation of ischemic myocardial structure and function. This approach may provide tools to prevent issues related to cell dispersion and engraftment observed in previous cell-based clinical trials.

1.3.2 Cell delivery for myocardial infarction therapy

The transplantation of stem cells to the myocardium with injectable biomaterials has gained substantial interest in MI therapy. It is a recent promising approach in which the delivered cells are expected to promote beneficial regenerative reactions in the impaired tissue. Stem cells have gained considerable attention because they can differentiate into several cell types,

including cardiac-like cells and endothelial cells (EC), necessary for a new vascularisation and heart function recovery. Stem cell therapies have been considerably investigated in the early 2000s as a treatment for MI and have shown promising results. Several animal studies support the hypothesis of the beneficial effect observed in cell therapies driven by paracrine effects (Duran *et al.* 2013, Gao *et al.* 2015, Nguyen *et al.* 2016, Strauer and Steinhoff 2011, Tomita *et al.* 1999, Wang *et al.* 2018).

Mesenchymal stem cells can differentiate into adipocytes, chondrocytes and osteogenic cells in favourable conditions (Pittenger *et al.* 1999).

The main parameters that need to be considered for cell therapy for an infarcted heart include:

- The delivery route: Infusion or direct injection to the heart. The choice of a suitable mode of delivery of therapeutic cells is determinant for cell retention post-treatment (Davies *et al.* 2016).
- The source of stem cells: the reactivity of the cells depends on the region where they have been harvested.
- The environment in which the delivered cells will reside: For example, a material serving as a scaffold for transplanted cells into the myocardium or the biomaterial for injection constitute the direct environment with which the cell interacts and needs to have the optimised properties for cell retention and survival.
- The bio-reactivity of the therapeutic cells: This is essential for cell signalling and cell biocompatibilities.

Several studies have been conducted in animal models using allogeneic or autologous stem cells (Strauer *et al.* 2003, Strauer and Steinhoff 2011, Thavapalachandran *et al.* 2021, Wollert *et al.* 2004, Wu *et al.* 2021). The allogeneic stem cells are collected from a different subject/patient and include umbilical cord-derived stem cells, foetal cardiomyocytes, and embryonic mesenchymal stem cells. They come from donors and have poor outcomes for tissue engineering-based therapies because of their reduced compatibility or immune responses and high rejections rate. Autologous stem cells are harvested from the subject to be treated and include skeletal myoblast, adipose-derived stem cells, resident cardiac stem cells and bone marrow-derived stem cells. Numerous studies demonstrated the beneficial effects of adult stem

cells on MI and the possibility to export these results to a clinical trial. Chen *et al.* (2014a) demonstrated the feasibility of using bone marrow mesenchymal stem cells incorporated in a hydrogel on rabbit models following MI. A study on rats by Wang *et al.* (2018) revealed an increase in the expression of endothelial related proteins, improved ejection fraction, reduced infarct size and a high vessel density by using a biochemically and genetically activated hydrogel loaded with adipose-derived stem cells. Intramyocardial transplantation of bone marrow-derived stem cells in infarcted rat heart has shown improved angiogenesis and myocardial functions and successful differentiation into cardiac-like cells (*in vitro* and *in vivo*) within the infarcted region of the myocardium (Tomita *et al.* 1999). More importantly, the myocyte-like phenotypes were only observed for bone marrow-derived stem cells cultured in a 5-azacytidine medium. The success of research works on stem cells as a potential therapy for myocardial infarction has encouraged the development of stem cell-based clinical trials.

Several clinical trials employed autologous or allogeneic stem cells for MI treatment. The therapeutic cells were delivered intramyocardially, intravenously or intracoronary to the impaired heart. In most of the trials, bone marrow-derived stem cells were used to determine the safety and feasibility (Hare *et al.* 2012, Hare *et al.* 2009, Strauer *et al.* 2003, Strauer and Steinhoff 2011).

The collection of stem cells from the bone marrow or selected MSCs were used in cell therapy. Strauer and Steinhoff (2011) tested the efficacy and safety of human mesenchymal stem cells in patients with myocardial infarction. They observed improvements in the heart functions after six months of follow-up.

A comparative study by Hare *et al.* (2012) assessed the viability of allogeneic and autologous bone-marrow-derived MSC in patients with ischemic cardiomyopathy. The injection of MSC, either autologous or allogeneic, showed positive effects on ventricular remodelling, the functional capacity of the heart, and patients life's quality.

Despite the successfully confirmed viability, safety, and efficacy of stem cell use for MI treatments, some studies reported different or poor outcomes compared to pre-clinical studies (Strauer and Steinhoff 2011). The possible reasons for these unexpected results may be (i) from the stem cells (e.g. cell preparation, non-standardised method for cell delivery) or (ii)

dependent on the methods for evaluating the heart functions. Moreover, the underlying mechanisms governing the action of therapeutic stem cells in the infarcted heart are still unclear.

1.3.3 Cell signalling and cardioprotective effects in cellular biomaterial injectates for myocardial infarction therapy

Biological systems respond to the environment with induced biochemical processes, including cellular and molecular signalling through chemical reactions. Signalling is a set of reactions activated by biochemical or biophysical cues in a biological system, leading to significant changes at a macroscopic scale. Cells are sensitive to external factors such as mechanical changes (e.g. mechanical strain) or chemical concentrations gradients (calcium, iron, glucose, cytokines). The cellular responses to external cues are differentiation, mitosis, proliferation, migration, gene expression, gene regulation and apoptosis. Stem cells are the most used in tissue engineering and cell therapies due to their multipotent capabilities. The cellular responses to mechanical or biochemical inputs have been widely investigated.

Cell-cell communication is crucial in the cardioprotective effect of therapeutic stem cells for MI treatment. During cellular communication, proteins are released in the medium by one cell and get attached to receptors on the membrane of the same or neighbouring cell, respectively, through autocrine or paracrine effect. Various studies reported angiogenesis and neo-vascularisation responses (Duran *et al.* 2013, Zhao *et al.* 2016, Zheng *et al.* 2001).

Numerous studies in the earlier 2000s focused on the role of growth factors and several other cytokines in the cardioprotective effects observed in cell therapies for myocardial infarction, both in pre-clinical and clinical trials (Cassino *et al.* 2012, Zhao *et al.* 2016, Zheng *et al.* 2001). Hepatocyte growth factor (HGF), vascular endothelial growth factor (VEGF), transforming growth factor-beta (TGF-β), and basic fibroblast growth factor (bFGF) are examples of growth factors involved in angiogenesis. Combining HGF and umbilical cord mesenchymal stem cells (UC-MSC) enhanced angiogenesis, increased cell proliferation and reduced cardiac cell death (Zhao *et al.* 2016). TGF-β is known for regulating VEGF expression, which is a crucial growth factor for angiogenesis activation and new vessel formation. Many studies reported that

mechanical stimuli are essential in growth factors production and other proteins responsible for angiogenic phenotypes. For example, it is well established that *in vitro* cyclic stretching on stem cells results in increased growth factor production and improved cardiac activities (Bhang *et al.* 2010, Tian *et al.* 2016).

Mechanical stimuli in biological processes such as tissue growth or morphogenesis are well known. Once delivered, the therapeutic cells are subjected to mechanical stimuli from the deformations of the injectate generated by the heart activities. In response, the cells initiate biochemical reactions, which lead to paracrine or autocrine signalling. Zheng *et al.* (2001) reported a VEGF mRNA and protein concentration increase in cardiac cells with applied cyclic stretch. Additionally, they observed a 2.5-fold increase of TGF-β one hour post-stretching. More importantly, the neutralisation of TGF-β inhibited the stretch-induced production of VEGF, confirming the mediation role played by TGF-β in VEGF production. Several studies further demonstrated the link between the growth factor secretion and the beneficial effects on the infarcted heart, including fractional shortening, fractional area change (Cassino *et al.* 2012, Rashid *et al.* 2021, Zhao *et al.* 2016).

By applying 18% cyclic stretch at 0.42 Hz to *in vitro* cultured ECs, Tian *et al.* (2016) observed increased cell permeability mediated by VEGF receptor-2 (VEGFR2). The mechanism whereby VEGFR2 activation mediates the pathologically induced ECs permeability was also demonstrated. Cassino *et al.* (2012) reported increasing VEGF secretion *in vivo* by applying 10% equibiaxial stretch to MSC. Furthermore, they reported improving systolic cardiac function (fractional shortening, fractional area change) and reduced scar tissue area.

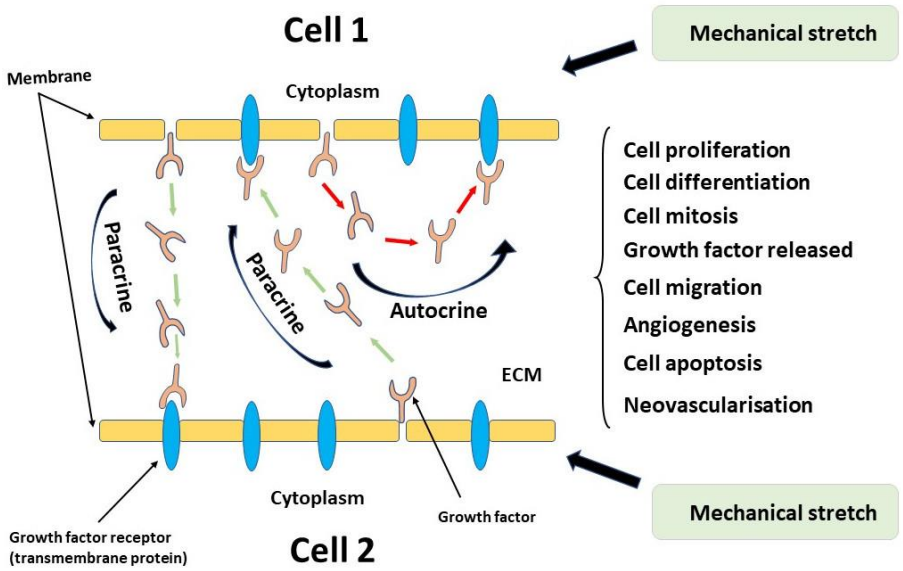

Figure 1. Cell signalling induced by mechanical stimuli. The growth factor released by cell 1 is attached to the receptor in cell 2 and vice versa (paracrine). Additionally, cell 1 releases a growth factor that binds to another of its receptors (autocrine). A cascade of reactions is initiated from the membrane through the cytoplasm to the nucleus, where gene expression is triggered, resulting in different cellular responses (cell proliferation, differentiation, mitosis, apoptosis, initiation of angiogenesis, growth factor production, or new vessel formation).

1.4 Computational modelling of cardiac tissue mechanics

Cardiac tissue mechanics can be assessed through experimental testing or theoretical predictions. The mechanical characterisation of materials uses experiments that apply displacement loads on a sample and record the material response. The standard way to represent material behaviour from this experiment is the strain-stress graph, which allows for determining the material mechanical properties. The theoretical approach for material characterisation uses a mathematical framework to predict the myocardium's responses to mechanical stimuli. The mathematical implementation can be based on analytical or numerical models. The development of computational models for cardiac tissue mechanics includes the consideration of heart geometry, constitutive equations and finite element analysis.

1.4.1 Geometries development

The first step in developing a finite element (FE) model is to define the domain. In a 3D problem, the domain consists of a spatial region delimited by boundary surfaces. In cardiac modelling, the domain can be defined using a mathematical representation of the boundary surfaces or reconstructed from images data (e.g. MRI or DT-MRI, µCT, ultrasounds, confocal images).

The first attempts to implement heart functions in a computational model used analytical representations, consisting of a mathematical formulation of the heart surfaces. The simplest geometry of the LV is two parallels parametric surfaces (endocardial and epicardial surfaces). The to spheroid approach was used to represent the endocardial or epicardial surfaces in the LV model for simplified geometries, see Eqn. (1.1) (Dieudonné 1969).

$$\frac{x^2}{a^2} + \frac{y^2}{b^2} + \frac{z^2}{c^2} \tag{1.1}$$

where a, b and c are parameters governing the morphology of the surface.

Nielsen et al. (1991) proposed a truncated biventricular geometry for the first time based on a mathematical formulation. The model described the two ventricles and included the myocardial fibre orientation.

The current increasing capacity of computers allows the reconstruction of 3D geometries from imaging data. Advances in imaging technologies also permit reconstructing a whole heart geometry, including right and left ventricle, in a subject-specific heart model, primarily based on magnetic resonance imaging (MRI) and ultrasound. Many tools are designed to transform the raw image data into 3D geometries. The 3D reconstructed geometries are used to create a domain representing the heart where the FE models and the heart tissue mechanics will be implemented. Several models are developed from MRI, CT scan images in porcine, human or rat models (Cai *et al.* 2017, Kortsmit *et al.* 2013b, Sack *et al.* 2018, Sack *et al.* 2016, Wall *et al.* 2006).

1.4.2 Constitutive modelling of cardiac tissue in the context of an infarcted treated heart

Biological tissues can respond to external loads and mechanical changes like any other material. However, the internal energy-driven activities in living cells, the main constituent of tissues, add complexity to constructing computational or mathematical models for predictions. Constitutive modelling is a mathematical formulation based on continuum mechanics theories that describe the material properties and predicts stresses and deformations within the material. These techniques help the theoretical representation and understanding of organ functions and, more importantly, quantifying parameters that cannot be assessed experimentally. Finite element methods are used for implementing the constitutive equations into a discretised numerical problem.

Materials can be described with viscous, elastic (linear or non-linear) or viscoelastic mechanical properties depending on the characteristics of their responses to mechanical inputs. The material response depends on the material's chemical or molecular composition. Biological tissues consist of cells aligned in many configurations, including layers (e.g. connective tissues) and a mixture of ECM (rich in collagen). The mechanics at a cellular level is mainly driven by microtubules and actin filaments and by myofibers in connective tissues, including the myocardium (Chagnon *et al.* 2015).

Advanced theoretical tools were developed in continuum mechanics and applied to biological tissues, including the myocardium (Humphrey 2003, Humphrey and Yin 1987, Pinto and Fung 1973). The deformations in the material are assessed through left and right Cauchy stress tensor **B** and **C**, respectively see Eqn. (1.2) and a deformation gradient variable **F**.

The relationship between deformations and stress describing the material behaviour is represented with a simple linear equation for pure elastic materials (e.g. Hooke's laws). For more complex materials, different approaches are introduced, including the strain energy density function (SEDF). The Cauchy stress tensor (which contains the stress values in different directions) depends on the strain energy density function and the deformation gradient variable (see Eqn. (1.3)).

$$C = F^T F, \qquad B = F F^T, \tag{1.2}$$

$$J\sigma = F \frac{\partial W}{\partial F}, \tag{1.3}$$

where W is the strain energy density function, σ is the Cauchy stress tensor and

$$J = \det F, \tag{1.4}$$

Several functions have been proposed for the strain energy density to describe different types of materials. Exponential and polynomial functions are commonly used to describe the hyperelastic responses in biological tissues, defining isotropic or anisotropic properties of biological soft tissues (Holzapfel and Ogden 2009, Humphrey 2003). Each function has a set of parameters determined through calibration using a tissue sample from uniaxial or biaxial experiments.

Due to their complexity, most biological tissues, including the myocardium, have a non-linear response to loads and are treated as hyperelastic material using a strain energy density approach.

Passive mechanical behaviour of the myocardium

The passive response in the myocardium is described with hyperelastic laws due to the non-linear responses to different loads. Additionally, the layered structure of myofibers within the myocardium introduces anisotropic behaviours.

Several constitutive models were developed for cardiac tissue. Two main types of strain energy density functions were usually utilised. Firstly, the isotropic non-linear material laws were adopted by Janz and Waldron (1978) in a simplified LV model developed to predict the LV stresses due to uniaxial stretches. Secondly, the exponential-based formulation was introduced later, considering the heart tissue's complexity and non-linearity.

Mechanical anisotropy, which is fundamental in the myocardium, was introduced to represent the myofibre and consider the ECM collagen structure (Holzapfel and Ogden 2009, Humphrey 2003, Yin *et al.* 1987). Several orthotropic and transversely isotropic models were used for the

myocardium based on exponential strain energy forms (Humphrey 2003, Humphrey and Yin 1987, Pinto and Fung 1973). Humphrey and Yin (1987) proposed a transversely isotropic strain energy function based on uniaxial and biaxial data and the heart's tissue structural composition. The strain energy density function is a combination of matrix and fibre contribution representing the two terms:

$$W = C\left(e^{b(I_1-3)} - 1\right) + A\left(e^{a(\alpha-3)^2} - 1\right), \tag{1.5}$$

Similarly, orthotropic models were proposed for soft tissue modelling, including the myocardium. One of the proposed models suitable for cardiac tissue was the Fung type. Costa *et al.* (2001) proposed a model based on biaxial tests:

$$W = \frac{1}{2}C(e^{Q} - 1), \tag{1.6}$$

with

$$Q = b_1E_{ff}^2 + b_2(E_{cc}^2 + E_{rr}^2 + 2E_{cr}E_{rc}) + 2b_3(E_{fc}E_{cf} + E_{fr}E_{rf}), \tag{1.7}$$

where b_i (I = 1, 2, 3) define the stiffness in the directions (fibre, sheet and sheet-normal), E_{ij} (i, j = 1, 2, 3)

Holzapfel and Ogden (2009) described a general strain energy density function considering three invariants in three different directions:

$$W = \frac{a}{2b}e^{b(I_1-3)} + \sum_{i=f,s}\frac{a_i}{2b_i}\left\{e^{b_i(I_{4i}-1)^2} - 1\right\} + \frac{a_{fs}}{2b_{fs}}\left\{e^{b_{fs}(I_{8fs})^2} - 1\right\}, \tag{1.8}$$

with the coefficients and parameters as defined in Table 3.

Experimental tests are performed to describe passive cardiac tissue responses and identify the shape and parameters in the strain energy density function. These tests consist of uniaxial, biaxial and shear loads (Omens *et al.* 1993, Sacks 2000, Sommer *et al.* 2015). In the passive response of the material, the experimental stress-strain data are fitted with the predicted relationship from the strain energy density function. In addition, the quadratic terms in the

exponents of the strain energy function (e.g. Fung-type function) in Eqs (1.5) - (1.8) must be positive definite to ensure the convexity necessary for FE simulations (Federico *et al.* 2008).

Active contraction of the myocardium

Current models use the sarcomere length, free calcium concentration measures during signal activation, and the active tension law to implement the active contraction in the heart. Guccione and Mcculloch (1993) developed the more efficient approach, where the previously cited parameters were considered, and the active tension is applied in the fibre direction.

The overall response of the myocardium during contraction is modelled by coupling the active tension with the passive response:

$$T = T^{(p)} + T^{(a)}, \tag{1.9}$$

where the active tension is proportional to:

$$T_0 = T_{max} \frac{Ca_0^2}{Ca_0^2 + ECa_{50}^2} C_t, \tag{1.10}$$

Mechanical behaviour of infarcted myocardium

The contraction in cardiac tissue is driven by the activity of cardiomyocytes, aligned into fibre layers. When MI occurs, many cardiac cells in the infarct region die and are replaced by fibrotic cells that produce collagen. The resulting infarcted myocardium is a non-contractile material whose mechanical properties depend on the injury stage (ischemia, necrosis, fibrosis or remodelling, and heart failure) (Baig *et al.* 1998, Costa *et al.* 2001, Holmes *et al.* 2005).

The mechanics of infarcted myocardium is driven by several parameters, including collagen content, collagen fibre alignment and cross-linking, and the number of remaining cardiac cells (Connelly *et al.* 1985, Fomovsky and Holmes 2010, Holmes *et al.* 2005). Computational modelling can significantly contribute to investigating mechanical changes in infarcted myocardium and the impact of an infarct on cardiac function. The mechanical properties of infarcted tissue change with the scar evolution and during the healing process (Fomovsky and Holmes 2010, Holmes *et al.* 2005). The non-contractile characteristics and the change in fibre

structure are key factors modifying the mechanical properties in the scar tissue (stiffness, contraction abilities).

The infarcted tissue is treated as a passive material with modifications in the anisotropic response (modifications in the fibre orientation) and increased stiffness (due to abnormal collagen level). A similar approach to healthy cardiac tissue modelling is used to model the infarcted tissue with modified parameters for stiffness (Guccione *et al.* 1993, Sun *et al.* 2009, Wenk *et al.* 2011).

In a model developed by Sack *et al.* (2018), a pathological scaling factor was introduced with a modification of the passive strain energy density function Eqn (1.8) to describe the pathological state of the damaged myocardium. New parameters were introduced considering the volume fraction of tissue health, and the active tension was turned to zero:

$$W = \frac{\bar{a}}{2b} e^{b(I_1-3)} + \sum_{i=f,s} \frac{\bar{a}_i}{2b_i} \{e^{b_i(I_{4i}-1)^2} - 1\} + \frac{\bar{a}_{fs}}{2b_{fs}} \{e^{b_{fs}(I_{8fs})^2} - 1\} \tag{1.11}$$

where $\bar{a}$, $\bar{a}_i$ with $i = (f, s)$ and $\bar{a}_{fs}$ govern healthy and pathological tissue homogenisation. A scalar parameter h defines the volume fraction of healthy tissue (Sack *et al.* 2018):

$$\bar{a_i} = a_i(h + (1 - h)p) \tag{1.12}$$

where $h \in [0, 1]$ define the pathological degree of the tissue and p scales the passive response according to pathology.

1.5 Experimental and computational cellular mechanics

1.5.1 Structural and mechanical properties of cells

Cell mechanical properties and their mechanical responses depend on their constituents. Understanding cellular mechanics at a single cell level is essential to predict and explain the tissue response to mechanical stimuli.

Cells are composed of three major parts that mainly contribute to cellular mechanics. The membrane is the envelope serving as a container to the internal part of the cell and plays an essential role in the communication with other cells and the surrounding environment (e.g. ECM). The nucleus is the central part of the cell (containing DNA) where gene expression and gene regulation occur. The cytoplasm is the intermediate region in the cell between the nucleus and the membrane and is made of different organelles and filamentous networks. Although the nucleus and membrane participate in cell mechanotransduction, the mechanical and structural contribution of the cytoplasm is considerably higher.

The cytoplasm comprises organelles (e.g. mitochondria, Golgi apparatus, endocardium reticulum, vacuoles, lysosomes), filamentous polymers (microtubules, actin filaments and intermediate filaments). The actin filament is a network of actins that is the primary structural component of the cytoskeleton. Intermediate filaments are intermediate structures between microtubules and actin filaments in size, stiffness, persistent length and flexibility (Rodriguez *et al.* 2013).

Cells have transmembrane proteins ensuring the adhesion and the junction between cells and ECM or other cells. These proteins allow the cell to establish tight junctions (mostly non-permeable junctions between cells), gap junctions (porous junctions which allow small proteins transportation) or anchoring junctions (plays structural functions by linking cells) (Rodriguez *et al.* 2013).

Cell mechanical properties are essential in building a computational model capable of predicting cell deformations or stress. There are generally two experimentally-based techniques to determine cell mechanical properties of cells, including force application techniques and force sensing techniques (Rodriguez *et al.* 2013).

Force application techniques measure cell responses to an external force and deduce a force-deformation relationship. The force application techniques include micropipette aspiration, atomic force microscopy, microneedle tools, optical tweezers, magnetic tweezers, cell compression, and cell stretching.

Several studies have used micropipettes aspiration in the earlier works dedicated to experimental investigations of cell mechanics. It is mainly used to determine elastic or viscoelastic mechanical properties in cells (Baaijens *et al.* 2005, Evans and Yeung 1989, Hochmuth 1993, Mitchison and Swann 1954, Trickey *et al.* 2006). The technique uses a force applied in a glass pipette to aspire part of the cell into the pipette. The mechanical property is then determined from the length of the part inside the pipette and the applied force.

AFM has gained considerable attention due to the simplicity and the high resolution achieved in the sample dimension and the force to be applied.

Cell stretching offers a possibility to assess mechanotransduction processes in cells (stretch-induced signalling, gene activities, ECM proteins recruitment) and help characterise the mechanical property simultaneously.

The force sensing technique includes traction force microscopy or cantilever sensing.

1.5.2 Constitutive and finite element modelling of cell

Cells shapes depend on the physical properties of their environment (Tee *et al.* 2011). In a 3D environment, most cells adopt a bulky configuration (example of a cell embedded in a therapeutic biomaterial injectate), whereas they tend to spread in a 2D environment with a flat shape.

The cell geometry can be simplified using idealised shapes, including spheres, half-sphere, disks or spheroids, depending on the topology or mechanical properties of the environment and the targeted cell function (Slomka and Gefen 2010, Slomka *et al.* 2009). More complex and realistic cell geometries can be developed from imaging techniques, including atomic force microscopy (AFM) (Darling *et al.* 2006), electronic microscopy, confocal microscopy or phase-contrast microscopy (Abdalrahman *et al.* 2017, Kohn *et al.* 2018, Saeed *et al.* 2016, Yamada *et al.* 2009).

The choice of imaging method depends on the purpose of the study and the cell size. For instance, atomic force microscopy plays a double role in (i) determining the mechanical properties of cells and (ii) revealing the cellular geometry. However, the technique is limited

to a global identification of the cell geometry and its mechanical properties without considering the cell components. In contrast, confocal microscopy highlights any region/component of interest in the cell (e.g. cytoplasm or nucleus).

Experimental techniques permit determining material properties necessary to implement a computational or mathematical study of cell mechanics. Cells mechanical responses are often complexes because of the internal active energy-driven reactions. Depending on the regime, the process, and the modelling scale, the viscoelastic, linear elastic, or hyperelastic descriptions are potential candidates to describe cell responses.

The hyperelastic description is commonly used in the context of large deformations and passive responses at the cellular scale. Jean *et al.* (2005) developed a finite element-based model to describe mechanotransduction pathways during endothelial cell rounding. Kohn *et al.* (2019) investigated a cellular focal adhesion by modelling a cell stretching experiment. The single-cell was treated as a hyperelastic isotropic material with a Neo-Hookean material law.

Depending on the time scale of the considered process, the active polymerisation and depolymerisation taking place within the cell can be considered.

Cell motility is modelled using different approaches, including the viscous or viscoelastic mechanical properties to represent polymerisation and depolymerisation in the cytoskeleton. Darling *et al.* (2006) used AFM to determine the elastic and viscoelastic property of chondrocytes, osteoblasts and adipocytes cells. They further showed that the primary differentiated cells have different mechanical properties than adult stem cells.

Based on the time scale and magnitude of deformations, cells and the different components are treated as pure viscous, viscoelastic or pure elastic materials. In the context of MI therapy, the cell is mainly treated as a 3D hyperelastic material with isotropic elastic Neo-Hookean responses (Gladilin *et al.* 2007) despite the heterogeneity provided by the different components (cytoplasm, nucleus or membrane). Saeed *et al.* (2016) developed a FE model of cell mechanics, which provide information on a single MSC mechanical behaviour. Furthermore, they showed the feasibility of using simple optical microscopy to construct a 3D cell geometry.

Despite extensive research dedicated to the impact of cell-based injection treatments, no computational study has investigated in detail the underlining mechanism from a molecular point of view or a macroscale level.

1.6 Limitations

The beneficial effects of biomaterial in the treatment of MI have been demonstrated in many studies. Over the last two decades, the knowledge about the impact of biomaterial injection on an impaired heart has gained considerable advancement, either computationally or experimentally. However, despite these advances, many questions remain open for future investigations. To date, few studies have examined the biological or biochemical aspect of the biomaterial injections therapy for MI coupled with computational modelling. Moreover, no computational research has related the deformations of the therapeutic stem cells carried in a biomaterial to the signalling of injected stem cells.

Stem cell delivery in a biomaterial to the myocardium for MI therapy has gained substantial interest. Most of these studies focused more on the biochemical processes and tried to identify different signalling pathways involved. Many cell mechanics studies have been conducted in 2D environments (focusing on cell migration or adhesion) or a 3D environment (cells embedded in tissue, ECM, and fluids). Stem cells, known as the best candidates for cell therapies, have recently gained considerable attention in investigating mechanotransduction induced by cyclic mechanical stimuli. Very few studies were dedicated to the cell mechanobiology in infarcted heart, either for resident cells or therapeutically delivered cells.

The responses of stem cells to a mechanical input have been widely investigated *in vitro* and are well understood. These cell responses are driven by biochemical reactions. However, the mechanisms underlying these processes have been poorly elucidated. According to the current data and experimental tools, there is potential to address these problems and gain new knowledge using computational approaches. Thus, it is essential to consider computational studies that combine mechanical changes in the myocardial injectates and the signalling of embedded and resident cells.

1.7 Aims and objectives

Based on the limitations of current knowledge described above, the **aims** of this research were:

Aim 1: To develop computational models for predicting the mechanics and associated signalling of cells delivered in a carrier biomaterial intramyocardially for the treatment of myocardial infarction, and

Aim 2: To demonstrate the feasibility of the developed models to investigate and optimise therapeutic cell therapies for myocardial infarction.

Several **objectives** were defined to achieve these aims:

Objective 1: To develop a 3D subject-specific biventricular geometry of a rat heart with left ventricular infarct and biomaterial injectate.

- Geometrical models will be obtained from *ex vivo* μCT image data. Particular emphasis will be placed on the microscopic injectate morphology (dispersion) in the myocardium that depends on the delivery time after the MI occurrence.
- Finite element simulations will investigate the ventricular and wall mechanics, including the deformations of the biomaterial injectate at the organ and tissue level (macroscopic and mesoscopic scale).

Objective 2: To develop a small mid-wall volume of myocardium in the infarcted LV region (sub-model) with microstructural details of the infarcted tissue and interlaced biomaterial injectate that serves as a microenvironment for the delivered cells (microscopic scale).

- The 3D deformations of the associated mid-wall region will be recorded in the biventricular model and used as loading boundary conditions for this sub-model.

Objective 3: To develop a finite element model of a single cell with an idealised spherical geometry and three cellular components, i.e. membrane, cytoplasm and nucleus, with different material properties (elastic modulus).

- One or more cell models will be incorporated in the biomaterial injectate domain of the sub-model to investigate deformations of the delivered cells.

Objective 4: To assess the relationship between computationally predicted deformation and related biochemical responses of the cells, e.g. VEGF/TGF-β production, based on existing experimental data on GF production in stretched cells.

Objective 5: To employ the developed methods and models to investigate the effect of injectate treatment parameters on cellular signalling and therapeutic benefit.

- Stiffness of the biomaterial injectate and the injection timing after infarction (i.e. coronary artery occlusion) are possible targets for these studies.

Chapter 2 Materials and methods

In the current study, cell mechanics were investigated in the context of a treatment for myocardial infarction. The therapy consists of intramyocardially delivering stem cells within a biomaterial into the impaired heart, especially around the infarct region. Several studies have reported biomaterial injection to alter the remodelling following the infarction. Further, introducing stem cells in the biomaterial activates biochemical reactions that lead to tissue regeneration and neo-vascularisation through paracrine signalling. The FE model developed in the study was designed to predict the mechanical responses of the injected cells in the context of cell-embedded biomaterial.

Due to the heart activities, the deformations produced at the heart tissue level are translated from the cardiac tissue to the biomaterial injectate, which deforms the embedded therapeutic cells. Therefore, the current study was conducted by considering three scales:

- The organ: the rat heart
- The tissue: a small block of heart tissue extracted from the LV free wall
- The cell: the injected cells located in the biomaterial

This chapter presents the methodology to develop models to predict the mechanics and associated signalling of cells delivered in an intramyocardially injected biomaterial to treat myocardial infarction.

2.1 Geometry development

2.1.1 Reconstruction of a biventricular geometry of a rat heart with biomaterial injectate

Data acquisition

Ex vivo microcomputed tomography (µCT) image data of infarcted rat hearts with polymeric injectates from an unrelated study (unpublished data) were used for geometric reconstruction. (Disclosure: The data acquisition describe here including in vivo experiments and ex vivo imaging was conducted prior to this thesis without involvement of the author but by collaborators of and under the supervision of Profs N Davies and T Franz.)

In brief, male Wistar rats (body mass: 180-220 g) were anaesthetised, and the heart was exposed via left thoracotomy along the 4th intercostal space. Myocardial infarction was induced by permanent ligation of the left anterior descending coronary artery 3 mm distal to the auricular appendix. The discolouration of the anterior ventricular wall and reduced contractility were hallmarks of a successful occlusion of the artery. The animals were divided into two groups based on the injection timing after the coronary occlusion: immediate and delayed injection groups. The first group of animals (immediate injection, n = 8) received 100 µl of radiopaque silicone rubber containing lead chromate (Microfil® MV-120 Flow-Tech, Carver, MA, USA) diluted 1.5:1 with MV-diluent via injection into the infarcted area of the myocardium immediately after infarct induction. In the second group of animals (delayed injection, n = 7), the chest was stepwise closed following infarct induction and buprenorphine was administered for pain management. Seven days later, the heart was accessed via the 4th intercostal space and 100 µl Microfil® radiopaque material was injected into the infarct area. For both groups, dispersion and *in situ* polymerisation of the Microfil® material were allowed for 30 min after the injection. The animals were then humanely killed and the hearts carefully harvested, thoroughly rinsed with saline, fixed in a 4% paraformaldehyde solution and transferred to saline for microcomputed tomography (µCT) scanning. All animal experiments were authorised by the Institutional Review Board of the University of Cape Town and

performed according to the National Institutes of Health (NIH, Bethesda, MD, USA) guidelines.

The µCT scans were performed with a custom-made scanner with a Feinfocus X-ray tube and a Varian 2520V Paxscan a-Si flat panel detector (CsI screen, 1920 x 1536, 127 µm pixel size) at the Centre for X-ray Tomography of Ghent University (UGCT) (Masschaele *et al.* 2007). For each scan, 1801 projections were captured with an exposure time of 0.8 s. The resulting scan images had a voxel pitch of 10 µm. Reconstruction was performed using the UGCT software package Octopus (Vlassenbroeck *et al.* 2007) (distributed by XRE, Ghent, Belgium, www.xre.be).

Sample selection

The selection of a sample for this study was based on several criteria. The first criterion was the time of injection. Several studies reported the impact of injection time on the outcomes of biomaterial therapies. Kadner *et al.* (2012) demonstrated that the injection of PEG hydrogel one week following the infarction (i.e. delayed injection) led to significant improvements in infarct heart's function and scar tissue mechanics. Additionally, depending on the injection time, different distribution patterns of the injectate were observed. The immediately delivered injectates have a fibrillar-like structure, whereas the delayed injectates exhibited a bulky morphology.

Similar observations were made on the data examined for the current study. The delayed injection group was chosen for the FE model based on the above information. The selection among the six data sets was based on the additional criteria of the image quality for segmentation. In practice, the images with a good intensity level and a high contrast between the biomaterial injectate (high intensity) and the cardiac tissue (low intensity) (see Figure 2) were privileged.

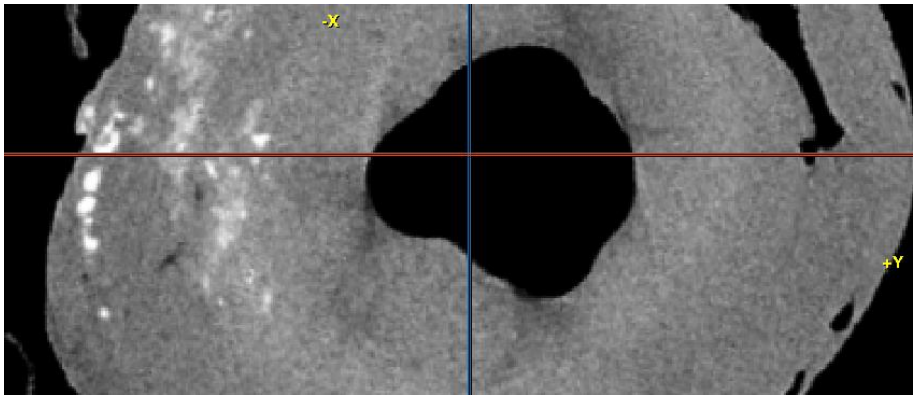

Figure 2. Cross-section image of an injected rat heart. The injectate has a higher intensity level compared to the cardiac tissue.

The atria were excluded in the selected sample data, and only the two ventricles were considered for the FE model development. The resulting geometry was a biventricular geometry truncated at the base. The truncation plane was chosen perpendicular to the longitudinal axis of the heart. In the initial data imported in Simpleware, the long axis (the apex-base axis) was not aligned with the long axis of the heart (red axis in Figure 3a). It was essential to implement a correct images orientation to obtain a precise fibre orientation direction. The proper orientation will result in a realistic fibre structure and a correct implementation of the myocardium mechanics (see Figure 3b).

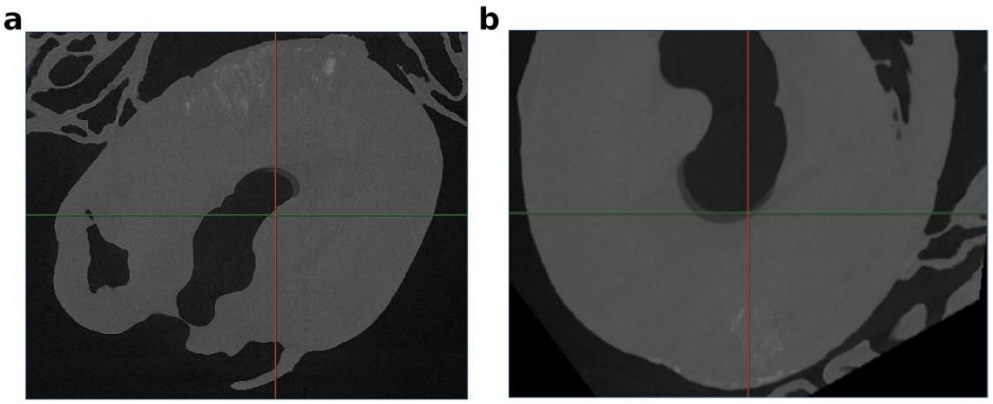

Figure 3. Re-orientation of heart geometry. (a) a non-oriented heart, the red axis (z-axis) is not aligned with the longitudinal axis (apex-base). (b) a representation of a truncated geometry at the base. The red axis is well aligned with the long axis.

Segmentation

Simpleware was used for segmentation with several features, including region-growing, level-set threshold and manual segmentation. Due to noise and the complexity of the images, manual and automatic (level-set threshold) segmentation techniques were combined. Two masks were created during the segmentation featuring the cardiac tissue and the injectate. The lack of histological data and the quality (capability to detect healthy from infarcted tissue) of the image data did not allow identifying the region of the cardiac infarct. Hence, the infarcted region was estimated and implemented manually in the FE model. The resulting geometry was meshed and used as a discretised domain for the FE model in Abaqus/CAE (Abaqus 6.14-3, Dassault Systèmes, Providence, RI, USA).

2.1.2 The extracted left ventricular mid-wall block

A small block was extracted from the biventricular model described in section 2.1.1. A resampling operation was performed in Simpleware on the entire heart geometry to obtain a 748 µm x 748 µm x 722 µm block (Figure 4). The resulting geometry referred to as sub-model comprised cardiac tissue (infarcted) and dispersed injectate. The x, y and z spacing were modified from 0.03, 0.03, and 0.03 mm in the biventricular (BV) model to 0.0078, 0.0078, and 0.0078 mm in the sub-model to accommodate the microscopic dimensions of the main cellular components (membrane, cytoplasm and nucleus) to be implemented later.

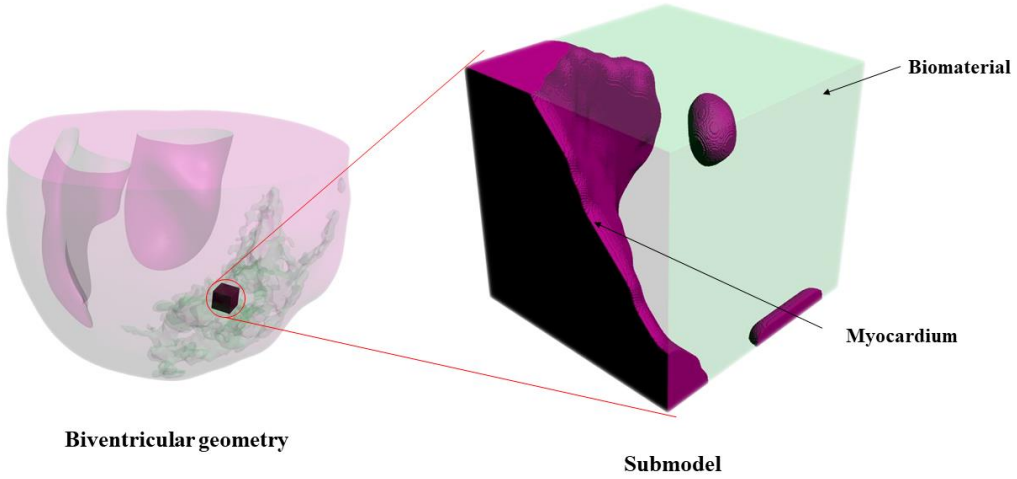

Figure 4. Sub-model geometry developed from the BV model.

2.1.3 Cell geometry and numerical cell seeding

Cells have been widely imaged and represented for mechanical investigations (Alihemmati *et al.* 2017, Caille *et al.* 2002, Saeed *et al.* 2016, Slomka *et al.* 2009, Yamada *et al.* 2009). In a 3D environment, cells can be represented either with a realistic shape from image reconstruction or an idealised geometry with specific characteristics close to the *in-vivo* geometry.

In the current study, the cell was represented by an ideal sphere. A three-component model was adopted to describe the membrane, cytoplasm and nucleus. Three spheres were created in Simpleware, sharing the same centre. The smallest sphere represents the nucleus. The region between the middle sphere and the nucleus represents the cytoplasm. The membrane was defined by a difference between the middle and the largest sphere. The final cellular geometry results in a different thicknesses for each component.

A Python script was created and implemented in Simpleware to seed cells at random locations in the injectate region of the sub-model. The process consisted of creating concentric spherical surfaces with a diameter of 60, 55 and 20 µm for the membrane, cytoplasm, and nucleus, respectively, at an arbitrary location in the biomaterial injectate. The developed cells were incorporated randomly in the injectate region of the sub-model geometry described in section 2.1.2. The developed Python script is available as supplementary data.

2.2 Myofibre structure in the cardiac model

The heart anatomy reveals a specific alignment of cardiac cells in myofibers that form bundles. The configuration of myofibers in layers plays an essential role in myocardial mechanics. This configuration introduces an anisotropic structure in the myocardium, responsible for different mechanical responses in various directions. This microstructure results in a preferred direction for the contraction in the cardiac tissue. It is, therefore, essential to consider the orientation of myofibers in computational modelling to obtain a complete and accurate FE model.

A rule-based algorithm developed by Sack *et al.* (2018) was implemented in the BV model. The principle consists of generating the projection of the fibre in a 3D coordinate system. The projected values of the fibre vector were obtained with two principal angles:

- The helix angle $\alpha_h = (f_{p1,} u_c)$ formed by the projection of the fibre on the plan made of the circumferential-longitudinal unit vector (u_c, u_l) and the circumferential unit vector u_c (Figure 5),
- The transverse angle $\alpha_t = (f_{p2}, u_c)$ between the projection of the fibre on the plane formed by the radial-circumferential unit vector (f_{p1}) and the circumferential unit vector (Figure 5).

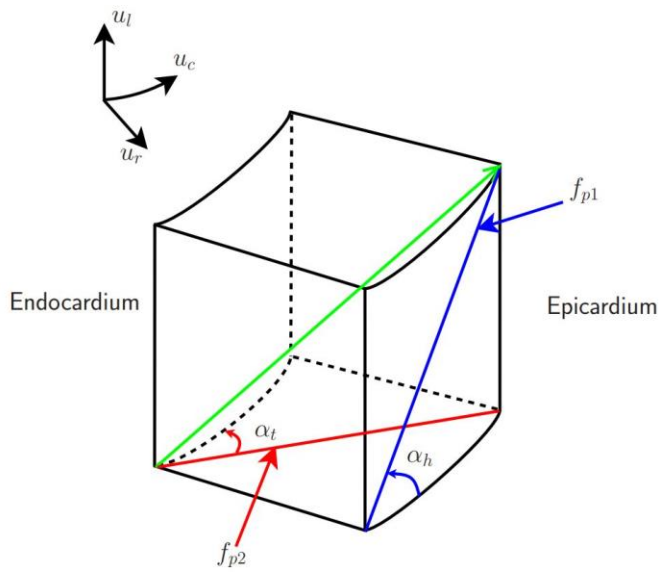

Figure 5. Myocardial fibre orientation in a unit volume element. The fibre direction is defined by two projections f_{p1} (with angle α_h relative to the unit vector u_c) and f_{p2} (with angle α_t relative to the unit vector u_r).

2.3 Constitutive laws

A constitutive model is a mathematical representation of material response to external mechanical input. These mathematical equations describe the responses of biological tissue to mechanical changes induced by loads and displacements.

In the heart, the deformations are originated from the active contractile cardiac cells or passive pressure during the filling of the ventricles.

The healthy and infarcted tissue was treated as hyperelastic anisotropic material during the passive filling stage of the cardiac cycle. The biomaterial injectate was assigned with a non-linear isotropic material law for the entire cycle. An additional constitutive model was used to represent the behaviour of healthy tissue during the active contraction phase.

2.3.1 Constitutive model of cardiac tissue

The mechanical properties of the infarcted region of the damaged myocardium depend on the stage of the infarct. It has been demonstrated that the pathological state of the heart plays an essential role in the mechanics of cardiac tissue (Holmes *et al.* 2005, Holmes *et al.* 1997, Tyberg *et al.* 1974, Villarreal *et al.* 1991). The finite element model (FEM) developed in this study needs to capture the complete mechanical behaviour of both infarcted and healthy tissue at different stages of the cardiac cycle (the passive filling and the active contraction). In addition, the model must reproduce the impact of the infarcted tissue on the mechanical response of the heart. The infarct reduces the capability of the myocardium to contract. As a result, the impaired tissue behaves as a passive material with increased material stiffness (Holmes *et al.* 2005). Finally, the mechanical properties of the injectate and cardiac tissue (healthy and infarcted) were incorporated in a FEM for simulations.

Passive filling

The healthy myocardium was treated as a hyperelastic anisotropic material during the passive filling. The mathematical formulation was adopted from the model proposed by Holzapfel and Ogden (2009). The strain energy density function in this formulation is given by:

$$W = \frac{a}{2b} e^{b(I_1-3)} + \sum_{i=f,s} \frac{a_i}{2b_i} \{e^{b_i(I_{4i}-1)^2} - 1\} + \frac{a_{fs}}{2b_{fs}} \{e^{b_{fs}(I_{8fs})^2} - 1\} + \frac{1}{D}\left(\frac{J^2-1}{2} - \ln(J)\right) \quad (2.1)$$

where the parameters used are provided in Table 3.

A similar formulation was used to describe the infarcted heart tissue with modifications in myofiber stiffness (increased stiffness in fibre, circumferential and longitudinal directions). The infarct response is illustrated in Eqn. (2.2) and obtained by adjusting the material stiffness. This approach was adopted from the model developed and validated by Sack *et al.* (2018). The mathematical formulation is given by:

$$W = \frac{\bar{a}}{2b} e^{b(I_1-3)} + \sum_{i=f,s} \frac{\bar{a}_i}{2b_i} \{e^{b_i(I_{4i}-1)^2} - 1\} + \frac{\bar{a}_{fs}}{2b_{fs}} \{e^{b_{fs}(I_{8fs})^2} - 1\} \quad (2.2)$$

with

$$\bar{a}_i = a_i(h + (1-h)p) \quad (2.3)$$

The parameters in Eqn. (2.2) are described in Table 3. These parameters were adopted from the literature (Dương *et al.* 2018, Sack *et al.* 2018). The parameters $\bar{a}$, $\bar{a}_i$ ($i = f, s$) and $\bar{a}_{fs}$, in Eqn. (2.2), govern the isotropic response of the infarcted myocardium and define the proportion of healthy and pathological tissue present in the myocardium. The scalar parameter h governs the health of the material point (Sack *et al.* 2018). The scaling parameter p adjusts the passive response according to the stage of the infarct.

Table 3. Constitutive parameters for passive mechanical behaviour of myocardium (Sack *et al.* 2018)

Parameter	Value	Description
a	0.2065 kPa	Governs the isotropic response
b	7.61	Governs the isotropic response
a_f	0.68 kPa	Governs additional stiffness in the fibre direction
b_f	14.61	Governs additional stiffness in the fibre direction
a_s	0.945 kPa	Governs additional stiffness in the sheet direction
b_s	12.67	Governs additional stiffness in the sheet direction
a_{fs}	5.55×10^{-2} kPa	Governs coupling stiffness in the fibre and sheet direction
b_{fs}	3.12	Governs coupling stiffness in the fibre and sheet direction
I_1, I_{4i}, I_{8fs}	-	Strain invariants
D	0.2×10^{-3} kPa^{-1}	Defines material incompressibility. Inversely proportional to the bulk modulus (K=2/D) defining the material's resistance to compression.
J	-	Third deformation gradient invariant

Active contraction

The active contraction during the cardiac systole was implemented with a time-varying elastance approach and described the active tension responsible for muscle contraction. An additional term was added to keep the passive response during the contraction (Guccione and Mcculloch 1993, Guccione *et al.* 1993, Walker *et al.* 2005). The merit of this model resides in the fact that it predicts the active tension developed by the myocardium by including the deactivation of calcium channels, the time of onset of contraction and the sarcomere length history (Guccione *et al.* 1993). The mathematical formulation of the active tension model is (Guccione *et al.* 1993, Sack *et al.* 2018, Walker *et al.* 2005):

$$T_a(t, E_{ff}) = \frac{T_{max}}{2} \frac{Ca_0^2}{Ca_0^2 + EC_{a_{50}}^2(E_{ff})} \left(1 - \cos\left(\omega(t, E_{ff})\right)\right) \tag{2.4}$$

The description of the parameters used is given in Table 4. The functions ECa_{50}, w, t and l are provided by the equations below:

$$ECa_{50}^2(E_{ff}) = \frac{Ca_{0_{max}}}{\sqrt{e^{B(l(E_{ff})-l_0)} - 1}}, \tag{2.5}$$

$$\omega(t, E_{ff}) = \pi\frac{t}{t_0}, \qquad \text{for } 0 \leq t \leq t_0 \tag{2.6}$$

$$\omega(t, E_{ff}) = \pi\frac{t - t_0 + t_r(l)}{t_r(l)}, \qquad \text{for } t_0 \leq t \leq t_r \tag{2.7}$$

$$\omega(t, E_{ff}) = 0, \qquad \text{for } t \geq t_0 + t_0 \tag{2.8}$$

Table 4. Constitutive parameters for active contraction in myocardium (Guccione *et al.* 1993, Sack *et al.* 2018)

Parameter	**Value & unit**	**Description**
T_{max}	60 kPa	Constitutive law scaling factor
Ca_0	4.35 µmol/l	Peak intercellular calcium concentration
Ca_{0max}	4.35 µmol/l	Maximum intercellular calcium concentration
B	4,750 mm^{-1}	Governs the shape of the peak isometric tension-sarcomere length relation
l_0	1.58 x 10^{-3} mm	The sarcomere length below which no active force develops
t_0	0.15 s	Time to reach peak tension
m	1,048.9 s/mm	Govern the shape of the linear relaxation duration and sarcomere relaxation
b	1.5 s	Govern the shape of the linear relaxation duration and sarcomere relaxation
E_{ff}	-	Lagrangian strain tensor component aligned with the local muscle fibre direction
l_r	2.03 x 10^{-3} mm	Initial sarcomere length

2.3.2 Injectable biomaterials

Mechanical support devices, including left ventricular assist devices (LVAD), are widely used for patients with end-stage heart failure and have demonstrated considerable advancement (Birks *et al.* 2006, Burkhoff *et al.* 2006). However, they can become very invasive and uncomfortable for use. Thus, non-degradable polymers have gained substantial attention in research in the last two decades and have been investigated considerably as an alternative and non-invasive solution. Injectable polymer hydrogels have demonstrated beneficial effects on the impaired heart by retarding the ventricular remodelling followed by a decrease in the wall stress (Christman *et al.* 2004a, Dobner *et al.* 2009, Wall *et al.* 2006, Wang *et al.* 2012). Furthermore, biomaterial injectates were developed as scaffolds for cells in cellular-based therapies (Hoeeg *et al.* 2021, Ke *et al.* 2020, Zhao *et al.* 2016).

In the current study, the injectable biomaterial (e.g. PEG hydrogel) was described as hyperelastic isotropic incompressible material. The mechanical responses were predicted using the Neo-Hookean material model with the following strain energy density function:

$$W = C_{10}(I_1 - 3) \tag{2.9}$$

where C_{10} characterises the material stiffness obtained from elastic modulus E and the Poisson ratio ν (Eqn. (2.10)), I_1 is the first deviatoric strain invariant defined in terms of deviatoric or principal stretch (see Eqn. (2.13)).

In the current study, the injectate biomaterial was treated as incompressible material. Thus, the Poisson's ratio was 0.5, and the elastic modulus varied from 4.1 kPa to 405,900 kPa (parametric study to investigate the impact of the biomaterial stiffness on biventricular deformation and subsequently on the cell mechanics and signalling).

$$C_{10} = \frac{E}{4(1 + \nu)} \tag{2.10}$$

Table 5. Material parameters for biomaterial injectate

Parameter	**Values**
Elastic modulus E (kPa)	4.1, 7.4, 40.6, 73.8, 405.9, 738.0, 4,059.0, 7,380.0, 40,590.0, 73,800.0, 405,900.0
Poisson's ratio ν	0.5

2.3.3 Cell mechanical properties

The cell is structurally composed of microfilament and microtubules that participate in the mechanical responses. These microstructures are compartmentalised into three main components (membrane, cytoplasm and nucleus). The average mechanical property in each compartment is different, where the cell membrane exhibits softer stiffness than the cytoplasm and nucleus. For this reason, the elastic modulus describing cell mechanical property was assigned by compartment. The complexity of cellular mechanics resides in the fact that they can respond to external forces by reinforcing their composition through active processes such as polymerisation or depolymerisation.

The dynamics of the cytoskeletal actin network, which governs the primary active response in living cells, has been modelled with a viscoelastic approach in several studies (Bausch *et al.* 1998, Evans 1989, Karcher *et al.* 2003, Yamada *et al.* 2000). In the current study, a hyperelastic approach was used to describe the mechanics of the cellular components.

A three-component model was used to represent the cell, as described in section 2.1.3. Each component is treated as hyperelastic isotropic compressible material described with a Neo-Hookean material law. The mathematical formulation of the strain energy density function (W) is given by:

$$W = C_{10}(\bar{I}_1 - 3) + \frac{1}{D_1}\left(J^{el} - 1\right)^2, \tag{2.11}$$

where C_{10} and D_1 depend on the elastic modulus and the material compressibility. The parameter C_{10} is given by Eqn. (2.10), and D_1 is provided by Eqn. (2.12). I_1 is the first deviatoric strain invariant defined in terms of deviatoric or principal stretches.

$$D_1 = \frac{2\,E}{3(1-2\nu)}, \tag{2.12}$$

$$\bar{I}_1 = \bar{\lambda}_1^{\,2} + \bar{\lambda}_2^{\,2} + \bar{\lambda}_3^{\,2} \tag{2.13}$$

Different material parameters are used for each component of the cell. A summary is given in the table below:

Table 6. Values of mechanical properties of cell components (membrane, cytoplasm and nucleus) (Caille *et al.* 2002, Jean *et al.* 2005).

	Elastic modulus E (kPa)	**Poisson ratio (v)**
Membrane	1.7	0.4
Cytoplasm	8	0.3
Nucleus	5	0.4

2.4 Finite element model development

The meshed BV geometry was imported in Abaqus/CAE (Abaqus 6.14-3, Dassault Systèmes, Providence, RI, USA). At the tissue level, the deformations were examined to determine cardiac tissue response during an entire cardiac cycle. Particular attention was given to the mechanics of the injectate. Furthermore, a sub-modelling technique was developed to study the micromechanics of the region extracted from the LV mid-wall and subsequently investigate the impact of the injectate deformations on the signalling of cells delivered in the biomaterial.

2.4.1 Biventricular finite element model of a rat heart

The BV geometry developed (section 2.1.1) was incorporated in Abaqus/CAE (Abaqus 6.14-3, Dassault Systèmes, Providence, RI, USA) to implement the different mechanical properties and investigate cardiac tissue mechanics based on the finite element modelling approach. A 10-node tetrahedral element type was used to obtain a discretised FE problem.

Boundary conditions

It is essential to consider realistic boundary conditions that reproduce the biological environment and the different loads applied to the domain's boundaries.

A zero displacement was applied to the nodes at the base in the longitudinal direction to prevent the rigid body motion of the geometry, see Figure 6. The passive filing was implemented by a linearly increasing pressure load on both LV and RV cavity surfaces. Several studies reported a higher pressure in the LV cavity (LV cavity pressure is four times the RV pressure). The measured systolic pressure is 30-40 mmHg and 100-140 mmHg in normal human hearts, respectively, in the RV and LV cavity (Mininni *et al.* 1996, Reichek and Devereux 1982). Pacher *et al.* (2004) measured left ventricle end-diastolic and left ventricular end-systolic pressure in rats and found 3.8 ± 0.9 mmHg and 133.8 ± 8.1 mmHg, respectively. In the current study, the cavity pressure was taken from 0 to 3.0 mmHg and 0 to 0.75 mmHg, respectively, for LV and RV cavities. This choice agrees with the range of the experimental end-diastolic pressure findings.

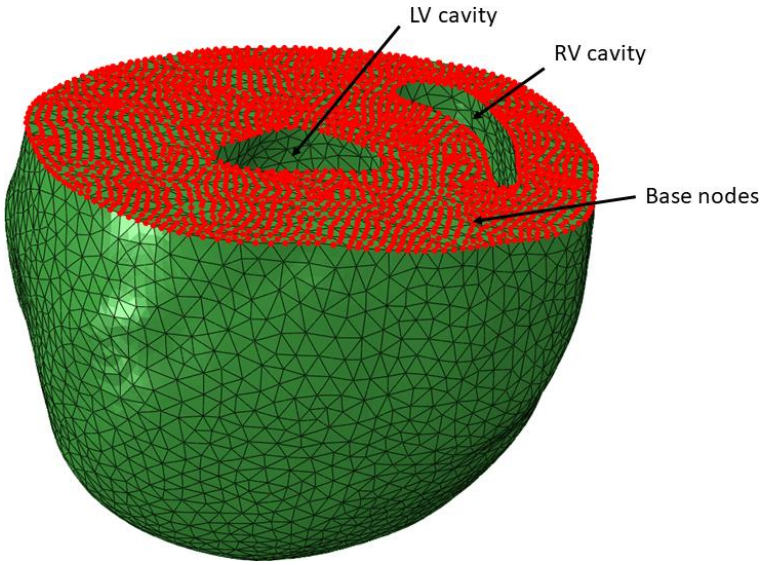

Figure 6. Heart geometry with a highlight on the base nodes and cavities. Base nodes are highlighted with red points where zero displacement boundary condition is applied. Linearly increasing pressure is applied to the LV and RV cavities.

Determination of computation time for end-systole and end-diastole

The end-diastolic time point was determined by applying a linearly increasing pressure on the LV and RV endocardial surfaces until the LV cavity volume matched a target experimental ED volume by Pacher *et al.* (2004). This step was performed on the BV model with injectate elastic modulus E_{inj} = 73.8 kPa.

A second simulation was performed to determine the end-systolic time point. The obtained time corresponded to the contraction and was determined from the ED time point defined previously until the active tension declined. The LV volume was calculated at this time point and compared with end-systolic volume values in the literature (Pacher *et al.* 2004).

2.4.2 Sub-model with embedded cells

The sub-modelling technique was used to investigate the micromechanics of the extracted block described in section 2.1.2. The nodal displacements in the sub-model region of the BV model were recorded for a complete cardiac cycle and applied to the sub-model.

The parametric simulation was achieved with several elastic moduli of injectate, E_I, between 4.1 and 405,900 kPa. The volume-averaged strain was recorded in the cardiac tissue and the injectate and analysed with the deformations observed in the embedded cells.

At the cellular level, the volume-averaged strain and the strain distribution in the cells were reported from the sub-model. The strain distribution was evaluated across the different injectate stiffness to optimise the impact of the biomaterial stiffness on the cell deformation.

2.5 Cell deformation and paracrine signalling: Production of TGF-β in a mechanically active environment

Therapeutical cells within an injected biomaterial are influenced by the mechanical changes in their surrounding environment. Biochemical signalling is a well-known response to these mechanical inputs. In the current study, the mechanical inputs sensed by cells were assumed to originate from the deformation of the biomaterial injectate due to cardiac activities.

A mathematical model was developed to predict the amount of TGF-β produced by therapeutic mesenchymal stem cells due to the deformations induced by heart activities. The model involves the calculation of TGF-β concentration using a linear interpolation function derived from experimental data. The TGF-β concentration was determined from the cellular averaged strain computed from the FE simulations in the sub-model. The function was obtained from data from the cell stretching experiments by Hirakata *et al.* (1997) and its replication with a FE model. Firstly, a relationship was established between TGF-β concentration and tensile strain of the substrate from experimental data. Secondly, a FE model that mimics the experiment by Hirakata *et al.* (1997) was developed to express the intracellular strain as a function of substrate strain. A more detailed description of the FE model is provided in the next section.

2.5.1 Computational modelling of the mechanics of a single cell on an elastic stretched substrate using a finite element modelling

A finite element model of a single-cell attached to an elastic substrate through focal adhesions was developed (Figure 7). The substrate was subjected to biaxial displacements (see Figure 7a). A spherical cap with small disks attached to its flat surface represented the cell and focal adhesions, respectively, as shown in Figure 7b. The attachment of the cell to the substrate was modelled with a tie constraint to ensure permanent adhesion and prevent sliding. The same contact conditions were applied between the cell body and the focal adhesions.

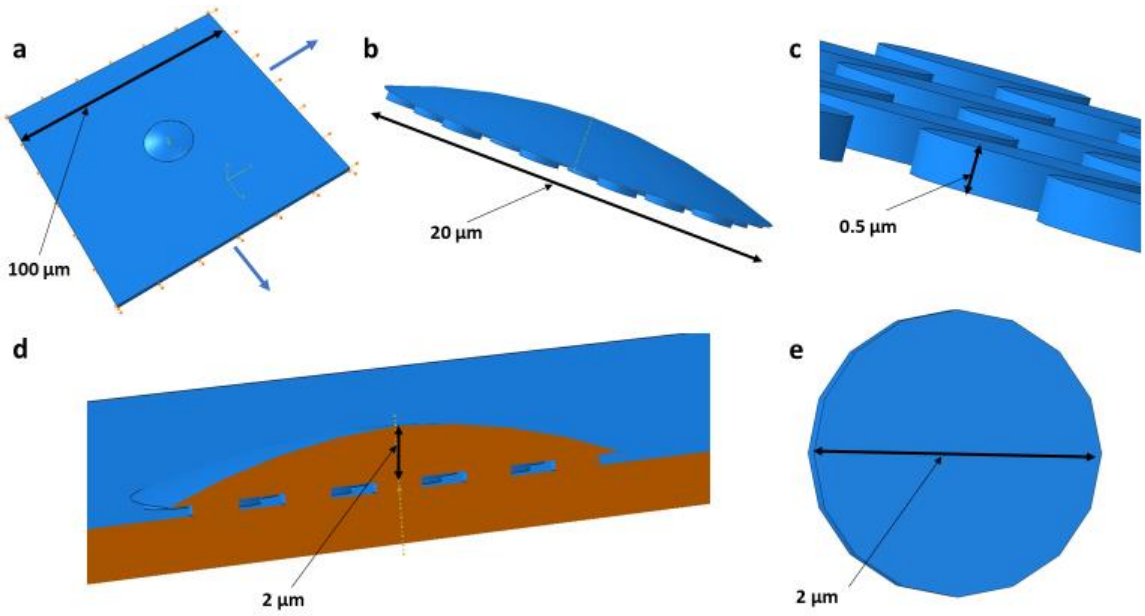

Figure 7. Single-cell stretching finite element model. Single-cell geometry attached to a substrate displaced with 5, 10, 15, and 20% strain (a, d). The cellular geometry consists of a spherical cup attached to disks representing the cell body (b) and the focal adhesions (b,c and e).

Biaxial displacements generating substrate tensile strains of 5%, 10%, 15%, and 20% were applied to the substrate edges to reproduce the conditions of Hirakata *et al.* (1997) experiments. The averaged strain was recorded in the cell and the focal adhesions for each applied substrate strain. A linear fit was then used to express the cellular deformation as a function of the substrate strain (see Eqn. (2.15)).

2.5.2 Modelling TGF-β production in cells exposed to substrate stretch

Several experimental studies have permitted quantifying the mechanically-induced cellular signalling of growth factor release. Hirakata *et al.* (1997) measured mRNA expression for TGF-β induced by cyclic mechanical stretch. In the study, cells were cultured and attached to an elastic substrate subjected to mechanical strain with different amplitudes (5%, 10%, 15% and 20%). They reported a relationship between the concentration of TGF-β mRNA expression and the substrate strain amplitude (Figure 8).

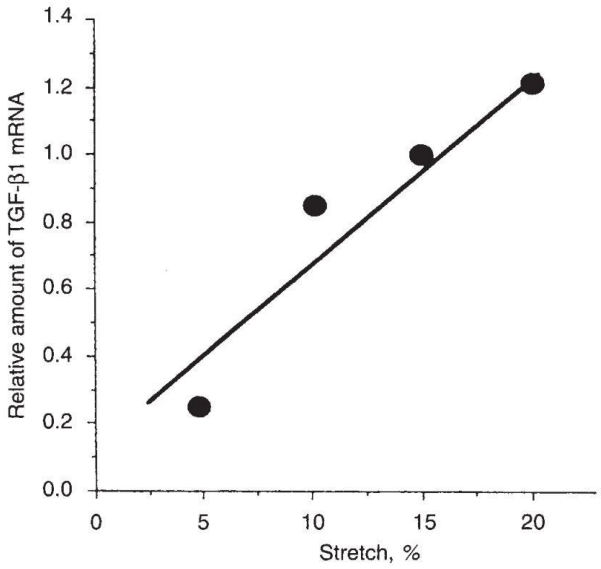

Figure 8. The relative amount of TGF-β mRNA for various mechanical tensile strain amplitudes, image adapted with permission from Hirakata *et al.* (1997).

The results were utilised in the current study to develop a linear fit of TGF-β expression as a function of the substrate strain with the following equation:

$$\text{TGF-}\beta = a_0\, \varepsilon_{Sub} + b_0, \tag{2.14}$$

where a_0 and b_0 were calibrated from a linear fit and ε_{Sub} is the substrate strain.

A second linear relationship (Eqn. (2.15)) was developed from the FE model described in section 2.5.1, between the computed averaged strain in the cell and the substrate strain.

$$\varepsilon_{Cell} = a_1\varepsilon_{Sub} + b_1, \tag{2.15}$$

where a_1 and b_1 were calibrated from a linear fit.

Finally, Eqs. (2.14) and (2.15) were combined to determine the amount of TGF-β mRNA expressed in terms of intracellular strain.

$$\text{TGF-}\beta = a_2\varepsilon_{cell} + b_2\,, \tag{2.16}$$

where a_2 and b_2 were determined by elimination of ε_{Sub} in Eqns. (2.14 and (2.15).

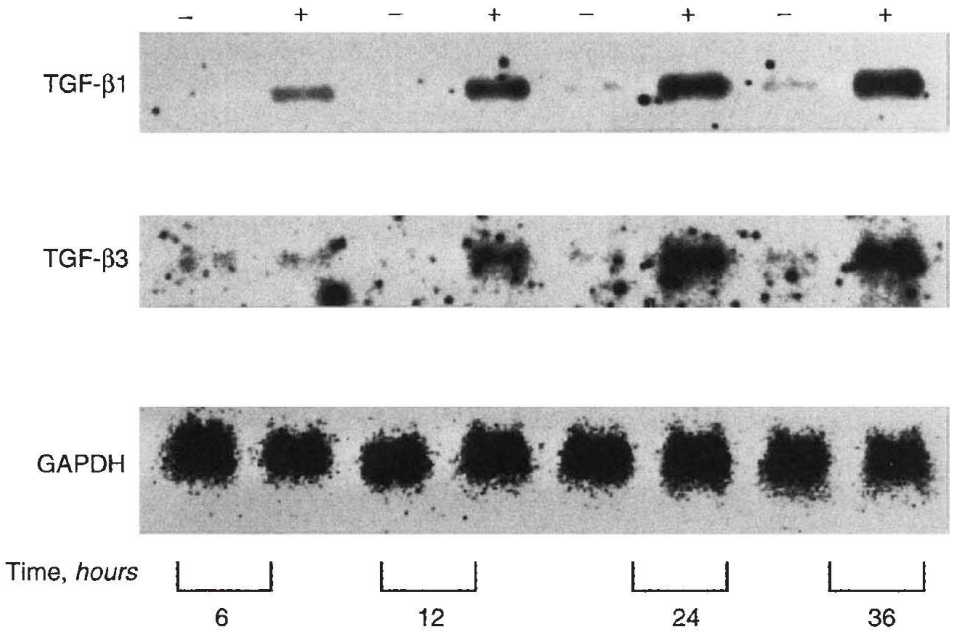

Figure 9. Secretion of TGF-β due to mechanical stretch. Analysis of the amount of TGF-β1 and TGF-β3 mRNA produced after exposure of cells to mechanical stretch for 6, 12, 24 and 36 hours. The figure was adopted from Hirakata *et al.* (1997).

2.6 FE simulations and data analysis

A parametric study was conducted with various biomaterial injectate elastic modulus ranging from E_{inj} = 4.1 to 405,900 kPa (the complete list of values used is provided in Table 5). The parametric study was designed to investigate the impact of injectate stiffness on the deformation of the myocardium, the biomaterial injectate and the therapeutic stem cells.

The myofibre and cross-fibre strain were analysed in the BV model (healthy and infarcted tissue). The deformations of the injectate region in the BV model were assessed by analysing the minimum principal and maximum principal strains.

In the BV model (i.e. myocardium and injectate), the median strain was calculated for each value of injectate elastic modulus. Furthermore, the strain distribution was also analysed and presented in boxplots showing the distribution of mesh element strain around the median strain value.

In the sub-model, a similar analysis was performed in the different regions:

- The biomaterial injectate
- The myocardium (infarcted tissue)
- Each cell (membrane, cytoplasm, and nucleus)

The following cellular strain computations were determined for all nine cells for each injectate stiffness.

The mean values of the maximum principal strain and the minimum principal strain at the integration points were determined for each tetrahedral element in the meshed geometry. These mean values are referred to as element strain (see Eqn. (2.17)). The element strains were recorded for each cellular component, i.e. membrane, cytoplasm and nucleus, at end-diastole and end-systole for each of the eleven values of injectate elastic modulus (elastic modulus values used can be found in Table 5). Nine cells were considered in the analysis.

The cellular strain data were presented in boxplots, showing the distribution of the volume-averaged strain of nine cells locations for eleven injectate stiffnesses. Histograms are also

reported to show the distribution of element strain within the geometries (the histograms are not presented in the results section but are available as supplementary data).

For each element in the cell meshes, the mean element strain $\varepsilon_{element}$ was obtained from the strain values at the integration points, i.e.

$$\varepsilon_{element} = \sum_{i=1}^{4} \varepsilon_{ip_i}, \tag{2.17}$$

where ε_{ip_i} is the strain at i^{th} integration point in the element (the models were defined with four integration points).

The volume-averaged strain for each cell component was calculated from the previously defined mean element strain as:

$$\varepsilon_{comp} = \frac{1}{V} \sum_{i=1}^{N} v_i \varepsilon_{element_i}, \tag{2.18}$$

where V is the total volume of the region considered, N is the total number of elements in the considered cell component, v_i is the volume of a single element i, and $\varepsilon_{element\_i}$ is the mean element strain from the integration points (i = 1, 2, …, N) calculated from Eqn. (2.17).

The mean strain of each cell component was calculated for each of the eleven injectate stiffnesses as:

$$\bar{\varepsilon}_{comp} = \frac{1}{n} \sum_{i=1}^{n} \varepsilon_{comp}, \tag{2.19}$$

Here, ε_{comp} is the volume-averaged in a cell component (comp = membrane, cytoplasm or nucleus), n is the number of cells used in the sub-model (n = 9 in the current study). The mean strain in the whole cell, also referred to as group cell strain, was obtained from the mean strain of the three cell components:

$$\varepsilon_{cell} = \frac{1}{c} \sum_{i=1}^{c} \bar{\varepsilon}_{comp}\,, \tag{2.20}$$

where c is the number of cell components, i.e. three.

Descriptive statistical analysis was performed on the strain data to determine the normality (Shapiro-Wilk normality test) and variability (SciPy, https://scipy.org/ and NumPy, https://numpy.org/). Data were presented using box and whisker plots (MatPlotLib, Python, https://matplotlib.org/), indicating median and interquartile ranges..

Boxplots were used to assess the distribution of the numerical strain data and the skewness with quartiles (or percentiles) and medians. For each region considered, a strain value (maximum principle, minimum principle, myofibre or cross-fibre strain) was recorded per element and ranked.

Five values were generally used to represent the data distribution:

- The lower quartile (Q_1) is the limit where 25% of the data falls below
- The upper quartile (Q_3) corresponds to a value in the data where 75% of fall on, thus 25% of values in the data are above
- The median is the mid-point of the ranked data. In the boxplot, the median is shown by a line dividing the box into two parts. Hence, half of the strain data falls below or above this value
- The minimum score is the lowest value excluding the outliers
- The maximum score is the highest value excluding the outliers

The upper and lower whiskers represent the scores outside the middle 50% (i.e. the lower 25% and the upper 25% of the scores). The interquartile range (IQR) is the boxplot that shows the middle 50% of scores (i.e. it ranges between the 25th and the 75th percentile). Boxplots are compared using the IQR, medians, outliers and skewness.

Chapter 3 Results

The geometries, the developed FE and mathematical models, and the results from simulations are presented in this chapter. The deformations in the myocardium (including the infarcted tissue) are assessed for a range of injectate stiffness using the fibre and cross-fibre strain. The maximum principal and minimum principal strains are reported for the injectate region in the BV model and the sub-model. Additionally, the variability and distribution of strain within the different models are presented using boxplots and histograms.

The impact of the injectate stiffness on the therapeutic cellular mechanics and signalling is addressed.

3.1 Biventricular model of rat heart with LV infarct and therapeutic injectate

3.1.1 Biventricular geometry and finite element model of the rat heart

A biventricular geometry was developed, comprising RV and LV cavities and capturing essential details of the ventricular morphology (Figure 11). The biventricular model displayed a detailed dispersion of the injectate within the LV free wall. The generated mesh comprised 206,142 quadratic tetrahedral elements (58,902 and 147,240 elements respectively for injectate region and myocardium). The mesh density was heterogenous through the geometry. Along the different regions, the mesh density varied from 3,852.3 to 302.8 elements/mm^3, respectively, from the injectate region to the myocardium. Thus, the mesh density increases toward the injectate region in the biventricular model (see Figure 10).

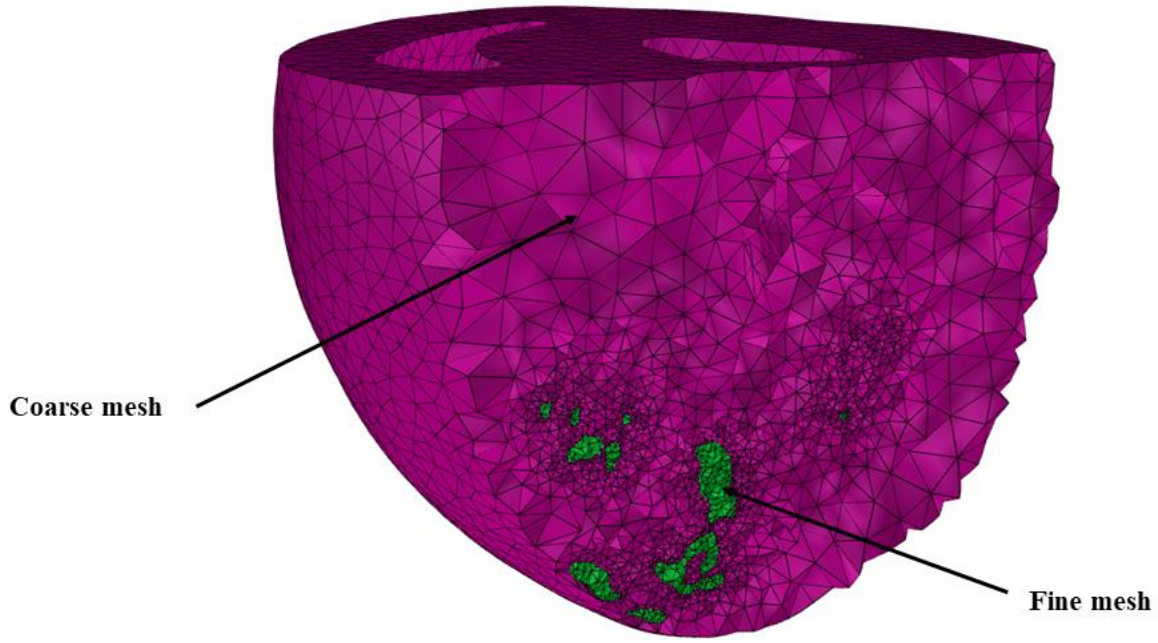

Figure 10. Variation in mesh density within the myocardium region and from the myocardium to the injectate. The mesh density increases toward the injectate geometry.

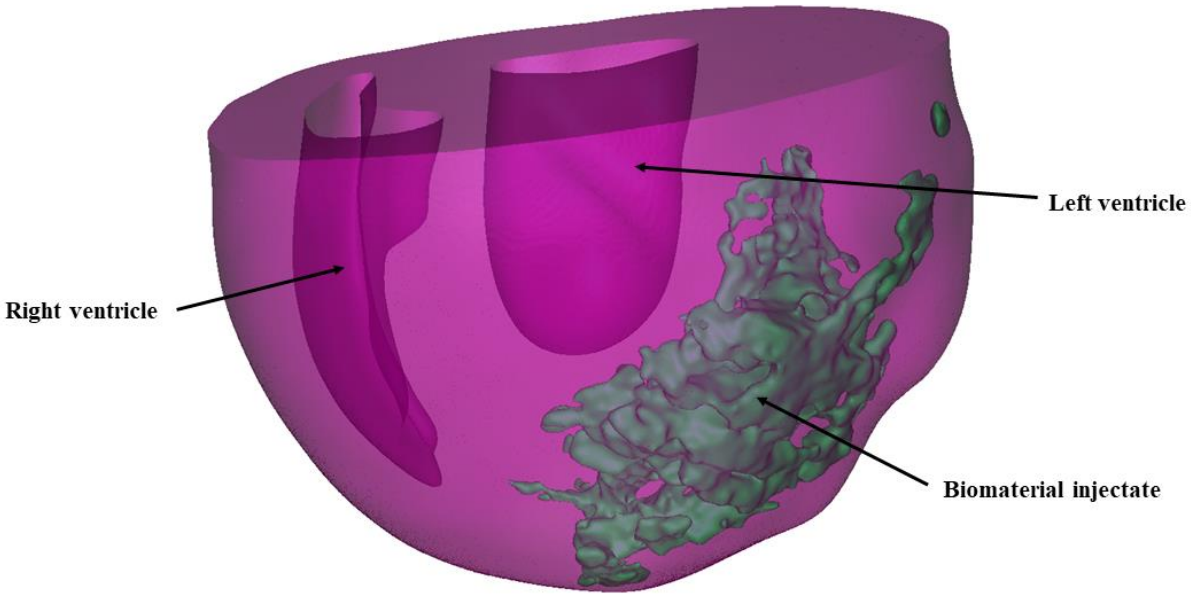

Figure 11. Biventricular geometry developed from μCT scan images in Simpleware. The LV, RV and a detailed dispersion of injectate are shown.

The alignment of the geometry with the long axis in the cardiac geometry is an essential condition to get realistic results, particularly for truncated geometries considered in the current study. The ventricular cavities (LV and RV) were not aligned with the long axis in the original geometry (Figure 12a). A new orientation was obtained (Figure 12b), where the longitudinal axis was aligned with the cavities. Compared with the original geometry, a difference in angle of about 20° was observed. The myocardial wall thickness, the myocardial volume, and the apex-base distance were compared for both geometries (see Table 7). The LV wall thickness at the truncated base (measured radially to the wall surfaces) was smaller in the rotated geometry compared to the original.

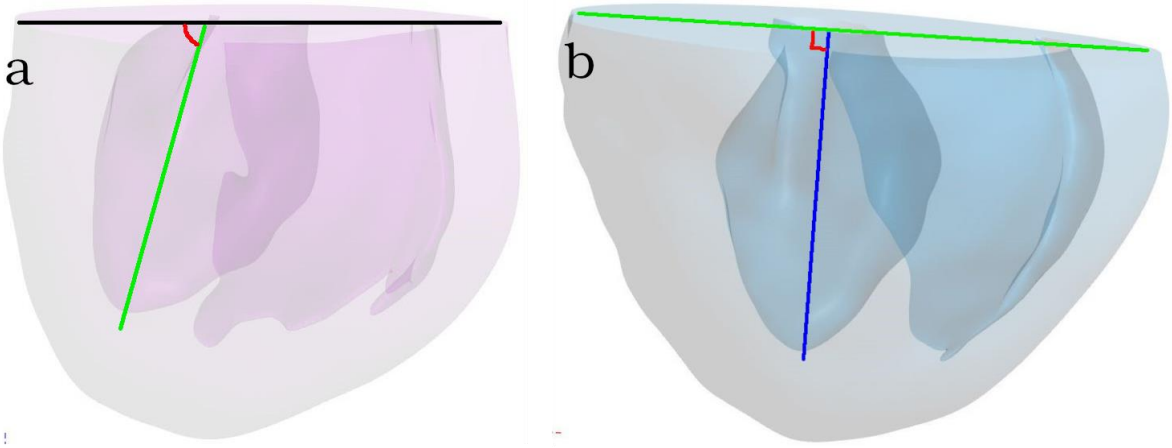

Figure 12. Rotation of the reconstructed rat heart geometry. The original geometry (a) and oriented geometry were obtained by a rotation of 20°.

Table 7. Comparison between original and rotated biventricular heart geometry. Myocardial volume, wall thickness and longitudinal length (distance base-apex).

	Rotated geometry	**Original geometry**
Myocardial volume (mm^3)	1,451	2,534
LV wall thickness (mm)	4.69 - 4.93	5.33 - 7.77
Septal Wall thickness (mm)	2.53 - 4.54	4.77 - 3.87
RV Free Wall thickness (mm)	1.74 - 3.24	2.94 - 1.73
Apex-Base length (mm)	13.94	12.12

3.1.2 Myocardial strain in the biventricular model and effect of injectate stiffness

The typical distributions of myofibre and the cross-fibre strain in the BV model at end-diastolic and end-systolic time points for an elastic modulus of the injectate of E_{inj} = 73.8 kPa are illustrated in Figure 13. The end-diastolic myofibre strain decreased from the endocardial to the epicardial surface, as also reported in other studies (Costa *et al.* 1999, Takayama *et al.* 2002, Waldman *et al.* 1988).

The deformation of the myocardium (healthy and infarcted tissue) was assessed through the myofibre and cross-fibre strain.

The end-diastolic myofibre strain decreased from 3.5% to 1.0%, and the median cross-fibre strain decreased in magnitude from -5.9% to -2.7% for increasing injectate stiffness (Figure 14). These changes in strain appear to be more pronounced in the low modulus region E_{inj} = 4.1 to 738 kPa and only marginal for E_{inj} > 738 kPa.

At end-systole, the median myofibre strain decreased in magnitude from -20.4% to -11.8%, with increasing elastic modulus. The median cross-fibre strain decreased from 6.5% to 4.6% with an increasing elastic modulus with an intermittent marginal increase for E_{inj} = 405.9 kPa and 738.0 kPa (Figure 15).

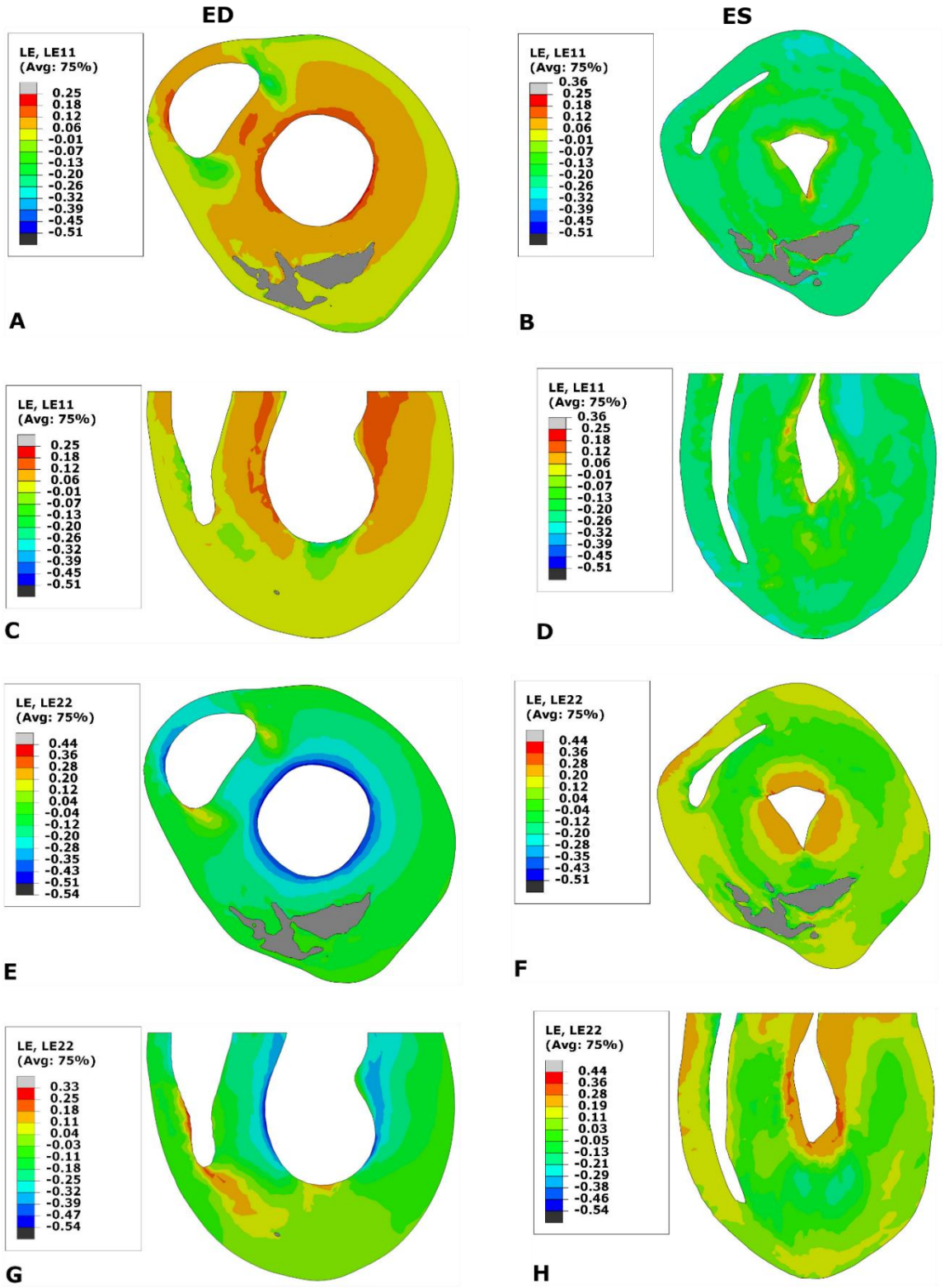

Figure 13. Short-axis and longitudinal contour plots showing myofibre strain (A-D) and cross-fibre strain (E-H) in the BV model at end-diastolic (left column) and end-systolic time point (right column) for E_{inj} = 73.8 kPa. The strain in the injectate is not displayed (grey areas).

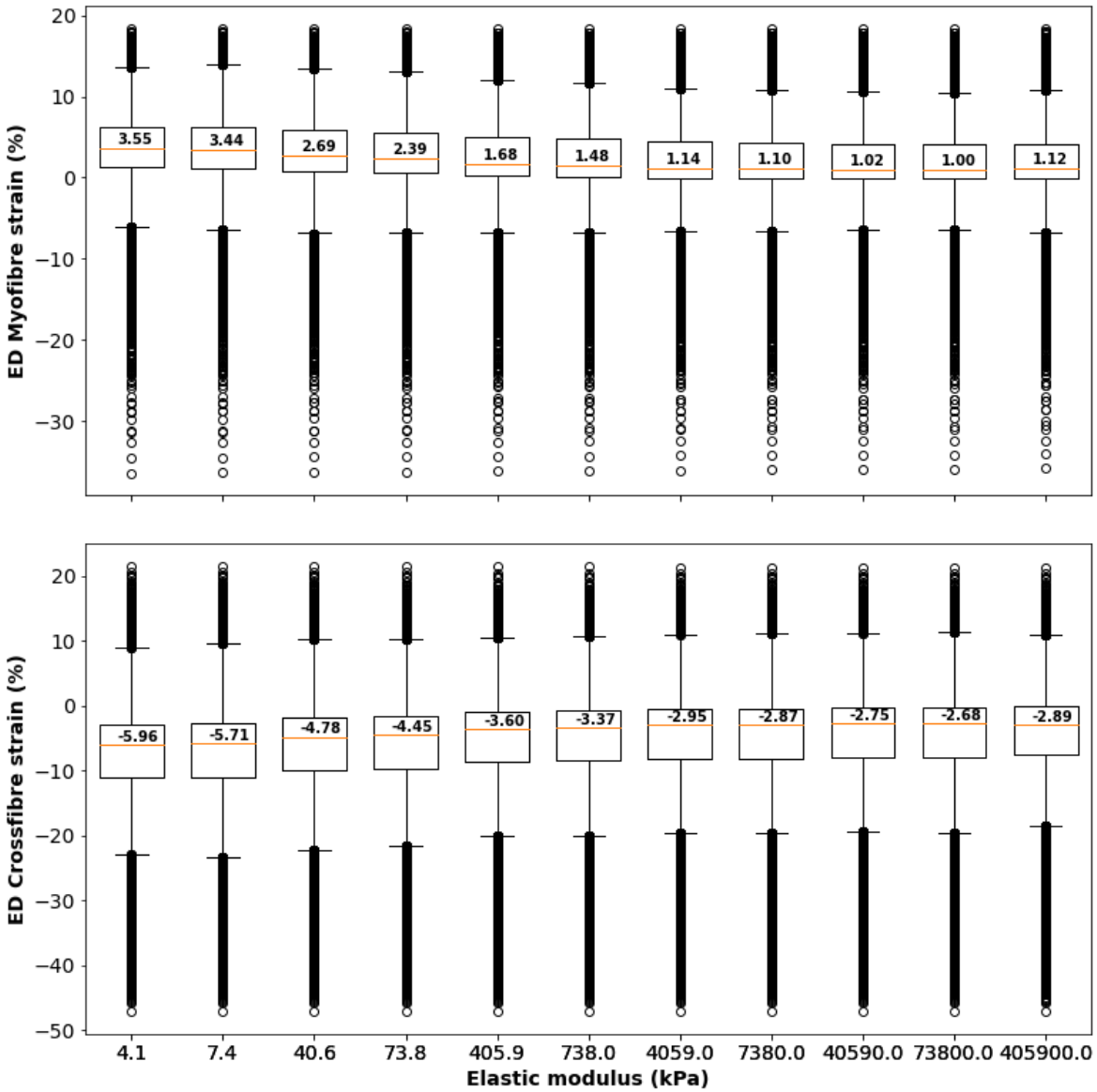

Figure 14. End-diastolic myofibre (top) and cross-fibre (bottom) strain in the myocardium for different injectate elastic modulus E_{inj} = 4.1 kPa to 405,900.0 kPa.

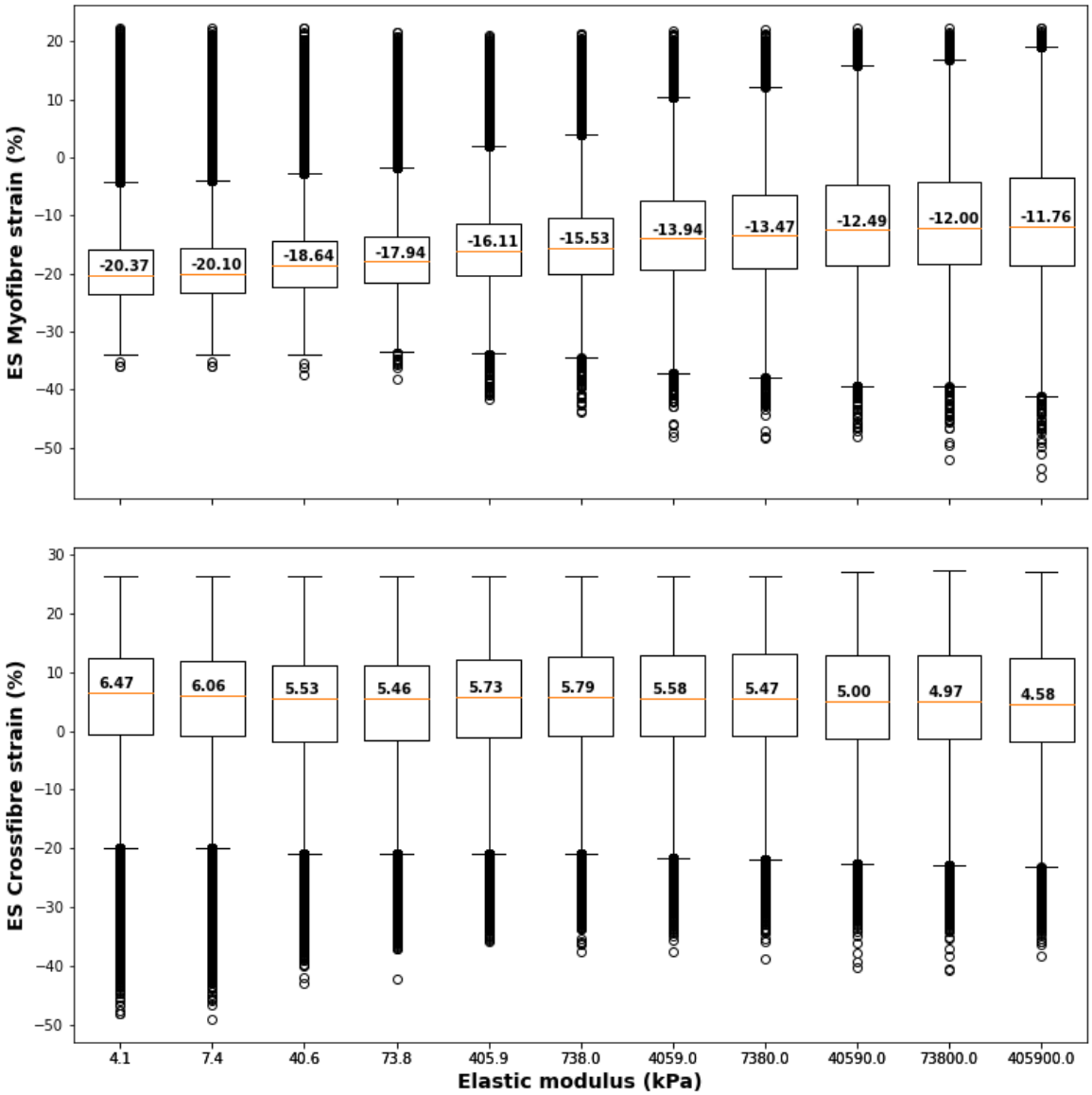

Figure 15. End-systolic myofibre (top) and cross-fibre (bottom) strain in the myocardium. The mesh-elements strains values are reported for different injectate stiffness (E_{inj} = 4.1 kPa to 405900.0 kPa).

3.1.3 Injectate deformation in the BV model and effect of the stiffness in a rat heart biventricular model

The end-diastolic and end-systolic maximum and minimum principal strains were reported in this section for the injectate region in the BV geometry. The median strains are presented to

describe the averaged deformation in the injectate for different elastic moduli. Boxplots are provided to analyse the variability in the mesh element strain data.

As a general observation, the magnitude (i.e. median), range (difference between the highest and lowest element strain) and interquartile range of maximum and minimum principal strain decreased considerably with increasing injectate stiffness for lower E_{inj} = 4.1 - 738 kPa. However, it only decreased marginally for the higher E_{inj} = 4,059 to 405,900 kPa, both at end-diastolic and end-systolic time points.

At end-systole, the median maximum principal strain decreased from 38.5% to 0.06%, and the median, minimum principal strain decreased in magnitude from -39.0% to -0.06% with increasing injectate stiffness (Figure 16).

At end-diastole, the median maximum principal strain decreased from 5.4% to 0.001%, and the median minimum principal strain decreased in magnitude from -5.4% to -0.001% for increasing injectate stiffness (Figure 17).

The ratio of ES to ED value of median maximum principal strain ranged from 7.2 (for the softest injectate) to 60 (for the stiffest injectate). The ES/ED ratio for the median, minimum principal strain similarly ranged from 7.3 (for softest injectate) to 60 (for stiffest injectate).

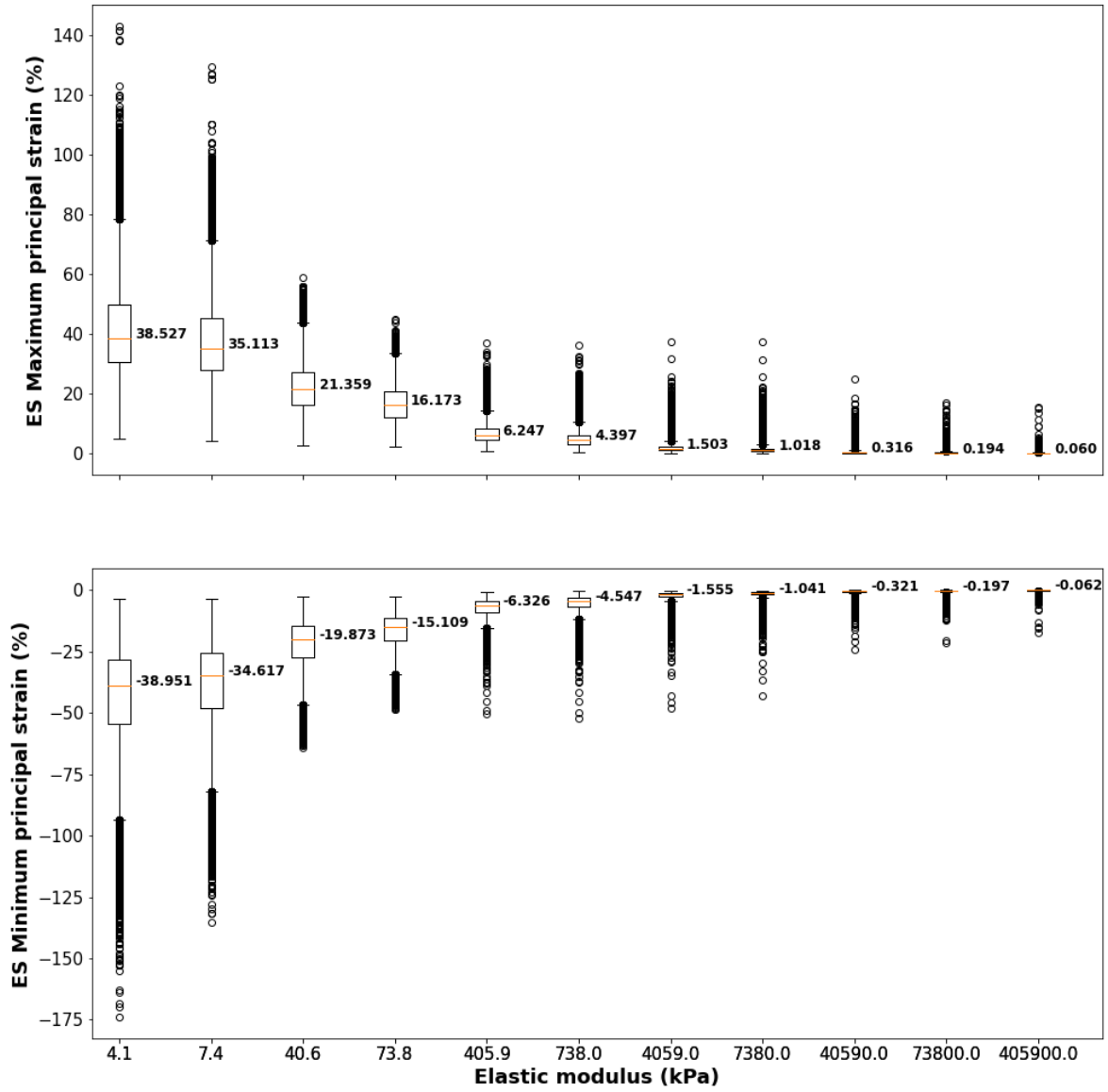

Figure 16. Box plot of end-systolic maximum and minimum principal strain in the injectate embedded in the BV geometry.

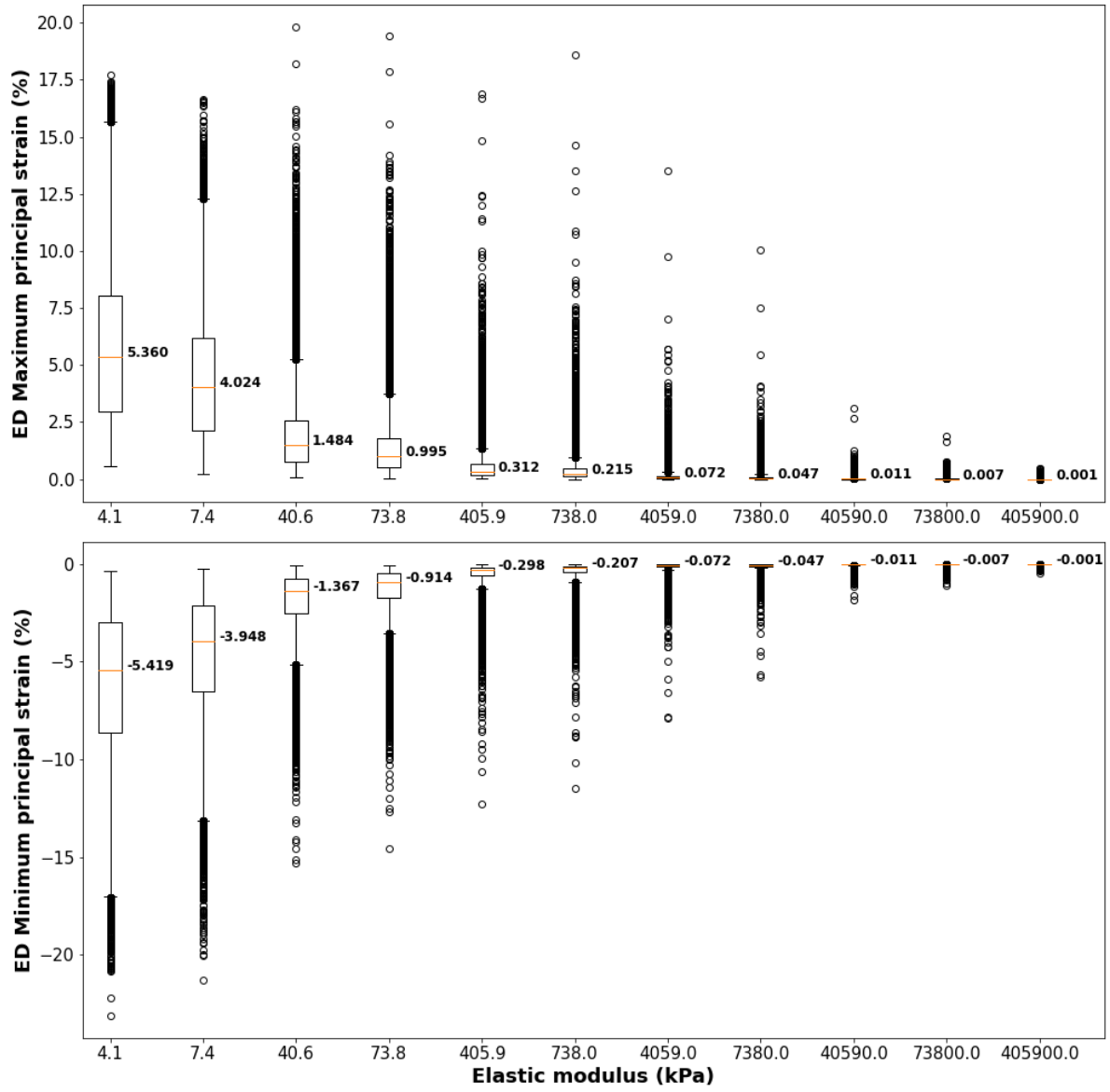

Figure 17. Box plot showing the end-diastolic maximum and minimum principal strain in the injectate region within the BV geometry.

3.2 Micromechanics of injectate and embedded cells in the infarcted rat heart

The geometry and the deformations in the extracted block (sub-model) are reported in this section. The micromechanics of the injectate and the embedded cells are investigated by analysing the maximum principal and minimum principal strains.

3.2.1 Geometry of the developed sub-model and embedded cells

The sub-model block geometry developed in Simpleware comprised three domains, i.e. myocardium, biomaterial injectate and idealised therapeutics cells. Nine cells were seeded in the injectate region, each cell featuring the three main components of a cell (membrane, cytoplasm, and nucleus, see Figure 18). The sub-model was meshed in Simpleware with 320,653 3D non-linear tetrahedral elements type. The dimensions of the sub-model block were 772 μm x 748 μm x 748 μm. The outer cell diameter was 65 μm, membrane thickness was 5 μm, and the nucleus diameter was 20 μm.

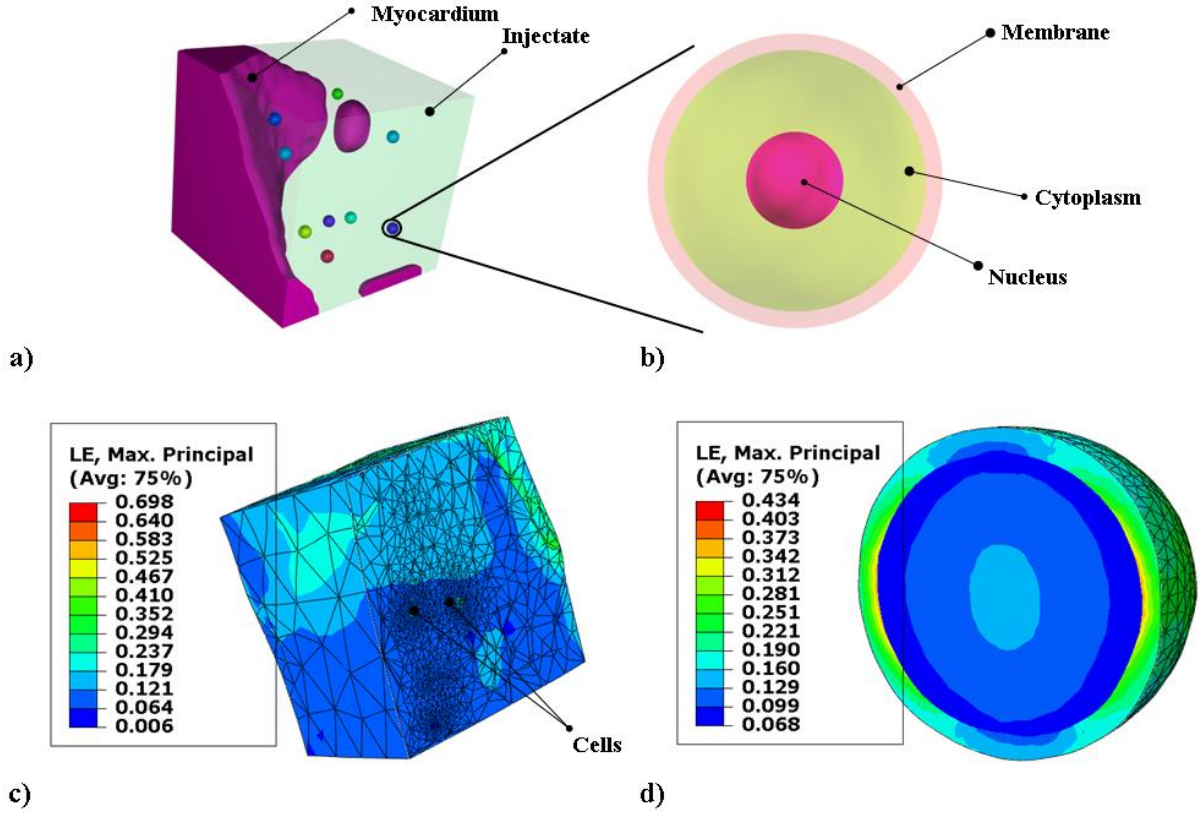

Figure 18.(a) Sub-model geometry showing the biomaterial injectate (green), the myocardium (purple) and (b) therapeutic cells (spherical shapes embedded within the injectate region). The cell geometry shows membrane, cytoplasm, and nucleus. FE mesh of the microstructural geometry (sub-model) showing (c) the maximum principle strain distribution in the block and (d) in a single cell.

3.2.2 Deformation of injectate in the sub-model

The maximum principal and minimum principal strain were presented at end-diastolic and end-systolic time points for the injectate region in the sub-model geometry.

At end-diastole, the median maximum principal strain decreased from 6.5% to 0.9%, and the median minimum principal strain decreased in magnitude from -7.3% to -0.9% with increasing injectate elastic modulus of E_{inj} = 4.1 to 405,900 kPa (Figure 19).

At end-systole, the median maximum principal strain decreased from 43.8% to 1.4%, and the median minimum principal strain decreased in magnitude from -38.0% to -1.5% with increasing injectate elastic modulus (Figure 20).

The ES/ED ratio of the median maximal principal strain varied from 6.7 (for the softest injectate, E_{inj} = 4.1 kPa) to 1.6 (for the stiffest injectate E_{inj} = 405,900 kPa). A similar decline was observed for the ES/ED ratio of the minimum principal strain from 5.2 for the softest injectate to 1.6 for the stiffest injectate.

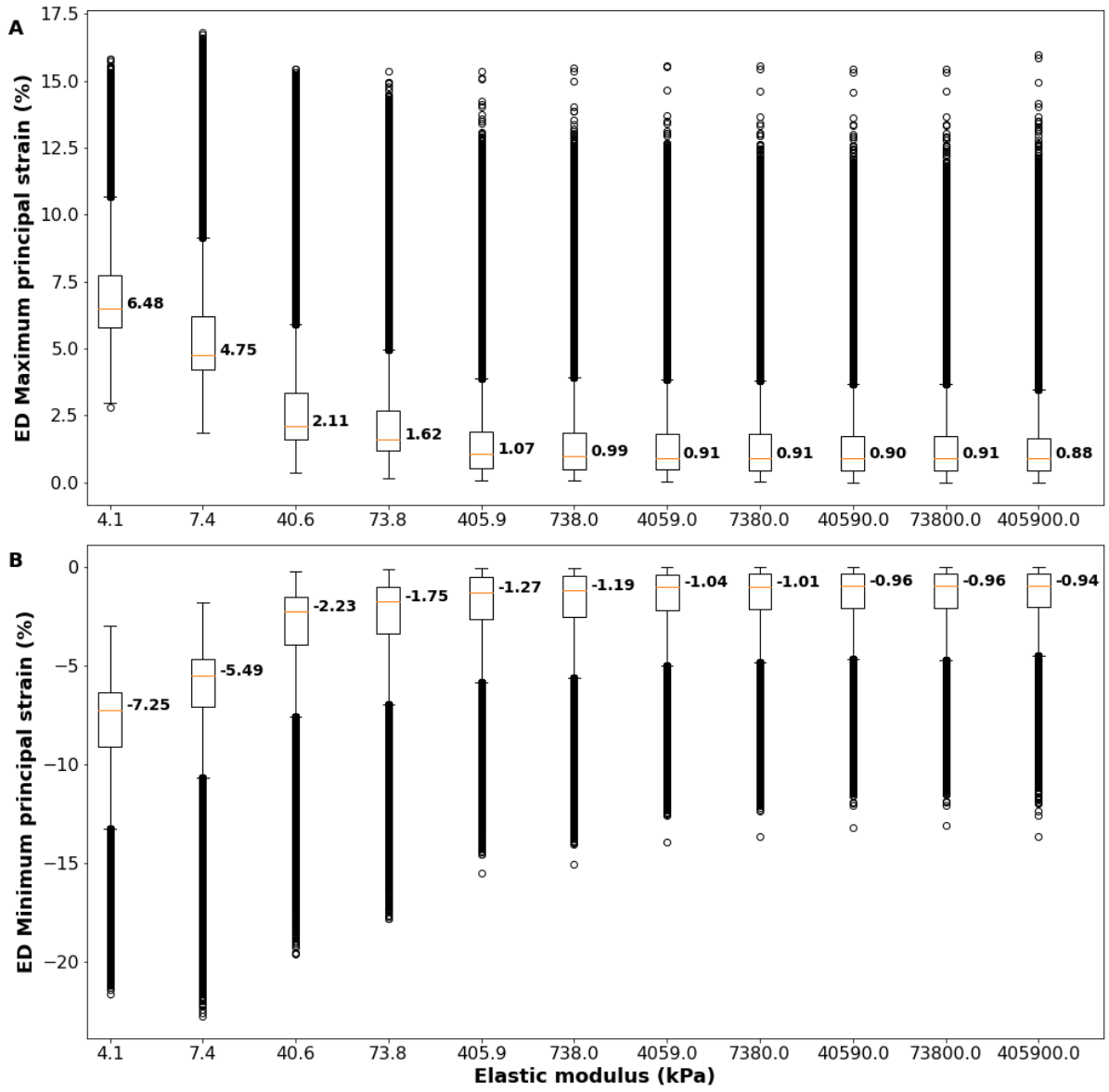

Figure 19. End-diastolic maximum principal strain (A) and minimum principal strain (B) in the injectate within the sub-model for different values of the injectate elastic modulus from 4.1 to 405,900 kPa. The orange line in the box indicates the median strain value.

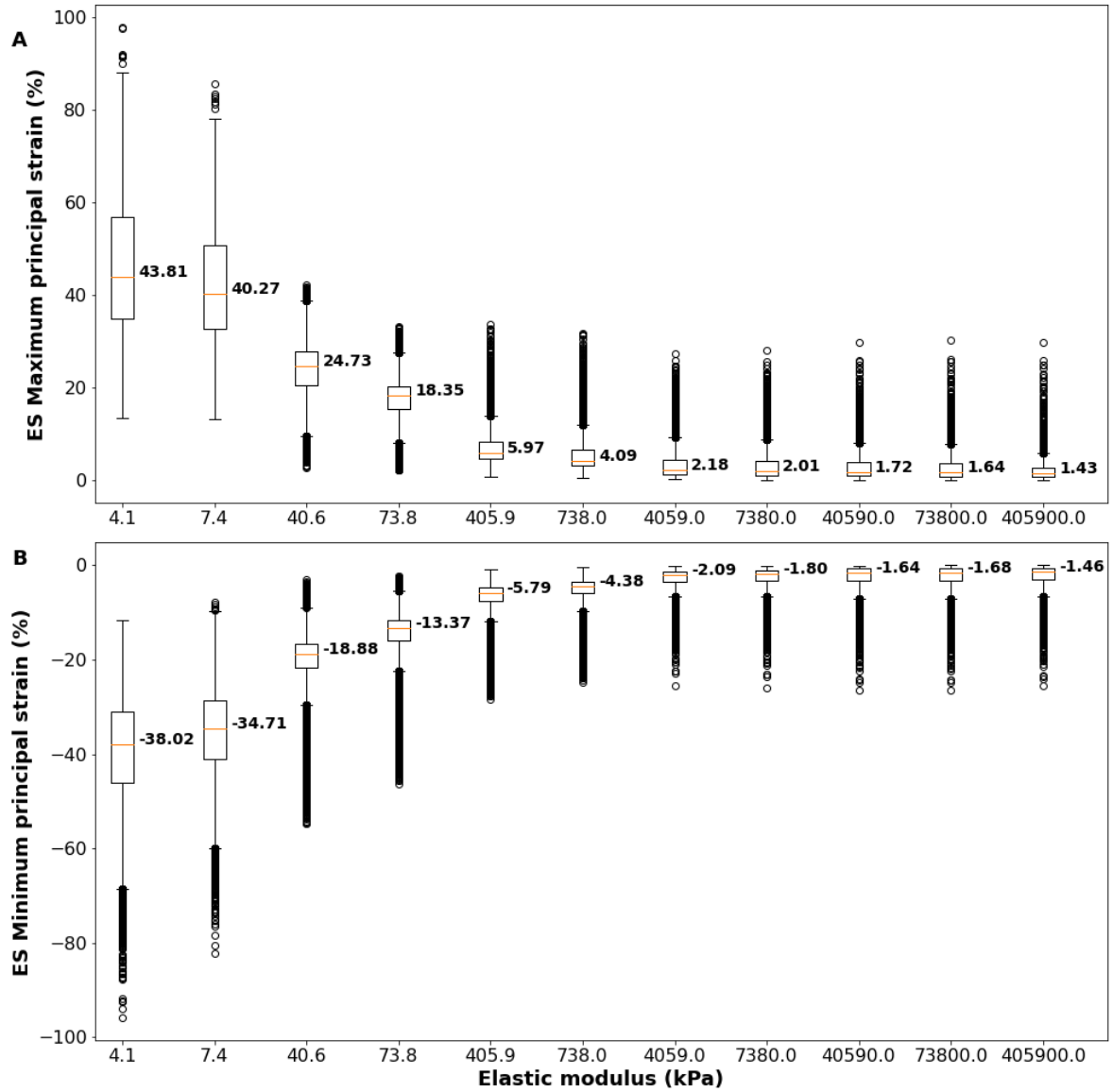

Figure 20. End-systolic maximum principal strain (A) and minimum principal strain (B) in the injectate within the sub-model for different values of the injectate elastic modulus from 4.1 to 405,900 kPa. The orange line in the box indicates the median strain value.

3.2.3 Deformation of cells embedded in the injectate

The deformation in the cell components was investigated by assessing the maximum and minimum principal strains at end-systole and end-diastole for eleven injectate elastic modulus

values E_{inj} = 4.1 kPa to 405,900 kPa. The strain data are reported for nine cells. For each cell component (membrane, cytoplasm, and nucleus), the volume-averaged strain distribution (for the nine cells) is presented with the median and interquartile range at end-systole and end-diastole since the data were not normally distributed according to Shapiro-Wilk normality tests. The ES-ED median range of maximum and minimum principal strain is also reported, reflecting the deformation range the embedded cells are exposed to during a cardiac cycle.

The end-systolic and end-diastolic maximum principal strain in the cell components decreased for increasing injectate elastic modulus E_{inj} = 7.4 kPa to 405,900 kPa. The decrease was more pronounced for the lower injectate elastic modulus E_{inj} = 7.4 kPa to 738 kPa compared to the upper range of the injectate elastic modulus of E_{inj} > 738 kPa. (Figure 21a,b,c).

The membrane displayed the highest strain compared to the cytoplasm and nucleus, which (nucleus and cytoplasm) have similar strains (see Figure 21).

The ES-ED range of the median maximum principal strains decreased for increasing injectate elastic modulus E_{inj} = 7.4 kPa to 405,900 kPa (Figure 21d).

Similar observations were found for the minimum principal strain, which exhibited negative (compressive) strain values. Here, the magnitude of the strain and the ES-ED strain range decreased for E_{inj} = 7.4 kPa to 738 kPa and levelled off for E_{inj} > 738 kPa as observed for the maximum principal strain, see Figure 22.

An increase in maximum and minimum principal strains at the end-systolic time point and consequently the associated ES-ED strain ranges were observed for the increase of injectate elastic modulus from E_{inj} = 4.1 kPa to 7.4kPa.

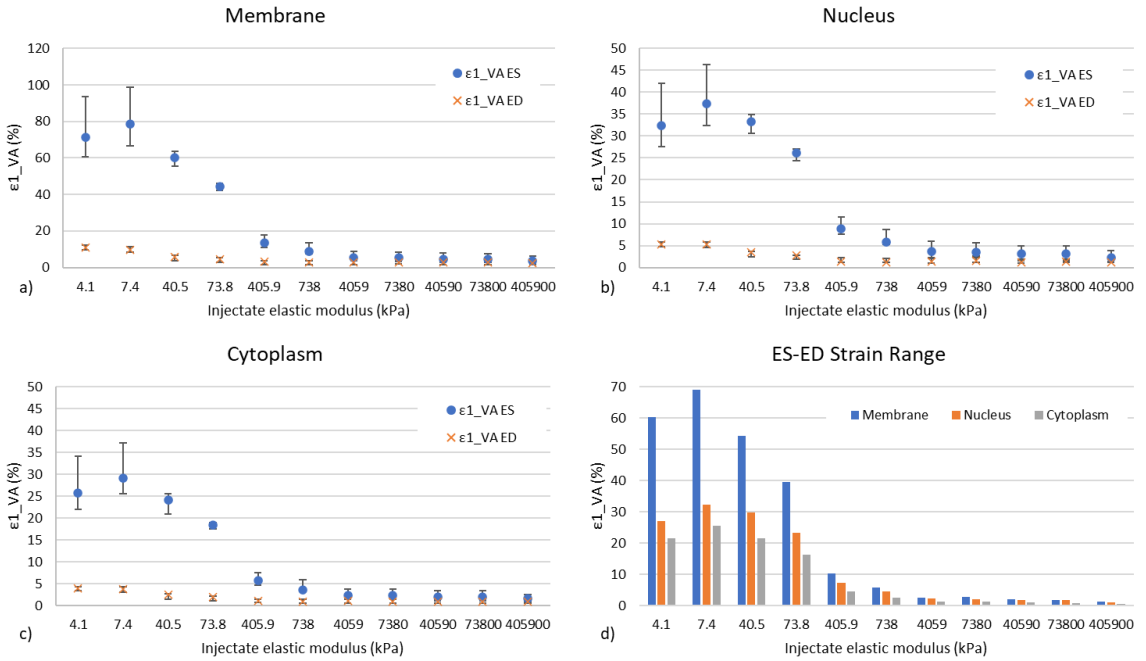

Figure 21. Maximum principal strain (ε_{1_VA}). Variation of end-systolic and end-diastolic volume-averaged strain with increasing injectate elastic modulus E_{inj} = 4.1 kPa to 405,900 kPa in the membrane (a), the nucleus (b), and the cytoplasm (c). ES-ED strain range versus injectate elastic modulus (d). (Data in a to c are presented as median and interquartile range).

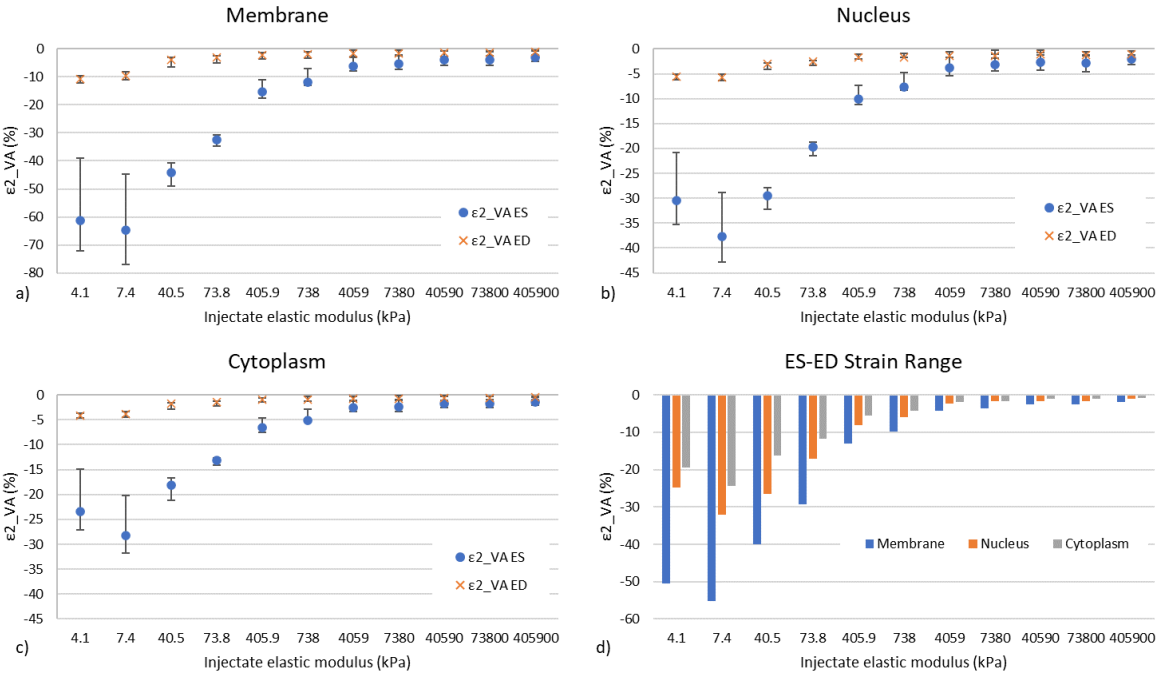

Figure 22. Minimum principal strain (ε_{2_VA}). Variation of end-systolic and end-diastolic volume-averaged strain with increasing injectate elastic modulus E_{inj} = 4.1 kPa to 405,900 kPa in the membrane (a), the nucleus (b), and the cytoplasm (c). ES-ED strain range versus injectate elastic modulus (d). (Data in a to c are presented as median and interquartile range).

3.3 Mechanically induced TGF- β production of therapeutic cells in the injectate

A model of the mechanically-induced production of TGF-β is presented to predict TGF-β mRNA expression in response to cellular deformations. First, results are shown from the finite element model of single-cell stretching (described in section 2.5.1) to mimic the experimental cell stretching study by Hirakata *et al.* (1997). The deformations in the cell induced by the substrate deformation are reported as maximum principal strain in the cell body and the focal adhesions. Secondly, a mathematical model describing the TGF-β expression induced by the substrate deformation is developed. Finally, a relationship is derived to express TGF-β expression as a function of cell deformation.

3.3.1 Finite element modelling of single-cell stretching on an elastic substrate

An optimised finite element mesh with 7,697, 1,186, and 122,694 elements in the cell body, focal adhesion and substrate, respectively, was selected following a mesh sensitivity study with a maximum of 15% biaxial strain in the substrate (see Figure 23 and Figure 24).

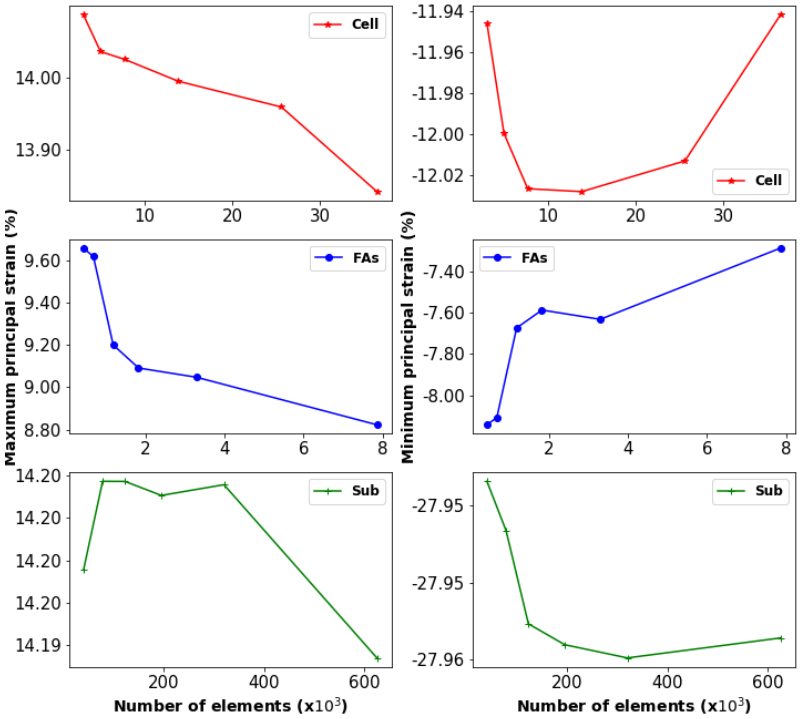

Figure 23. Mesh sensitivity study. Convergence of the maximum (left column) and minimum (right column) principal strain for increasing number of elements in the cell body (top), focal adhesions (middle) and substrate geometries (bottom) for a biaxial substrate strain of 15%.

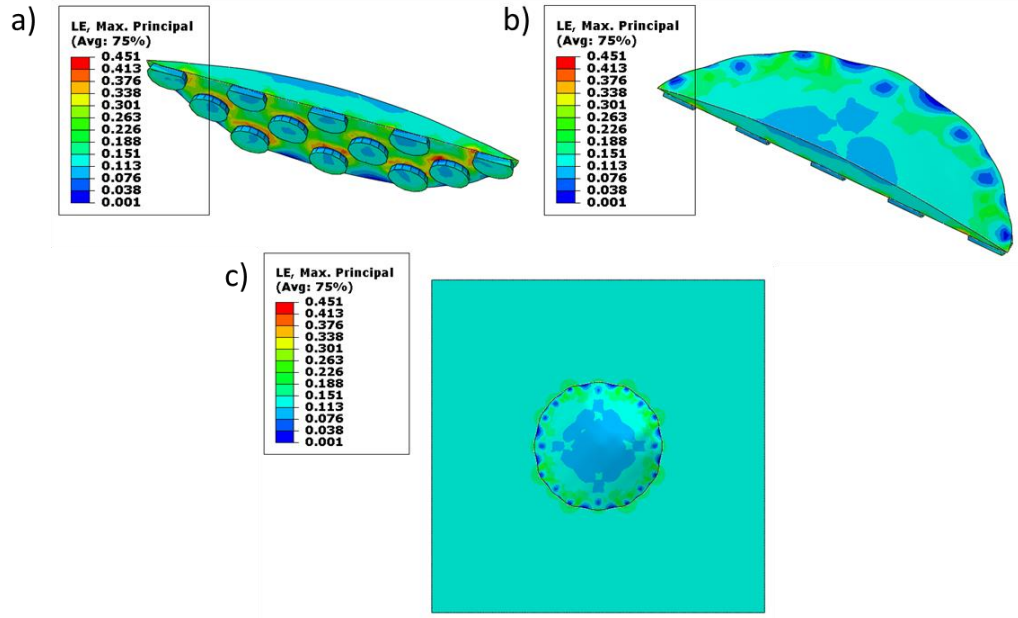

Figure 24. Contour plots of maximum principal strain in the focal adhesions (a), cell body (b), and substrate-cell assembly (c) from substrate biaxial strain of 15% for optimised mesh densities.

The mean volume-averaged maximum principal strain in the cell body and focal adhesions increased linearly with increasing substrate strain ε_{Sub} = 5% to 20%, see Figure 25. The relationship of the maximum principal strain in the cell with the substrate strain was expressed as a linear function:

$$\varepsilon_{Cell} = 0.84\,\varepsilon_{Sub} + 0.37, \tag{3.1}$$

where ε_{Sub} is the substrate strain ranging from 5% to 20%, and ε_{Cell} is the mean volume-averaged maximum principal strain in the cell body and the focal adhesions.

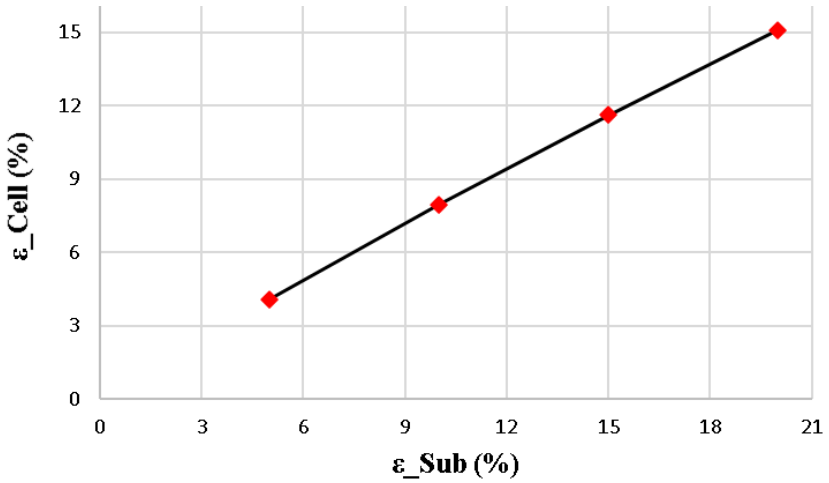

Figure 25. Mean volume-averaged maximum principal strain in a single cell stretched on an elastic substrate. The finite element model computed volume-averaged strain (red squares) is shown with the strain predicted in the cell for increasing substrate strain with Eqn. (3.1) (solid line).

3.3.2 Mathematical modelling of mechanically-induced TGF-β expression

A linear fit of the relationship of the cell deformation with TGF-β expression was obtained using experimental data by Hirakata *et al.* (1997) and the finite element results (from section 3.3.1).

Quantitative data of the TGF-β expression as a function of substrate strain were extracted from Hirakata *et al.* (1997), Figure 3. Four data pairs were obtained, each corresponding to the

substrate strain and the expression of TGF-β, see Figure 26. The linear function of TGF-β expression with substrate strain is given by:

$$[\text{TGF-}\beta] = 0.06\,\varepsilon_{\text{Sub}} + 0.08, \tag{3.2}$$

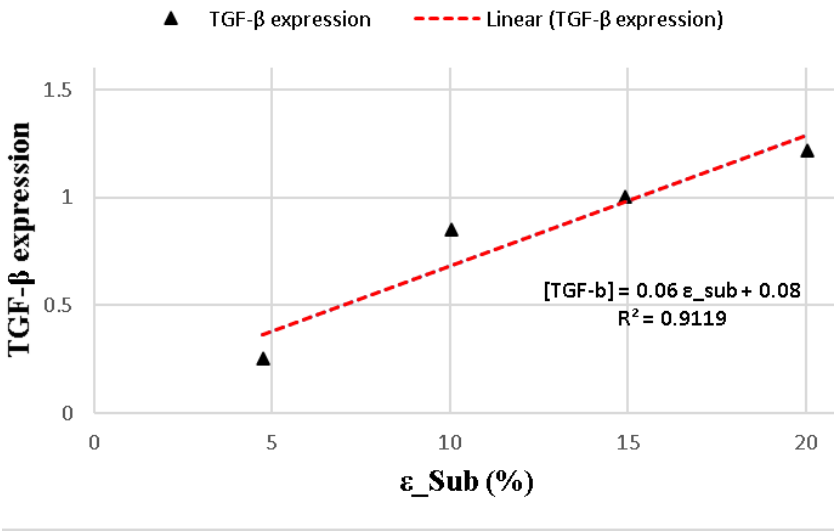

Figure 26. Linear fit of TGF-β mRNA expression in a stretched cell on an elastic substrate. The experimental data of TGF-β mRNA expression (black triangles) and the linear fit (red dashed line) are shown for increasing substrate strain ε_{Sub} = 5% to 20%.

The results from the finite element model and the mathematical model were used by combining Eqns. (3.1) and (3.2) to obtain TGF-β mRNA expression as a function of cell strain as shown in Eqn. (3.3) and Figure 27:

$$[\text{TGF-}\beta] = 0.07\,\varepsilon_{\text{Cell}} + 0.11, \tag{3.3}$$

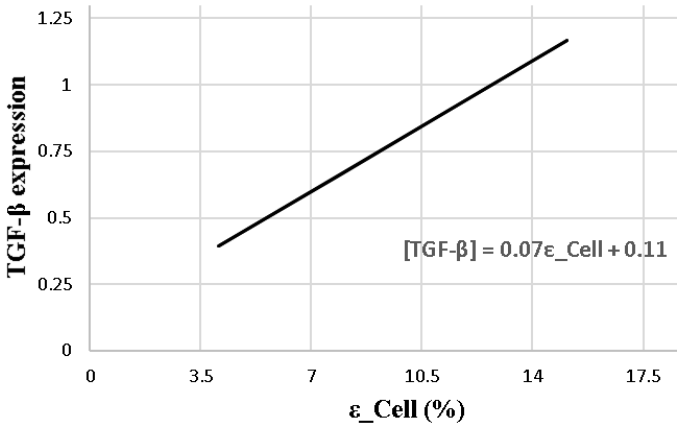

Figure 27. Expression of mechanically-induced TGF-β mRNA versus mean volume-averaged maximum principal strain in the cell.

3.3.3 Prediction of TGF-β expression in cells embedded in the intramyocardial injectate

The TGF-β mRNA expression of the cells embedded in the biomaterial injectate decreased with increasing injectate stiffness. The expression of TGF-β in the injected cells was determined using Eqn. (3.3) and the ES-ED ranges of maximum principal strain in the cells (Figure 21d). However, considerable extrapolation beyond the strain range considered by Hirakata *et al.* (1997) was required, and it was assumed that the linear relationship is valid in the ES-ED strain range domain.

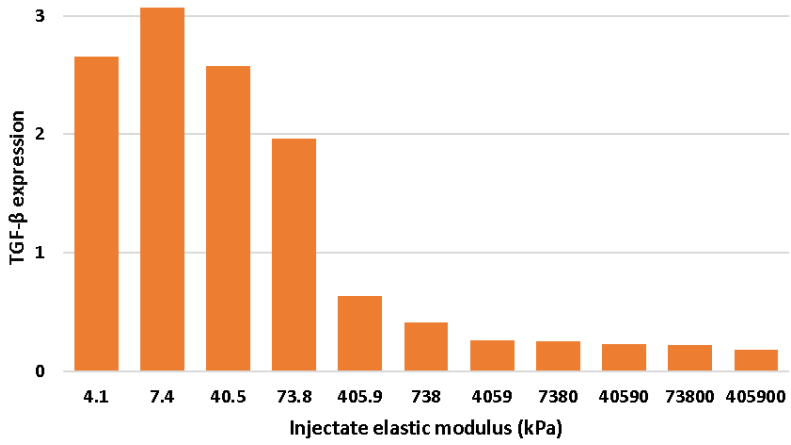

Figure 28. TGF-β mRNA expression in embedded cells versus injectate elastic modulus E_{inj} = 4.1 kPa to 405,900 kPa.

Chapter 4 Discussion

Understanding the cellular signalling mechanism involved in the cardioprotective effect following the intramyocardial injection of the therapeutic cells embedded in a carrier biomaterial for MI treatments is critical for optimising the cell-based therapy. The present computational study involved the development of computational models for cardiac mechanics at different scales. The effect of the stiffness of the biomaterial injectate on the mechanics and TGF-β expression of the injected cells during a cardiac cycle was shown using the developed models. The findings demonstrate that variation of the injectate stiffness can be used to guide deformation and associated biochemical signalling of cells embedded in the injectate. In particular, the injectate with the low stiffness values investigated promise beneficial effects as cell deformation is more sensitive to a change in stiffness compared to the higher stiffness values.

4.1 Computational model of an infarcted rat heart with biomaterial injectate

4.1.1 Biventricular geometry and finite element model of the rat heart with *in situ* biomaterial injectate

Many cardiac computational modelling studies involving animal species used simplified geometries to reduce the computation time and the data size (Dieudonné 1969, Wall *et al.* 2006, Wenk *et al.* 2009). The current study was the first to reconstruct a subject-specific biventricular geometry of a rat heart with a realistic dispersed biomaterial injectate for finite element analysis. The model highlights details in the rat heart morphology and the micro-structural injectate dispersion in the LV wall. This achievement was possible with advanced tools in

computational and image processing. The details achieved in reconstructing the accurate geometry resulted in a considerably higher and heterogeneous mesh density in the model.

The reconstruction of the biventricular geometry and the development of FE mesh adopted a validated method developed in our research group, see Sack *et al.* (2018). Hence, a mesh sensitivity study was not deemed necessary.

The high-performance computing (HPC) facility at the University of Cape Town was essential to run simulations and, more importantly, for the feasibility of the parametric studies where eleven different injectate stiffnesses were used.

4.1.2 Constitutive models of a rat myocardium and embedded injectate

Different strain energy density functions were used for the myocardial and injectate regions in the model, contrary to studies that used the homogenisation approach to represent the biomaterial injectate (Wall *et al.* 2006, Wenk *et al.* 2011). The meshed geometries distinguished the myocardium and the injectate regions, treated separately with different material properties. This approach considered the mechanical anisotropy in the myocardium, which is not present in the injectate.

The passive myocardial material parameters used in the current study were adopted from Dương *et al.* (2018), where the same animal model (rat) was used and, the parameters were validated by comparing stress-strain curves with experimental data by Sirry *et al.* (2016). The active contraction in the healthy region of the BV myocardium was modelled with a validated time-varying elastance model (Guccione *et al.* 1993). The parameters estimated by Guccione *et al.* (1993) for the canine model have been used in several studies involving rats (Wise *et al.* 2016) and porcine (Sack *et al.* 2018) models.

4.1.3 Mechanics of infarcted rat heart

Therapeutic intramyocardial biomaterial injectates with different mechanical properties may result in different biomechanical responses and cardiac functions of the infarcted heart. The current study showed that an increasing elastic modulus (i.e. stiffness) of the biomaterial injectate reduces the ES and ED strains in the myofibre and cross-fibre directions within the

biventricular wall, including the healthy and infarcted regions.

In several studies that investigate the impact of injectates on the infarcted heart, a reduction in the wall stress from non-treated to treated infarct was observed and identified as a critical factor for ventricular biomechanical and function improvement (Kichula *et al.* 2014, Kortsmit *et al.* 2013a, Miller *et al.* 2013, Sirry 2015).

Additionally, increasing the injectate stiffness reduced cardiac ventricular wall stress (Kichula *et al.* 2014, Sirry 2015). In the current study investigating the strain in the entire BV geometry, the increase of the injectate elastic modulus led to reduced myofibre and cross-fibre strain in the healthy region of the BV geometry. This finding may suggest that increasing the elastic modulus of injectate for MI treatment may result in a mechanical beneficial effect by reducing the myofibre and cross-fibre strains in the healthy region of the BV geometry.

4.1.4 Mechanical responses of the injectate

The biomaterial injectate is the environment of therapeutically delivered cells for MI treatment. Thus, the mechanical response of the injectate is crucial for the mechanics and the associated signalling of the embedded cells.

The current study showed that the response of the injectate depends on its stiffness. For increasing injectate elastic modulus, the maximum and minimum principal strain decreased.

The upper range of the elastic modulus (E_{inj} > 738 kPa) used in the study is unrealistic for PEG hydrogels or other injectable biomaterials (Rizzi *et al.* 2006, Singelyn *et al.* 2012). However, the current study aimed to explore the wide range of injectate stiffness and predict the injectate response. It was shown that the deformations induced in the injectate are negligible from a particular threshold of the injectate elastic modulus.

4.2 Mechanics and mechanotransduction of cells in biomaterial injectate delivered to the infarct region

One of the promising approaches to promoting regenerative processes in a damaged heart following myocardial infarction is stem cell therapies. The goal is to produce cardiac-like cells, initiate growth factor expression necessary for neo-vascularisation and angiogenesis or inhibit cardiomyocyte death through paracrine signalling (Kocher *et al.* 2001, Shudo *et al.* 2013). Despite the advances and the increasing number of studies dedicated to cellular and biomaterial therapies, the mechanisms underlining the cardioprotective impact of injectates and cell-based therapies remain unclear.

It is well established that cyclic mechanical loads *in vivo* and *in vitro* induce biochemical responses in cells (Seko *et al.* 1999, Shradhanjali *et al.* 2017, Tian *et al.* 2016, Zheng *et al.* 2001). Bhang *et al.* (2010) showed that cyclic mechanical strain (i) promotes the expression of cardiomyogenic markers in bone marrow-derived mesenchymal stem cells (BMMSCs) and (ii) in combination with TGF-β leads to enhanced expression of cardiac-specific genes.

The current study aimed to determine (i) the mechanics and associated TGF-β expression of cells delivered with the biomaterial injectate and (ii) the effect of the mechanical injectate properties on cellular signalling to guide the treatment and optimise the therapeutic benefit.

The study showed that delivered cells mechanics and associated signalling, e.g., TGF-β expression, are more sensitive to stiffness changes in soft injectates than stiff injectates. These findings suggest that the stiffness of soft injectates may be employed to guide the cardioprotective effects in the infarcted heart in the context of treatment with deliverable biomaterial.

4.2.1 Microstructural finite element modelling

The sub-modelling approach used in the current study connected the BV model (at the tissue level) to a microscale structural model (sub-model at the cellular scale) and allowed a transition from BV mechanics to cellular micromechanics. The sub-modelling method was adopted from Sirry (2015), who extended 2D mask of histological images to obtain the 3D geometry of the

myocardium and injectate sub-model composite. The current study used a similar approach to derive the microstructural sub-model geometry. However, the 3D geometry was obtained from resampling the BV model, offering a more realistic microstructure representation. Furthermore, the resolution of the original μCT scan images provided sufficient details in the microstructure to consider cellular dimensions in the injectate region.

The microstructural block model was obtained by resampling the biventricular geometry, and it captured fine morphological details of the injected biomaterial, infarcted tissue, and cells embedded in the injectate. The resampling consists of downscaling the spacing parameters in x, y, and z-directions in the image set. Correct spacing in x, y and z was required to obtain realistic geometry and preserve the original morphologies. More importantly, the spacing must be small enough to generate cell geometries and meshes representing the cellular component with several mesh layers. This precaution was specifically important for the cell membrane that is the thinnest structure (thickness 3 to 5 μm).

4.2.2 Micromechanics of the injectate

The mechanical properties of the deliverable biomaterial are a crucial factor for successful cell therapy because the delivered cells reside in the injectate. The injectate provides mechanical support to the impaired tissue to inhibit the adverse remodelling. The biomaterial injectate further serves as a physical environment for the therapeutic cells and prevents them from flowing out of the region of interest. The sub-model study showed the impact of injectate stiffness on its deformation at a microscopic length scale, namely the decrease in strain in the injectate for increasing E_{inj}. Similar observations were reported by Sirry *et al.* (2015), where stiffer injectate resulted in less deformation within an acellular injectate region of the sub-model. The agreement of these findings confirms the appropriateness of the size and location of the representative volume element as a sub-model.

4.2.3 Cell mechanics in the biomaterial injectate

To the author's knowledge, this study is the first to use a computational approach to investigate therapeutically injected cell mechanics and the associated signalling for MI treatment. It was

found that the cells' ES and ED strain, respectively, and the associated ES-ED strain range decreased for increasing injectate stiffness. Moreover, it was observed that the cell mechanics was considerably more sensitive to environmental stiffness changes for soft injectates (with $E_{inj} \leq 738$ kPa) than stiff injectates (with $E_{inj} > 738$ kPa).

During a cardiac cycle and the related myocardial deformations, the cells embedded in the injectate are exposed to the strain range between end-systole and end-diastole. The deformation in the injectate is transferred to the embedded cells and controls their mechanical responses.

In contrast to the decrease in cellular deformation observed for an increase of the injectate modulus of $E_{inj} \geq 7.4$ kPa, an increase in cell strain was observed for the increase of injectate stiffness from Einj = 4.1 kPa to 7.4 kPa. This contrasting cell behaviour may reveal a threshold of the injectate stiffness at which the mechanical response of the cells changes. This change may be explained when considering the elastic modulus of the cell, i.e. the cellular components, namely E = 1.7, 8 and 5 kPa for the membrane, cytoplasm and nucleus, respectively. The softest injectate with $E_{inj} = 4.1$ kPa used in the study has, as such, a lower elastic modulus than the bulk of the cellular structure (i.e. cytoplasm and nucleus). The softest injectate will transfer a smaller deformation to the cells than the injectate with the next higher elastic modulus of $E_{inj} = 7.4$ kPa closer to the elastic modulus of cytoplasm and nucleus.

The strain distribution in the cellular components exhibited a near-uniform distribution, providing little information about the variability in cellular deformation depending on the location of the cells in the injectate.

4.2.4 Single-cell model for TGF-β expression induced by biaxial stretching

Several computational studies investigated cell mechanics in stretching experiments, focusing on the role of focal adhesion or the effect of substrate stiffness (Abdalrahman *et al.* 2017, Kohn *et al.* 2019). The experimental cell stretching study performed by Hirakata *et al.* (1997) and its implementation in the finite element model in the current study revealed a linear increase in cell strain for increasing substrate strain. Similar results were reported by Abdalrahman *et al.* (2017), where the global deformation of a single cell increased linearly for an increasing substrate strain.

A FE model allows predicting the deformation within a cell from a measurable substrate displacement, which is difficult to measure and was not provided by the experiments done by Hirakata *et al.* (1997). This FE approach can be transferred to the cellular and intracellular deformation induced by the injectate deformation as a three-dimensional cellular environment (discussed in the previous section).

In the current study, the mathematical model developed from the experimental work by Hirakata *et al.* (1997) showed a linear increase of TGF-β with an increase in biaxial substrate strain (5 to 20% biaxial strain). The results of the finite element model associated with the mathematical model demonstrated a linear relationship between the cell strain and the expression of TGF-β.

4.2.5 Mechanically-induced TGF-β expression of cells embedded in the intramyocardial biomaterial injectate

The developed mathematical model for strain-induced TGF-β expression in cells allowed to determine the cellular TGF-β expression in response to the deformation underwent by therapeutic cells in an intramyocardial injectate during a cardiac cycle (i.e. ES-ED strain range).

A study by Bhang *et al.* (2010) confirmed the expression of TGF-β based on cellular mechanics. The current study revealed a higher sensitivity of TGF-β expression to a change in the environmental stiffness for low injectate stiffnesses ($E_{inj} \leq 738$ kPa) compared to high injectate stiffnesses ($E_{inj} > 738$ kPa). These observations agreed with several studies that report the effect of cyclic mechanical stimuli on growth factor expression (Bhang *et al.* 2010, Kichula *et al.* 2014).

The developed model allowed to identify a range of injectate stiffness susceptible to optimise the cellular mechanics and the production of TGF-β necessary for regenerative signals and neo-vascularisation in the damaged tissue.

The injectate stiffness affects the injectate deformations, which guide the deformations in the injected cells. Based on these results, injectate stiffness plays an essential role in the cellular growth factor expression in therapeutic intramyocardial injectates and cardioprotective signalling in the infarcted heart.

Chapter 5 Conclusions and recommendations

5.1 Conclusions and novel aspects

This study aimed to (i) develop computational models for predicting the mechanics and associated signalling of cells delivered in a carrier biomaterial intramyocardially for the treatment of myocardial infarction, and (ii) demonstrate the feasibility of the developed models to investigate and optimise therapeutic cell therapies for myocardial infarction. The following objectives were defined to achieve these aims:

1) To develop a 3D subject-specific biventricular geometry of a rat heart with a left ventricular infarct and biomaterial injectate.
2) To develop a small mid-wall volume of the infarcted LV region (sub-model) with microstructural details of the infarcted tissue and interlaced biomaterial injectate, representing a micro-environment for the delivered cells (microscopic scale).
3) To develop a finite element model of a single cell with an idealised spherical geometry. The three-component cellular model will represent the cell membrane, the cytoplasm and nucleus with different material properties.
4) To investigate the relationship between computationally predicted deformation and related biochemical responses of the cells, e.g. VEGF or TGF-β production, based on existing experimental data on GF production in stretched cells.
5) To employ the developed methods and models to investigate the effect of treatment parameters on cellular signalling and therapeutic benefit.

All objectives were achieved, and the previous chapter presented the outcomes. The sections below summarise the study's findings and novel aspects for the objectives. The relevant results are emphasised, and recommendations are made based on limitations in the methods and models developed.

5.1.1 Biventricular model of rat heart with infarct and biomaterial injectate (objective 1)

A 3D biventricular geometry of an infarcted rat heart with infarct and biomaterial injectate in the left ventricular free wall was reconstructed from *ex vivo* μCT data. The developed model featured a realistic representation of the biomaterial delivered one week after infarct induction into the infarct region. The reconstructed geometry was used to develop a subject-specific finite element model of an infarcted rat heart with biomaterial injectate and investigate the effect of the injectate stiffness on ventricular and injectate mechanics.

The end-systolic and end-diastolic myofibre and cross-fibre strain in the ventricular walls and maximum and minimum principal strain in the biomaterial injectate decreased in magnitude with increasing injectate stiffness.

These findings fulfilled objective 1 and contributed to objective 5 of the current work.

Novelty: This is the first computational study that (a) generated and used a high-resolution microstructurally detailed geometry of an *in situ* biomaterial injectate in a biventricular geometry, and (b) fundamentally assessed the effect of injectate stiffness with 11 values of the biomaterial elastic modulus between 4.1 and 405,900 kPa.

5.1.2 Microstructural modelling of myocardium, injectate and cells (objective 2)

A microstructural finite element model with geometrical details of myocardium and biomaterial injectate at cellular length scale was developed from the *ex vivo* μCT data to investigate the tissue and injectate micromechanics and the role of cell mechanics in a therapy that utilises stem cells delivered in a biomaterial for MI treatment. The geometry represented a mid-wall region of 748 μm x 748 μm x 722 μm in the infarcted LV free wall with infarcted myocardium and biomaterial injectate. Boundary displacements of the mid-wall region during a cardiac cycle were obtained from the biventricular FE model and applied to the microstructural model, connecting organ/tissue scale to tissue/cellular length scale. The developed model predicted a reduction in ES and ED maximum and minimum principal strain

in the injectate with an increase in the injectate stiffness. This reduction was most pronounced for soft injectates with E_{inj} up to 405.9 kPa.

This approach provided the framework to investigate the mechanics of cells delivered within a therapeutic biomaterial for MI treatment. The results are essential for predicting and understanding the mechanical responses underwent by stem cells carried in the therapeutic biomaterial.

These outcomes fulfilled objective 2 of the current study.

Novelty: The *ex vivo* μCT of the infarcted rat heart with biomaterial injectate provided a detailed microstructural geometry, a finite element model of the infarcted myocardium, and a dispersed biomaterial. In the only prior study of Sirry *et al.* (2015), the injectate geometry was based on cryo-light microscopy imaging with a lower resolution, particularly along the longitudinal direction.

5.1.3 Mechanics of cells embedded in intramyocardial injectates (objective 3)

Cell geometries were developed and incorporated at random locations in the injectate region of the microstructural finite element model (described in the previous section). The model was employed to investigate the mechanical response of intramyocardially injected cells in the infarcted heart during a cardiac cycle. The biventricular and microstructural finite element models were coupled to transfer deformation from organ and tissue to cellular scale.

The ES-ED strain range analysis revealed that the maximum cellular deformation was obtained for Einj = 7.4 kPa. This elastic modulus was similar to that of cytoplasm and nucleus of the stem cells in the injectate. The cellular strain decreased both for decreasing and increasing injectate stiffness. The variation of cellular strain was considerably higher for soft injectates with E_{inj} up to 405.9 kPa than for stiff injectates with an elastic modulus of 738 kPa and above.

The model and findings provide input for investigating the deformation-induced biochemical responses in therapeutic cells, i.e. cellular signalling induced by external mechanical forces.

This work fulfilled objective 3 and contributed to objective 5.

Novelty: The current study is the first to quantify the cellular mechanical response in a therapeutic biomaterial injectate environment for myocardial infarction treatment. The developed models will help predict cellular mechanical responses for biomaterial-based therapies for myocardial infarction.

5.1.4 Mechanically driven cell signalling (objective 4)

Mathematical formulations were developed by coupling a finite element model for single-cell stretching and a cell stretching experimental data from the literature to investigate the relationship between the deformation of the delivered stem cells and the mechanically induced cellular signalling.

A mathematical formulation for cellular TGF-β expression in response to substrate strain was developed from experimental data from a study by Hirakata *et al.* (1997).

A single-cell finite element model on an elastic substrate was developed to link intracellular deformation to substrate strain. Displacement boundary conditions were applied to the substrate to generate biaxial strains up to 20%, mimicking Hirakata et al. (1997) experiments on cellular TGF-β expression induced by substrate strain.

The coupling of the two mathematical relationships formulations linked cellular TGF-β expression to intracellular deformation during a cell stretching experiment.

This work fulfilled objective 4 of the study.

Novelty: The developed mathematical model for single-cell strain-induced TGF-β expression addresses the knowledge gap on the biochemical response of cells in response to external forces.

5.1.5 Cellular signalling of stem cells in therapeutic biomaterial injectates (Objective 5)

The combination of the methods and models developed, i.e. BV model, microstructural FE model and mathematical model of mechanically-induced cellular TGF-β expression, provides a computational platform to investigate and guide biomaterial and cell therapies for MI.

Linking the mathematical relationship between intracellular deformation and TGF-β expression to the parametric study on the effect of injectate stiffness on mechanics of the stem cells embedded in the injectate enables prediction of cellular signalling of therapeutically delivered cells.

The effects of the delivered biomaterial (and cells) on the heart function need to be considered in the computational platform to harness its full potential in guiding therapy development.

The platform offers a wider scope on therapeutic biomaterial and cell injections for MI and other cardiac conditions, e.g. heart failure, e.g. timing of injection after infarction and cellular expression of other biochemical factors.

Novelty: The platform offers for the first time an integrated computational method of assessing the mechanobiological effects of biomaterial and cell therapies in the heart, i.e. the mechanical support by the biomaterial injectate and the cardioprotective signalling of the delivered cells.

5.2 Limitations and recommendations

In the current study, the methods and models were developed with some assumptions for simplicity or lack of data. The present section aims at (i) highlighting the main limitations of the developed models and (ii) providing recommendations that can contribute to the amelioration of the developed models' outcomes and help to guide decisions in the design of therapies based on biomaterial injectate and stem cells for MI treatment.

5.2.1 Biventricular model development

The developed model exhibited fine details of the myocardium and the injectate morphologies. However, the truncated geometry with the boundary conditions defined at the base can be enhanced with a simplified circulatory system, including systemic arteries, systemic veins, and a pulmonary circuit, as described by Sack *et al.* (2018). Furthermore, the heart upper chambers and valves can also be incorporated.

The implementation of fibre orientation in the current subject-specific biventricular geometry used a rule-based approach consisting of a generalised mathematical formulation that was not subject-specific. An experimentally based implementation of the subject-specific fibre orientation with DT-MRI or a visualisation tool is recommended when data are available to improve the fibre structure representation in the model.

The current study did not define contact properties or interaction between different interfaces, i.e. myocardium-injectate and injectate-therapeutic cells. A continuous mesh was generated from the myocardium to the injectate resulting in fixed contact properties between these two regions. The contact definitions in the model may be revised to more realistically represent the interface mechanics. However, experimental characterisation of these interactions will be required to provide supplementary information to the description of contact properties between the different regions in the models.

The developed biventricular model used a single cardiac cycle because the focus of the research was on cellular mechanics. However, more than one cycle is recommended for future work to ensure reasonable consistency in the deformations undergone by the myocardium.

Furthermore, the mechanical model was mainly based on the solid domain of the heart. It would be more accurate to consider the fluid flow and the interaction with the myocardium in addition to the solid deformations that the cardiac tissue undergoes.

5.2.2 Micromechanics and structure of cells embedded in intramyocardial therapeutic biomaterial injectate

The described micromechanics of the therapeutically injected cells was based on assumptions that introduced limitations in the model. The main assumptions were made on the cell geometry, the membrane thickness and the cell mechanical properties.

The *in silico* representation of the embedded cells was considerably detailed due to the high resolution of the original μCT images. However, morphological details can be lost with the approach of idealised spheres to mimic the realistic behaviour of the therapeutically injected stem cells.

The membrane thickness used in the model (5 μm) was based on the limitations in the resolution of the software used to develop the cellular geometry(Simpleware). A possible way to improve is to add the membrane structure separately to the cytoplasm-nucleus geometry, exported from Simpleware (e.g. wrapping shell envelope around the cytoplasm using Abaqus/CAE (Abaqus 6.14-3, Dassault Systèmes, Providence, RI, USA).

Previous studies (Abdalrahman *et al.* 2017, Kohn *et al.* 2019) used shell elements to illustrate the considerably small thickness of the membrane compared to the nucleus and the cytoplasm. Even though the effect of mesh element type has not been investigated, it can be a source of discrepancies in the final results. A further mesh sensitivity study is recommended to quantify the effect of mesh type and decide the optimised element type.

The numerical cell seeding algorithm placed cells randomly in the entire volume of the microstructural model (sub-model). Of the 15 cells seeded, six were not used for the mechanical analysis due to their location in the tissue domain and vicinity of model boundaries and interfaces. Expanding the seeding algorithm to monitor the location of the cells can give more control over the seeding process and the number of cells available for analysis. Moreover, the number of cells used in the injectate region did not represent a realistic cell density in cell-based therapies for impaired cardiac tissue. An expansion to a larger cell number will improve the representation of *in vivo* conditions.

A further extension of the cell seeding can be directed, rather than random, cell placement to determine the impact of cell locations on their mechanics and therapeutic signalling. One can then consider cells grouped far from or dispersed and closed to the injectate-myocardium interfaces. Such an extended study can help design cell patterns within the injectate at the culture stage and when targeted spatial delivery into the heart becomes available.

The cellular components were treated as isotropic and compressible materials with Neo-Hookean strain energy density functions. The constitutive equations did not consider the active processes involved in the cell (actin polymerisation and depolymerisation). Including these dynamic cytoskeletal processes will allow assessing the medium- and long-term structural responses of cells.

5.2.3 Mechanically-driven cell signalling and the application at the organ level

The data of mechanically-induced growth factors production available in the literature are commonly from experiments performed for several hours (Zheng *et al.* 2001). Thus, the kinetics of TGF-β expression was not considered in the current model because the time scale was beyond that of biochemical reactions involved in signalling pathways (order of microseconds). A quantitatively accurate model will require information on the entire biochemical pathway of TGF-β in mesenchymal stem cells.

More growth factors and other biochemical factors can be included to extend the application of the current work, such as VEGF, known for its role in the neovascularization of the damaged tissue and responsible for new vessel formations in the infarcted tissue.

The sub-model predicted deformations of therapeutic cells embedded in the injectate beyond the strain range obtained from the experiment by Hirakata *et al.* (1997). Employing the developed relationship of the deformation-induced cellular TGF-β expression was based on the assumption that the relationship is valid beyond the experimental strain range. Further investigations or experiments are needed to confirm the validity of the linear increase in TGF-β expression in the ES-ED strain range covered in the cell deformation at the cellular scale.

The predicted variations in TGF-β expression were based on experiments with non-cardiac cells and as a function of stretch. However, several cardiac cells express and are regulated by TGF-β, which in turn is not only regulated by strain but also by stiffness and composition of the ECM and signalling ligands like angiotensin II. Therefore, multiple sources of TGF- β regulation need to be considered to improve the model further.

5.2.4 Optimisation of biomaterial and cell injection treatment

The effect of the biomaterial injectate on the ventricular function of the infarcted heart has not been considered in the current study. However, functional improvement is important for optimising biomaterial and stem cell-based therapy for MI. The current work should be extended to investigating and optimising biomaterial and cell injectates to enhance mechanically-induced signalling and ventricular functions.

Publication plan for this PhD research

Two manuscripts are in preparation for publication:

- The first manuscript on “Mechanics of a biomaterial injectate in a computational model of a rat ventricular geometry” (Sections 3.1 and 3.2).
- The second manuscript on “Cell mechanically-induced signalling in the context of a treatment for myocardial infarction” (Sections 3.3, 3.4 and 3.5).

Data availability

The data supporting this thesis can be accessed on the University of Cape Town's institutional data repository (ZivaHub) under the doi https://doi.org/10.25375/uct.17430287 from 1 March 2023 or upon request.

References

Abdalrahman T, Dubuis L, Green J, Davies N, Franz T. *Cellular mechanosensitivity to substrate stiffness decreases with increasing dissimilarity to cell stiffness*. Biomech Model Mechanobiol 2017, **16**(6): 2063-75.

Alihemmati Z, Vahidi B, Haghighipour N, Salehi M. *Computational simulation of static/cyclic cell stimulations to investigate mechanical modulation of an individual mesenchymal stem cell using confocal microscopy*. Materials Science and Engineering: C 2017, **70**: 494-504.

Anker SD, Coats AJ, Cristian G, Dragomir D, Pusineri E, Piredda M, Bettari L, Dowling R, Volterrani M, Kirwan BA, Filippatos G, Mas JL, Danchin N, Solomon SD, Lee RJ, Ahmann F, Hinson A, Sabbah HN, Mann DL. *A prospective comparison of alginate-hydrogel with standard medical therapy to determine impact on functional capacity and clinical outcomes in patients with advanced heart failure (augment-hf trial)*. Eur Heart J 2015, **36**(34): 2297-309.

Atluri P, Miller JS, Emery RJ, Hung G, Trubelja A, Cohen JE, Lloyd K, Han J, Gaffey AC, Macarthur JW. *Tissue-engineered, hydrogel-based endothelial progenitor cell therapy robustly revascularizes ischemic myocardium and preserves ventricular function*. The Journal of thoracic and cardiovascular surgery 2014, **148**(3): 1090-8.

Baaijens FP, Trickey WR, Laursen TA, Guilak F. *Large deformation finite element analysis of micropipette aspiration to determine the mechanical properties of the chondrocyte*. Ann Biomed Eng 2005, **33**(4): 494-501.

Baig MK, Mahon N, Mckenna WJ, Caforio AL, Bonow RO, Francis GS, Gheorghiade M. *The pathophysiology of advanced heart failure*. Am Heart J 1998, **135**(6 Pt 2 Su): S216-30.

Ban K, Park HJ, Kim S, Andukuri A, Cho KW, Hwang JW, Cha HJ, Kim SY, Kim WS, Jun HW, Yoon YS. *Cell therapy with embryonic stem cell-derived cardiomyocytes encapsulated in injectable nanomatrix gel enhances cell engraftment and promotes cardiac repair*. ACS Nano 2014, **8**(10): 10815-25.

Barocas VH, Moon AG, Tranquillo RT. *The fibroblast-populated collagen microsphere assay of cell traction force—part 2: Measurement of the cell traction parameter*. J Biomech Eng 1995, **117**(2): 161-70.

Bausch AR, Ziemann F, Boulbitch AA, Jacobson K, Sackmann E. *Local measurements of viscoelastic parameters of adherent cell surfaces by magnetic bead microrheometry*. Biophys J 1998, **75**(4): 2038-49.

Beltrami AP, Barlucchi L, Torella D, Baker M, Limana F, Chimenti S, Kasahara H, Rota M, Musso E, Urbanek K. *Adult cardiac stem cells are multipotent and support myocardial regeneration*. Cell 2003, **114**(6): 763-76.

Bhang SH, Gwak SJ, Lee TJ, Kim SS, Park HH, Park MH, Lee DH, Lee SH, Kim BS. *Cyclic mechanical strain promotes transforming-growth-factor-β1-mediated cardiomyogenic marker expression in bone-marrow-derived mesenchymal stem cells in vitro*. Biotechnology and applied biochemistry 2010, **55**(4): 191-7.

Birks EJ, Tansley PD, Hardy J, George RS, Bowles CT, Burke M, Banner NR, Khaghani A, Yacoub MH. *Left ventricular assist device and drug therapy for the reversal of heart failure*. N Engl J Med 2006, **355**(18): 1873-84.

Blatchley MR, Gerecht S. *Acellular implantable and injectable hydrogels for vascular regeneration*. Biomed Mater 2015, **10**(3): 034001.

Bordignon C, Carlo-Stella C, Colombo MP, De Vincentiis A, Lanata L, Lemoli RM, Locatelli F, Olivieri A, Rondelli D, Zanon P. *Cell therapy: Achievements and perspectives*. Haematologica 1999, **84**(12): 1110-49.

Burkhoff D, Klotz S, Mancini DM. *Lvad-induced reverse remodeling: Basic and clinical implications for myocardial recovery*. J Card Fail 2006, **12**(3): 227-39.

Cai L, Wang Y, Gao H, Li Y, Luo X. *A mathematical model for active contraction in healthy and failing myocytes and left ventricles*. PLoS ONE 2017, **12**(4): e0174834.

Caille N, Thoumine O, Tardy Y, Meister J-J. *Contribution of the nucleus to the mechanical properties of endothelial cells*. Journal of biomechanics 2002, **35**(2): 177-87.

Cassino TR, Drowley L, Okada M, Beckman SA, Keller B, Tobita K, Leduc PR, Huard J. *Mechanical loading of stem cells for improvement of transplantation outcome in a model of acute myocardial infarction: The role of loading history*. Tissue Eng Part A 2012, **18**(11-12): 1101-8.

Chagnon G, Rebouah M, Favier D. *Hyperelastic energy densities for soft biological tissues: A review*. Journal of Elasticity 2015, **120**(2): 129-60.

Chen J, Guo R, Zhou Q, Wang T. *Injection of composite with bone marrow-derived mesenchymal stem cells and a novel synthetic hydrogel after myocardial infarction: A protective role in left ventricle function*. Kaohsiung J Med Sci 2014a, **30**(4): 173-80.

Chen J, Guo R, Zhou Q, Wang T. *Injection of composite with bone marrow-derived mesenchymal stem cells and a novel synthetic hydrogel after myocardial infarction: A protective role in left ventricle function*. The Kaohsiung journal of medical sciences 2014b, **30**(4): 173-80.

Christman KL, Fok HH, Sievers RE, Fang Q, Lee RJ. *Fibrin glue alone and skeletal myoblasts in a fibrin scaffold preserve cardiac function after myocardial infarction*. Tissue Eng 2004a, **10**(3-4): 403-9.

Christman KL, Vardanian AJ, Fang Q, Sievers RE, Fok HH, Lee RJ. *Injectable fibrin scaffold improves cell transplant survival, reduces infarct expansion, and induces neovasculature formation in ischemic myocardium*. J Am Coll Cardiol 2004b, **44**(3): 654-60.

Connelly CM, Vogel WM, Wiegner AW, Osmers EL, Bing OH, Kloner RA, Dunn-Lanchantin DM, Franzblau C, Apstein CS. *Effects of reperfusion after coronary artery occlusion on post-infarction scar tissue*. Circ Res 1985, **57**(4): 562-77.

Costa KD, Holmes JW, Mcculloch AD. *Modelling cardiac mechanical properties in three dimensions*. Philosophical Transactions of the Royal Society of London A: Mathematical, Physical and Engineering Sciences 2001, **359**(1783): 1233-50.

Costa KD, Takayama Y, Mcculloch AD, Covell JW. *Laminar fiber architecture and three-dimensional systolic mechanics in canine ventricular myocardium*. Am J Physiol 1999, **276**(2): H595-607.

Darling E, Zauscher S, Guilak F. *Viscoelastic properties of zonal articular chondrocytes measured by atomic force microscopy*. Osteoarthritis and cartilage 2006, **14**(6): 571-9.

Davies N, Goetsch K, Ngoepe M, Franz T, Lecour S. *Delivery modes for cardiac stem cell therapy* Stem cells and cardiac regeneration, Springer, 2016: 165-90.

Di Franco S, Amarelli C, Montalto A, Loforte A, Musumeci F. *Biomaterials and heart recovery: Cardiac repair, regeneration and healing in the mcs era: A state of the "heart"*. Journal of thoracic disease 2018, **10**(Suppl 20): S2346.

Dieudonné J-M. *The left ventricle as confocal prolate spheroids*. bulletin of mathematical biophysics 1969, **31**(3): 433-9.

Dobner S, Bezuidenhout D, Govender P, Zilla P, Davies N. *A synthetic non-degradable polyethylene glycol hydrogel retards adverse post-infarct left ventricular remodeling*. J Card Fail 2009, **15**(7): 629-36.

Dương MTN, Ach T, Alkassar M, Dittrich S, Leyendecker S. *Numerical simulation of cardiac muscles in a rat biventricular model*. 6th European Conference on Computational Mechanics (ECCM 6), 7th European Conference on Computational Fluid Dynamics (ECFD 7). UK, 2018.

Duran JM, Makarewich CA, Sharp TE, Starosta T, Zhu F, Hoffman NE, Chiba Y, Madesh M, Berretta RM, Kubo H. *Bone-derived stem cells repair the heart after myocardial infarction through transdifferentiation and paracrine signaling mechanisms*. Circulation research 2013, **113**(5): 539-52.

Eschenhagen T, Bolli R, Braun T, Field LJ, Fleischmann BK, Frisén J, Giacca M, Hare JM, Houser S, Lee RT. *Cardiomyocyte regeneration: A consensus statement*. Circulation 2017, **136**(7): 680-6.

Evans EA. *Structure and deformation properties of red blood cells: Concepts and quantitative methods*. Methods Enzymol 1989, **173**: 3-35.

Evans EA, Yeung A. *Apparent viscosity and cortical tension of blood granulocytes determined by micropipet aspiration*. Biophys J 1989, **56**(1): 151-60.

Fan C, Shi J, Zhuang Y, Zhang L, Huang L, Yang W, Chen B, Chen Y, Xiao Z, Shen H, Zhao Y, Dai J. *Myocardial-infarction-responsive smart hydrogels targeting matrix metalloproteinase for on-demand growth factor delivery*. Adv Mater 2019, **31**(40): e1902900.

Federico S, Grillo A, Giaquinta G, Herzog W. *Convex fung-type potentials for biological tissues*. Meccanica 2008, **43**(3): 279-88.

Fernández-Avilés F, Sanz-Ruiz R, Climent AM, Badimon L, Bolli R, Charron D, Fuster V, Janssens S, Kastrup J, Kim H-S. *Global position paper on cardiovascular regenerative medicine*. European Heart Journal 2017, **38**(33): 2532-46.

Finegold JA, Asaria P, Francis DP. *Mortality from ischaemic heart disease by country, region, and age: Statistics from world health organisation and united nations*. Int J Cardiol 2013, **168**(2): 934-45.

Fomovsky GM, Holmes JW. *Evolution of scar structure, mechanics, and ventricular function after myocardial infarction in the rat*. Am J Physiol Heart Circ Physiol 2010, **298**(1): H221-8.

Gao LR, Chen Y, Zhang NK, Yang XL, Liu HL, Wang ZG, Yan XY, Wang Y, Zhu ZM, Li TC. *Intracoronary infusion of wharton's jelly-derived mesenchymal stem cells in acute myocardial infarction: Double-blind, randomized controlled trial*. BMC medicine 2015, **13**(1): 162.

Gasperini L, Mano JF, Reis RL. *Natural polymers for the microencapsulation of cells*. J R Soc Interface 2014, **11**(100): 20140817.

Gladilin E, Micoulet A, Hosseini B, Rohr K, Spatz J, Eils R. *3d finite element analysis of uniaxial cell stretching: From image to insight*. Phys Biol 2007, **4**(2): 104-13.

Guccione J, Mcculloch A. *Mechanics of active contraction in cardiac muscle: Part i—constitutive relations for fiber stress that describe deactivation*. Journal of Biomechanical Engineering 1993, **115**(1): 72-81.

Guccione J, Waldman L, Mcculloch A. *Mechanics of active contraction in cardiac muscle: Part ii—cylindrical models of the systolic left ventricle*. Journal of Biomechanical Engineering 1993, **115**(1): 82-90.

Guo HD, Wang HJ, Tan YZ, Wu JH. *Transplantation of marrow-derived cardiac stem cells carried in fibrin improves cardiac function after myocardial infarction*. Tissue Eng Part A 2011, **17**(1-2): 45-58.

Hare JM, Fishman JE, Gerstenblith G, Velazquez DLD, Zambrano JP, Suncion VY, Tracy M, Ghersin E, Johnston PV, Brinker JA. *Comparison of allogeneic vs autologous bone marrow–derived mesenchymal stem cells delivered by transendocardial injection in patients with ischemic cardiomyopathy: The poseidon randomized trial*. JAMA 2012, **308**(22): 2369-79.

Hare JM, Traverse JH, Henry TD, Dib N, Strumpf RK, Schulman SP, Gerstenblith G, Demaria AN, Denktas AE, Gammon RS, Hermiller JB, Jr., Reisman MA, Schaer GL, Sherman W. *A randomized, double-blind, placebo-controlled, dose-escalation study of intravenous adult human mesenchymal stem cells (prochymal) after acute myocardial infarction*. J Am Coll Cardiol 2009, **54**(24): 2277-86.

Hirakata M, Kaname S, Chung UG, Joki N, Hori Y, Noda M, Takuwa Y, Okazaki T, Fujita T, Katoh T, Kurokawa K. *Tyrosine kinase dependent expression of tgf-beta induced by stretch in mesangial cells*. Kidney Int 1997, **51**(4): 1028-36.

Hochmuth RM. *Measuring the mechanical properties of individual human blood cells*. J Biomech Eng 1993, **115**(4B): 515-9.

Hoeeg C, Dolatshahi-Pirouz A, Follin B. *Injectable hydrogels for improving cardiac cell therapy—in vivo evidence and translational challenges*. Gels 2021, **7**(1): 7.

Holmes JW, Borg TK, Covell JW. *Structure and mechanics of healing myocardial infarcts*. Annu Rev Biomed Eng 2005, **7**: 223-53.

Holmes JW, Nunez JA, Covell JW. *Functional implications of myocardial scar structure*. Am J Physiol 1997, **272**(5 Pt 2): H2123-30.

Holzapfel GA, Ogden RW. *Constitutive modelling of passive myocardium: A structurally based framework for material characterization*. Philos Trans A Math Phys Eng Sci 2009, **367**(1902): 3445-75.

Humphrey JD. *Continuum biomechanics of soft biological tissues*. Proceedings of the Royal Society of London Series A: Mathematical, Physical and Engineering Sciences 2003, **459**(2029): 3-46.

Humphrey JD, Yin FC. *On constitutive relations and finite deformations of passive cardiac tissue: I. A pseudostrain-energy function*. J Biomech Eng 1987, **109**(4): 298-304.

Janz RF, Waldron RJ. *Predicted effect of chronic apical aneurysms on the passive stiffness of the human left ventricle*. Circ Res 1978, **42**(2): 255-63.

Jean RP, Chen CS, Spector AA. *Finite-element analysis of the adhesion-cytoskeleton-nucleus mechanotransduction pathway during endothelial cell rounding: Axisymmetric model*. J Biomech Eng 2005, **127**(4): 594-600.

Johnson TD, Christman KL. *Injectable hydrogel therapies and their delivery strategies for treating myocardial infarction*. Expert opinion on drug delivery 2013, **10**(1): 59-72.

Kadner K, Dobner S, Franz T, Bezuidenhout D, Sirry MS, Zilla P, Davies NH. *The beneficial effects of deferred delivery on the efficiency of hydrogel therapy post myocardial infarction*. Biomaterials 2012, **33**(7): 2060-6.

Karcher H, Lammerding J, Huang H, Lee RT, Kamm RD, Kaazempur-Mofrad MR. *A three-dimensional viscoelastic model for cell deformation with experimental verification*. Biophys J 2003, **85**(5): 3336-49.

Ke X, Li M, Wang X, Liang J, Wang X, Wu S, Long M, Hu C. *An injectable chitosan/dextran/β-glycerophosphate hydrogel as cell delivery carrier for therapy of myocardial infarction*. Carbohydrate polymers 2020, **229**: 115516.

Kichula ET, Wang H, Dorsey SM, Szczesny SE, Elliott DM, Burdick JA, Wenk JF. *Experimental and computational investigation of altered mechanical properties in myocardium after hydrogel injection*. Ann Biomed Eng 2014, **42**(7): 1546-56.

Kikuchi K, Poss KD. *Cardiac regenerative capacity and mechanisms*. Annual review of cell and developmental biology 2012, **28**: 719.

Kim S, Healy KE. *Synthesis and characterization of injectable poly(n-isopropylacrylamide-co-acrylic acid) hydrogels with proteolytically degradable cross-links*. Biomacromolecules 2003, **4**(5): 1214-23.

Kocher AA, Schuster MD, Szabolcs MJ, Takuma S, Burkhoff D, Wang J, Homma S, Edwards NM, Itescu S. *Neovascularization of ischemic myocardium by human bone-marrow-derived angioblasts prevents cardiomyocyte apoptosis, reduces remodeling and improves cardiac function*. Nat Med 2001, **7**(4): 430-6.

Kofidis T, De Bruin JL, Hoyt G, Lebl DR, Tanaka M, Yamane T, Chang CP, Robbins RC. *Injectable bioartificial myocardial tissue for large-scale intramural cell transfer and functional recovery of injured heart muscle*. J Thorac Cardiovasc Surg 2004, **128**(4): 571-8.

Kofidis T, Lebl DR, Martinez EC, Hoyt G, Tanaka M, Robbins RC. *Novel injectable bioartificial tissue facilitates targeted, less invasive, large-scale tissue restoration on the beating heart after myocardial injury*. Circulation 2005, **112**(9 Suppl): I173-7.

Kohn JC, Abdalrahman T, Sack KL, Reinhart-King CA, Franz T. *Endothelial cells on an aged subendothelial matrix display heterogeneous strain profiles in silico*. Biomech Model Mechanobiol 2018, **17**(5): 1405-14.

Kohn JC, Abdalrahman T, Sack KL, Reinhart-King CA, Franz T. *Cell focal adhesion clustering leads to decreased and homogenized basal strains*. Int J Numer Method Biomed Eng 2019, **35**(12): e3260.

Kortsmit J, Davies NH, Miller R, Macadangdang JR, Zilla P, Franz T. *The effect of hydrogel injection on cardiac function and myocardial mechanics in a computational post-infarction model*. Comput Methods Biomech Biomed Engin 2013a, **16**(11): 1185-95.

Kortsmit J, Davies NH, Miller R, Zilla P, Franz T. *Computational predictions of improved of wall mechanics and function of the infarcted left ventricle at early and late remodelling stages: Comparison of layered and bulk hydrogel injectates*. Advances in Biomechanics and Applications 2013b, **1**(1): 41-55.

Krupnick AS, Kreisel D, Engels FH, Szeto WY, Plappert T, Popma SH, Flake AW, Rosengard BR. *A novel small animal model of left ventricular tissue engineering*. J Heart Lung Transplant 2002, **21**(2): 233-43.

Lee RJ, Hinson A, Bauernschmitt R, Matschke K, Fang Q, Mann DL, Dowling R, Schiller N, Sabbah HN. *The feasibility and safety of algisyl-lvr™ as a method of left ventricular augmentation in patients with dilated cardiomyopathy: Initial first in man clinical results*. International journal of cardiology 2015, **199**: 18-24.

Leor J, Tuvia S, Guetta V, Manczur F, Castel D, Willenz U, Petnehazy O, Landa N, Feinberg MS, Konen E, Goitein O, Tsur-Gang O, Shaul M, Klapper L, Cohen S. *Intracoronary injection of in situ forming alginate hydrogel reverses left ventricular remodeling after myocardial infarction in swine*. J Am Coll Cardiol 2009, **54**(11): 1014-23.

Lin YD, Yeh ML, Yang YJ, Tsai DC, Chu TY, Shih YY, Chang MY, Liu YW, Tang AC, Chen TY, Luo CY, Chang KC, Chen JH, Wu HL, Hung TK, Hsieh PC. *Intramyocardial peptide nanofiber injection improves postinfarction ventricular remodeling and efficacy of bone marrow cell therapy in pigs*. Circulation 2010, **122**(11 Suppl): S132-41.

Liu Z, Wang H, Wang Y, Lin Q, Yao A, Cao F, Li D, Zhou J, Duan C, Du Z, Wang Y, Wang C. *The influence of chitosan hydrogel on stem cell engraftment, survival and homing in the ischemic myocardial microenvironment*. Biomaterials 2012, **33**(11): 3093-106.

Lu W-N, Lü S-H, Wang H-B, Li D-X, Duan C-M, Liu Z-Q, Hao T, He W-J, Xu B, Fu Q. *Functional improvement of infarcted heart by co-injection of embryonic stem cells with temperature-responsive chitosan hydrogel*. Tissue Engineering Part A 2008, **15**(6): 1437-47.

Mann DL, Lee RJ, Coats AJ, Neagoe G, Dragomir D, Pusineri E, Piredda M, Bettari L, Kirwan BA, Dowling R, Volterrani M, Solomon SD, Sabbah HN, Hinson A, Anker SD. *One-year follow-up results from augment-hf: A multicentre randomized controlled clinical trial of the efficacy of left ventricular augmentation with algisyl in the treatment of heart failure*. Eur J Heart Fail 2016, **18**(3): 314-25.

Masschaele BC, Cnudde V, Dierick M, Jacobs P, Van Hoorebeke L, Vlassenbroeck J. *Ugct: New x-ray radiography and tomography facility*. Nuclear Instruments and Methods in Physics Research Section A: Accelerators, Spectrometers, Detectors and Associated Equipment 2007, **580**(1): 266-9.

Mendis S, Puska P, Norrving B. Global atlas on cardiovascular disease prevention and control, World Health Organization, 2011.

Miller R, Davies NH, Kortsmit J, Zilla P, Franz T. *Outcomes of myocardial infarction hydrogel injection therapy in the human left ventricle dependent on injectate distribution*. Int J Numer Method Biomed Eng 2013, **29**(8): 870-84.

Mininni S, Diricatti G, Vono MC, Giglioli C, Margheri M, Olivo G, Gensini G, Galanti G. *Noninvasive evaluation of right ventricle systolic pressure during dynamic exercise by saline-enhanced doppler echocardiography in progressive systemic sclerosis*. Angiology 1996, **47**(5): 467-74.

Mitchison J, Swann M. *The mechanical properties of the cell surface*. J Exp Biol 1954, **31**(3): 443-60.

Mousaei Ghasroldasht M, Seok J, Park H-S, Liakath Ali FB, Al-Hendy A. *Stem cell therapy: From idea to clinical practice*. International Journal of Molecular Sciences 2022, **23**(5): 2850.

Nguyen PK, Rhee JW, Wu JC. *Adult stem cell therapy and heart failure, 2000 to 2016: A systematic review*. JAMA Cardiol 2016, **1**(7): 831-41.

Nishikawa S-I, Goldstein RA, Nierras CR. *The promise of human induced pluripotent stem cells for research and therapy*. Nature reviews Molecular cell biology 2008, **9**(9): 725-9.

Omens JH. *Stress and strain as regulators of myocardial growth*. Prog Biophys Mol Biol 1998, **69**(2-3): 559-72.

Omens JH, Mackenna DA, Mcculloch AD. *Measurement of strain and analysis of stress in resting rat left ventricular myocardium*. J Biomech 1993, **26**(6): 665-76.

Opie LH, Mayosi BM. *Cardiovascular disease in sub-saharan africa*. Circulation 2005, **112**(23): 3536-40.

Pacher P, Mabley JG, Liaudet L, Evgenov OV, Marton A, Hasko G, Kollai M, Szabo C. *Left ventricular pressure-volume relationship in a rat model of advanced aging-associated heart failure*. Am J Physiol Heart Circ Physiol 2004, **287**(5): H2132-7.

Pinto JG, Fung YC. *Mechanical properties of the heart muscle in the passive state*. J Biomech 1973, **6**(6): 597-616.

Pittenger MF, Mackay AM, Beck SC, Jaiswal RK, Douglas R, Mosca JD, Moorman MA, Simonetti DW, Craig S, Marshak DR. *Multilineage potential of adult human mesenchymal stem cells*. Science 1999, **284**(5411): 143-7.

Plotkin M, Vaibavi SR, Rufaihah AJ, Nithya V, Wang J, Shachaf Y, Kofidis T, Seliktar D. *The effect of matrix stiffness of injectable hydrogels on the preservation of cardiac function after a heart attack*. Biomaterials 2014, **35**(5): 1429-38.

Rashid FN, Clayton ZE, Ogawa M, Perdomo J, Hume RD, Kizana E, Chong JJH. *Platelet derived growth factor-a (pdgf-a) gene transfer modulates scar composition and improves left ventricular function after myocardial infarction*. Int J Cardiol 2021, **341**: 24-30.

Ravichandran R, Venugopal JR, Sundarrajan S, Mukherjee S, Ramakrishna S. *Poly (glycerol sebacate)/gelatin core/shell fibrous structure for regeneration of myocardial infarction*. Tissue Engineering Part A 2011, **17**(9-10): 1363-73.

Ravichandran R, Venugopal JR, Sundarrajan S, Mukherjee S, Ramakrishna S. *Minimally invasive cell-seeded biomaterial systems for injectable/epicardial implantation in ischemic heart disease*. Int J Nanomedicine 2012, **7**: 5969-94.

Reichek N, Devereux RB. *Reliable estimation of peak left ventricular systolic pressure by m-mode echographic-determined end-diastolic relative wall thickness: Identification of severe valvular aortic stenosis in adult patients*. Am Heart J 1982, **103**(2): 202-3.

Rizzi SC, Ehrbar M, Halstenberg S, Raeber GP, Schmoekel HG, Hagenmüller H, Müller R, Weber FE, Hubbell JA. *Recombinant protein-co-peg networks as cell-adhesive and proteolytically degradable hydrogel matrixes. Part ii: Biofunctional characteristics*. Biomacromolecules 2006, **7**(11): 3019-29.

Robinton DA, Daley GQ. *The promise of induced pluripotent stem cells in research and therapy*. Nature 2012, **481**(7381): 295-305.

Rodriguez ML, Mcgarry PJ, Sniadecki NJ. *Review on cell mechanics: Experimental and modeling approaches*. Applied Mechanics Reviews 2013, **65**(6).

Ryu JH, Kim I-K, Cho S-W, Cho M-C, Hwang K-K, Piao H, Piao S, Lim SH, Hong YS, Choi CY. *Implantation of bone marrow mononuclear cells using injectable fibrin matrix enhances neovascularization in infarcted myocardium*. Biomaterials 2005, **26**(3): 319-26.

Sabbah HN, Wang M, Gupta RC, Rastogi S, Ilsar I, Sabbah MS, Kohli S, Helgerson S, Lee RJ. *Augmentation of left ventricular wall thickness with alginate hydrogel implants improves left ventricular function and prevents progressive remodeling in dogs with chronic heart failure*. JACC Heart Fail 2013, **1**(3): 252-8.

Sack KL, Aliotta E, Ennis DB, Choy JS, Kassab GS, Guccione JM, Franz T. *Construction and validation of subject-specific biventricular finite-element models of healthy and failing swine hearts from high-resolution dt-mri*. Front Physiol 2018, **9**(539): 539.

Sack KL, Baillargeon B, Acevedo-Bolton G, Genet M, Rebelo N, Kuhl E, Klein L, Weiselthaler G, Burkhoff D, Franz T. *Partial lvad restores ventricular outputs and normalizes lv but not rv stress distributions in the acutely failing heart in silico*. International journal of artificial organs 2016, **39**(8): 421.

Sacks MS. *Biaxial mechanical evaluation of planar biological materials*. Journal of elasticity and the physical science of solids 2000, **61**(1-3): 199.

Saeed M, Sharabani-Yosef O, Weihs D, Gefen A. *A phase-contrast microscopy-based method for modeling the mechanical behavior of mesenchymal stem cells*. Comput Methods Biomech Biomed Engin 2016, **19**(13): 1359-62.

Saludas L, Pascual-Gil S, Prosper F, Garbayo E, Blanco-Prieto M. *Hydrogel based approaches for cardiac tissue engineering*. Int J Pharm 2017, **523**(2): 454-75.

Seko Y, Seko Y, Takahashi N, Shibuya M, Yazaki Y. *Pulsatile stretch stimulates vascular endothelial growth factor (vegf) secretion by cultured rat cardiac myocytes*. Biochem Biophys Res Commun 1999, **254**(2): 462-5.

Semler EJ, Ranucci CS, Moghe PV. *Mechanochemical manipulation of hepatocyte aggregation can selectively induce or repress liver-specific function*. Biotechnology and bioengineering 2000, **69**(4): 359-69.

Sepantafar M, Maheronnaghsh R, Mohammadi H, Rajabi-Zeleti S, Annabi N, Aghdami N, Baharvand H. *Stem cells and injectable hydrogels: Synergistic therapeutics in myocardial repair*. Biotechnol Adv 2016, **34**(4): 362-79.

Shradhanjali A, Riehl BD, Lee JS, Ha L, Lim JY. *Enhanced cardiomyogenic induction of mouse pluripotent cells by cyclic mechanical stretch*. Biochem Biophys Res Commun 2017, **488**(4): 590-5.

Shudo Y, Miyagawa S, Ohkura H, Fukushima S, Saito A, Shiozaki M, Kawaguchi N, Matsuura N, Shimizu T, Okano T. *Addition of mesenchymal stem cells enhances the therapeutic effects of skeletal myoblast cell-sheet transplantation in a rat ischemic cardiomyopathy model*. Tissue Engineering Part A 2013, **20**(3-4): 728-39.

Silveira-Filho LM, Coyan GN, Adamo A, Luketich SK, Menallo G, D'amore A, Wagner WR. *Can a biohybrid patch salvage ventricular function at a late time point in the post-infarction remodeling process?* Basic to Translational Science 2021, **6**(5): 447-63.

Singelyn JM, Dequach JA, Seif-Naraghi SB, Littlefield RB, Schup-Magoffin PJ, Christman KL. *Naturally derived myocardial matrix as an injectable scaffold for cardiac tissue engineering*. Biomaterials 2009, **30**(29): 5409-16.

Singelyn JM, Sundaramurthy P, Johnson TD, Schup-Magoffin PJ, Hu DP, Faulk DM, Wang J, Mayle KM, Bartels K, Salvatore M, Kinsey AM, Demaria AN, Dib N, Christman KL. *Catheter-deliverable hydrogel derived from decellularized ventricular extracellular matrix increases endogenous cardiomyocytes and preserves cardiac function post-myocardial infarction*. J Am Coll Cardiol 2012, **59**(8): 751-63.

Sirry MS. *Computational biomechanics of acute myocardial infarction and its treatments*. Human Biology, Univerity of Cape Town, 2015, **PhD**: 145.

Sirry MS, Butler JR, Patnaik SS, Brazile B, Bertucci R, Claude A, Mclaughlin R, Davies NH, Liao J, Franz T. *Characterisation of the mechanical properties of infarcted myocardium in the rat under biaxial tension and uniaxial compression*. J Mech Behav Biomed Mater 2016, **63**: 252-64.

Sirry MS, Davies NH, Kadner K, Dubuis L, Saleh MG, Meintjes EM, Spottiswoode BS, Zilla P, Franz T. *Micro-structurally detailed model of a therapeutic hydrogel injectate in a rat biventricular cardiac geometry for computational simulations*. Comput Methods Biomech Biomed Engin 2015, **18**(3): 325-31.

Slomka N, Gefen A. *Finite element modeling of cellular mechanics experiments*. in Gefen A (Ed. Cellular and biomolecular mechanics and mechanobiology. Berlin, Heidelberg, Springer Berlin Heidelberg, 2010, 10.1007/8415_2010_31: 331-44.

Slomka N, Or-Tzadikario S, Sassun D, Gefen A. *Membrane-stretch-induced cell death in deep tissue injury: Computer model studies*. Cell Mol Bioeng 2009, **2**(1): 118-32.

Sommer G, Schriefl AJ, Andra M, Sacherer M, Viertler C, Wolinski H, Holzapfel GA. *Biomechanical properties and microstructure of human ventricular myocardium*. Acta Biomater 2015, **24**: 172-92.

Stankus JJ, Guan J, Wagner WR. *Fabrication of biodegradable elastomeric scaffolds with sub-micron morphologies*. J Biomed Mater Res A 2004, **70**(4): 603-14.

Stokke BT, Draget KI, Smidsrød O, Yuguchi Y, Urakawa H, Kajiwara K. *Small-angle x-ray scattering and rheological characterization of alginate gels. 1. Ca− alginate gels*. Macromolecules 2000, **33**(5): 1853-63.

Strauer BE, Brehm M, Zeus T. *Repair of infarcted myocardium by autologous intracoronary mononuclear bone marrow cell transplantation in humans*. ACC Current Journal Review 2003, **1**(12): 44.

Strauer BE, Steinhoff G. *10 years of intracoronary and intramyocardial bone marrow stem cell therapy of the heart: From the methodological origin to clinical practice*. J Am Coll Cardiol 2011, **58**(11): 1095-104.

Sun K, Stander N, Jhun CS, Zhang Z, Suzuki T, Wang GY, Saeed M, Wallace AW, Tseng EE, Baker AJ, Saloner D, Einstein DR, Ratcliffe MB, Guccione JM. *A computationally efficient formal optimization of regional myocardial contractility in a sheep with left ventricular aneurysm*. J Biomech Eng 2009, **131**(11): 111001.

Takayama Y, Costa KD, Covell JW. *Contribution of laminar myofiber architecture to load-dependent changes in mechanics of lv myocardium*. Am J Physiol Heart Circ Physiol 2002, **282**(4): H1510-20.

Tee SY, Fu J, Chen CS, Janmey PA. *Cell shape and substrate rigidity both regulate cell stiffness*. Biophys J 2011, **100**(5): L25-7.

Thavapalachandran S, Le TYL, Romanazzo S, Rashid FN, Ogawa M, Kilian KA, Brown P, Pouliopoulos J, Barry AM, Fahmy P. *Pluripotent stem cell-derived mesenchymal*

stromal cells improve cardiac function and vascularity after myocardial infarction. Cytotherapy 2021, **23**(12): 1074-84.

Tian Y, Gawlak G, O'donnell JJ, 3rd, Birukova AA, Birukov KG. *Activation of vascular endothelial growth factor (vegf) receptor 2 mediates endothelial permeability caused by cyclic stretch*. J Biol Chem 2016, **291**(19): 10032-45.

Toeg HD, Tiwari-Pandey R, Seymour R, Ahmadi A, Crowe S, Vulesevic B, Suuronen EJ, Ruel M. *Injectable small intestine submucosal extracellular matrix in an acute myocardial infarction model*. Ann Thorac Surg 2013, **96**(5): 1686-94; discussion 94.

Toh WS, Loh XJ. *Advances in hydrogel delivery systems for tissue regeneration*. Mater Sci Eng C Mater Biol Appl 2014, **45**: 690-7.

Tomita S, Li RK, Weisel RD, Mickle DA, Kim EJ, Sakai T, Jia ZQ. *Autologous transplantation of bone marrow cells improves damaged heart function*. Circulation 1999, **100**(19 Suppl): II247-56.

Traverse JH, Henry TD, Dib N, Patel AN, Pepine C, Schaer GL, Dequach JA, Kinsey AM, Chamberlin P, Christman KL. *First-in-man study of a cardiac extracellular matrix hydrogel in early and late myocardial infarction patients*. JACC Basic Transl Sci 2019, **4**(6): 659-69.

Trickey WR, Baaijens FP, Laursen TA, Alexopoulos LG, Guilak F. *Determination of the poisson's ratio of the cell: Recovery properties of chondrocytes after release from complete micropipette aspiration*. J Biomech 2006, **39**(1): 78-87.

Tyberg JV, Forrester JS, Wyatt HL, Goldner SJ, Parmley WW, Swan HJ. *An analysis of segmental ischemic dysfunction utilizing the pressure-length loop*. Circulation 1974, **49**(4): 748-54.

Urech L, Bittermann AG, Hubbell JA, Hall H. *Mechanical properties, proteolytic degradability and biological modifications affect angiogenic process extension into native and modified fibrin matrices in vitro*. Biomaterials 2005, **26**(12): 1369-79.

Villarreal FJ, Lew WY, Waldman LK, Covell JW. *Transmural myocardial deformation in the ischemic canine left ventricle*. Circ Res 1991, **68**(2): 368-81.

Vlassenbroeck J, Dierick M, Masschaele B, Cnudde V, Van Hoorebeke L, Jacobs P. *Software tools for quantification of x-ray microtomography at the ugct*. Nuclear Instruments and Methods in Physics Research Section A: Accelerators, Spectrometers, Detectors and Associated Equipment 2007, **580**(1): 442-5.

Waldman LK, Nosan D, Villarreal F, Covell JW. *Relation between transmural deformation and local myofiber direction in canine left ventricle*. Circulation research 1988, **63**(3): 550-62.

Walker JC, Ratcliffe MB, Zhang P, Wallace AW, Fata B, Hsu EW, Saloner D, Guccione JM. *Mri-based finite-element analysis of left ventricular aneurysm*. Am J Physiol Heart Circ Physiol 2005, **289**(2): H692-700.

Wall ST, Walker JC, Healy KE, Ratcliffe MB, Guccione JM. *Theoretical impact of the injection of material into the myocardium: A finite element model simulation*. Circulation 2006, **114**(24): 2627-35.

Wang H, Liu Z, Li D, Guo X, Kasper FK, Duan C, Zhou J, Mikos AG, Wang C. *Injectable biodegradable hydrogels for embryonic stem cell transplantation: Improved cardiac remodelling and function of myocardial infarction*. J Cell Mol Med 2012, **16**(6): 1310-20.

Wang H, Rodell CB, Lee ME, Dusaj NN, Gorman JH, 3rd, Burdick JA, Gorman RC, Wenk JF. *Computational sensitivity investigation of hydrogel injection characteristics for myocardial support*. J Biomech 2017, **64**: 231-5.

Wang H, Shi J, Wang Y, Yin Y, Wang L, Liu J, Liu Z, Duan C, Zhu P, Wang C. *Promotion of cardiac differentiation of brown adipose derived stem cells by chitosan hydrogel for repair after myocardial infarction*. Biomaterials 2014, **35**(13): 3986-98.

Wang W, Tan B, Chen J, Bao R, Zhang X, Liang S, Shang Y, Liang W, Cui Y, Fan G, Jia H, Liu W. *An injectable conductive hydrogel encapsulating plasmid DNA-enos and adscs for treating myocardial infarction*. Biomaterials 2018, **160**: 69-81.

Wenk JF, Eslami P, Zhang Z, Xu C, Kuhl E, Gorman Iii JH, Robb JD, Ratcliffe MB, Gorman RC, Guccione JM. *A novel method for quantifying the in-vivo mechanical effect of material injected into a myocardial infarction*. The Annals of Thoracic Surgery 2011, **92**(3): 935-41.

Wenk JF, Wall ST, Peterson RC, Helgerson SL, Sabbah HN, Burger M, Stander N, Ratcliffe MB, Guccione JM. *A method for automatically optimizing medical devices for treating heart failure: Designing polymeric injection patterns*. J Biomech Eng 2009, **131**(12): 121011.

Wise P, Davies NH, Sirry MS, Kortsmit J, Dubuis L, Chai CK, Baaijens FP, Franz T. *Excessive volume of hydrogel injectates may compromise the efficacy for the treatment of acute myocardial infarction*. International journal for numerical methods in biomedical engineering 2016, **32**(12): e02772.

Wollert KC, Meyer GP, Lotz J, Ringes-Lichtenberg S, Lippolt P, Breidenbach C, Fichtner S, Korte T, Hornig B, Messinger D, Arseniev L, Hertenstein B, Ganser A, Drexler H. *Intracoronary autologous bone-marrow cell transfer after myocardial infarction: The boost randomised controlled clinical trial*. Lancet 2004, **364**(9429): 141-8.

Wu Z, Cheng S, Wang S, Li W, Liu J. *Bmscs-derived exosomal microrna-150-5p attenuates myocardial infarction in mice*. International Immunopharmacology 2021, **93**: 107389.

Xu G, Wang X, Deng C, Teng X, Suuronen EJ, Shen Z, Zhong Z. *Injectable biodegradable hybrid hydrogels based on thiolated collagen and oligo (acryloyl carbonate)–poly (ethylene glycol)–oligo (acryloyl carbonate) copolymer for functional cardiac regeneration*. Acta biomaterialia 2015, **15**: 55-64.

Yamada H, Mouri N, Nobuhara S. *Three-dimensional morphometry of single endothelial cells with substrate stretching and image-based finite element modeling*. EURASIP Journal on Advances in Signal Processing 2009, **2010**(1): 616091.

Yamada S, Wirtz D, Kuo SC. *Mechanics of living cells measured by laser tracking microrheology*. Biophys J 2000, **78**(4): 1736-47.

Yin FC, Strumpf RK, Chew PH, Zeger SL. *Quantification of the mechanical properties of noncontracting canine myocardium under simultaneous biaxial loading*. J Biomech 1987, **20**(6): 577-89.

Zhang P, Zhang H, Wang H, Wei Y, Hu S. *Artificial matrix helps neonatal cardiomyocytes restore injured myocardium in rats*. Artif Organs 2006, **30**(2): 86-93.

Zhao L, Liu X, Zhang Y, Liang X, Ding Y, Xu Y, Fang Z, Zhang F. *Enhanced cell survival and paracrine effects of mesenchymal stem cells overexpressing hepatocyte growth factor promote cardioprotection in myocardial infarction*. Exp Cell Res 2016, **344**(1): 30-9.

Zheng W, Seftor EA, Meininger CJ, Hendrix MJ, Tomanek RJ. *Mechanisms of coronary angiogenesis in response to stretch: Role of vegf and tgf-beta*. Am J Physiol Heart Circ Physiol 2001, **280**(2): H909-17.

Appendix A Strain distribution-descriptive statistics values

ES myofibre and cross-fibre strain in biventricular model

App Table 1. Statistical values of the ES myofibre strain distribution in the healthy and infarcted myocardium

	MYOFIBRE STRAINS			
E_{INJ}	**Mean**	**Median**	**Q1**	**Q3**
4.059	-18.56	-20.37	-23.49	11.27
7.38	-18.40	-20.10	-23.29	10.98
40.59	-17.37	-18.64	-22.18	10.45
73.8	-16.86	-17.94	-21.67	10.27
405.9	-15.26	-16.11	-20.39	9.94
738	-14.63	-15.53	-20.06	9.87
4059	-12.91	-13.94	-19.28	9.78
7380	-12.40	-13.47	-19.04	9.80
40590	-11.42	-12.49	-18.57	9.93
73800	-11.04	-12.00	-18.32	9.99
405900	-10.89	-11.76	-18.59	10.42

App Table 2. Statistical values of the ES cross-fibre strain distribution in the healthy and infarcted myocardium

	CROSS-FIBRE STRAINS			
E_{INJ}	**Mean**	**Median**	**Q1**	**Q3**
4.059	5.01	6.47	-0.62	12.26
7.38	4.70	6.06	-0.88	11.80
40.59	4.08	5.53	-1.72	11.04
73.8	4.18	5.46	-1.67	11.17
405.9	5.00	5.73	-1.05	12.21
738	5.21	5.79	-0.86	12.51
4059	5.40	5.58	-0.84	12.96
7380	5.37	5.47	-0.91	13.01
40590	5.03	5.00	-1.33	12.82
73800	5.01	4.97	-1.41	12.86
405900	4.57	4.58	-1.86	12.36

ED myofibre and cross-fibre strain in biventricular model

App Table 3. Statistical values of the ED myofibre strain distribution in the healthy and infarcted myocardium

	MYOFIBRE STRAIN			
E_{INJ}	**Mean**	**Median**	**Q1**	**Q3**
4.059	3.85	3.55	1.31	6.25
7.38	3.81	3.44	1.22	6.32
40.59	3.40	2.69	0.79	5.88
73.8	3.21	2.39	0.63	5.60
405.9	2.72	1.68	0.25	4.94
738	2.59	1.48	0.15	4.77
4059	2.35	1.14	-0.03	4.40
7380	2.30	1.10	-0.05	4.33
40590	2.20	1.02	-0.08	4.19
73800	2.16	1.00	-0.12	4.13
405900	2.18	1.12	-0.18	4.21

App Table 4. Statistical values of the ED cross-fibre strain distribution in the healthy and infarcted myocardium

	CROSS-FIBRE STRAINS			
E_{INJ}	**Mean**	**Median**	**Q1**	**Q3**
4.059	-7.46	-5.96	-11.00	-2.99
7.38	-7.32	-5.71	-11.00	-2.72
40.59	-6.62	-4.78	-10.02	-1.90
73.8	-6.34	-4.45	-9.60	-1.62
405.9	-5.68	-3.60	-8.64	-0.98
738	-5.53	-3.37	-8.45	-0.79
4059	-5.23	-2.95	-8.12	-0.44
7380	-5.16	-2.87	-8.06	-0.37
40590	-5.01	-2.75	-7.92	-0.25
73800	-5.00	-2.68	-7.93	-0.21
405900	-4.81	-2.89	-7.49	-0.12

ES maximum and minimum principal strain in injectate of biventricular model

App Table 5. Statistical values of the ES maximum strain distribution in the injectate in the BV model

	MAX PRINCIPAL STRAIN			
E_{INJ}	**Mean**	**Median**	**Q1**	**Q3**
4.059	38.527	38.527	30.665	49.836
7.38	35.113	35.113	27.969	45.331
40.59	21.359	21.359	16.176	27.217
73.8	16.173	16.173	12.101	20.750
405.9	6.247	6.247	4.626	8.497
738	4.397	4.397	3.174	6.151
4059	1.503	1.503	0.996	2.283
7380	1.018	1.018	0.653	1.583
40590	0.316	0.316	0.188	0.545
73800	0.194	0.194	0.114	0.351
405900	0.060	0.060	0.033	0.117

App Table 6. Statistical values of the ES minimum strain distribution in the injectate

	MIN PRINCIPAL STRAIN			
E_{INJ}	**Mean**	**Median**	**Q1**	**Q3**
4.059	-38.951	-38.951	-54.549	-28.447
7.38	-34.617	-34.617	-48.272	-25.651
40.59	-19.873	-19.873	-27.509	-14.752
73.8	-15.109	-15.109	-20.536	-11.296
405.9	-6.326	-6.326	-8.983	-4.620
738	-4.547	-4.547	-6.583	-3.232
4059	-1.555	-1.555	-2.408	-1.036
7380	-1.041	-1.041	-1.658	-0.684
40590	-0.321	-0.321	-0.556	-0.192
73800	-0.197	-0.197	-0.356	-0.116
405900	-0.062	-0.062	-0.123	-0.03

ED maximum and minimum principal strain in injectate of biventricular model

App Table 7. Statistical values of the ED maximum principal strain distribution in the injectate of the BV model

	MAX PRINCIPAL STRAIN			
E_{INJ}	Mean	Median	Q1	Q3
4.059	5.360	5.360	2.962	8.037
7.38	4.024	4.024	2.149	6.210
40.59	1.484	1.484	0.782	2.576
73.8	0.995	0.995	0.527	1.811
405.9	0.312	0.312	0.162	0.643
738	0.215	0.215	0.108	0.452
4059	0.072	0.072	0.034	0.152
7380	0.047	0.047	0.022	0.099
40590	0.011	0.011	0.005	0.024
73800	0.007	0.007	0.003	0.014
405900	0.001	0.001	0.001	0.003

App Table 8. Statistical values of the ED minimum strain distribution in the injectate

	MIN PRINCIPAL STRAIN			
E_{INJ}	**Mean**	**Median**	**Q1**	**Q3**
4.059	-5.419	-5.419	-8.615	-2.994
7.38	-3.948	-3.948	-6.524	-2.122
40.59	-1.367	-1.367	-2.495	-0.731
73.8	-0.914	-0.914	-1.698	-0.476
405.9	-0.298	-0.298	-0.600	-0.156
738	-0.207	-0.207	-0.426	-0.106
4059	-0.072	-0.072	-0.145	-0.035
7380	-0.047	-0.047	-0.094	-0.023
40590	-0.011	-0.011	-0.023	-0.005
73800	-0.007	-0.007	-0.014	-0.003
405900	-0.001	-0.001	-0.003	-0.001

Appendix B Box plots strain distribution in cells (sub-model)

Description of data presentation

From section 0 to 0, the cell's and its components (membrane, cytoplasm, and nucleus) volume-averaged end-systolic and end-diastolic maximum and minimum principal strains are reported in boxplots. Each boxplot presents the distribution of volume-averaged strains of nine cells and the mean values. These plots are repeated for each of the 11 values of the injectate elastic modulus.

Deformation in entire cell

At end-diastole, the group cell strain maximum principal strain decreased from 7.3% to 3.2%, and the minimum principal strain decreased in magnitude from -7.6% to -2.6% (App Figure 1 B) for increasing injectate stiffness.

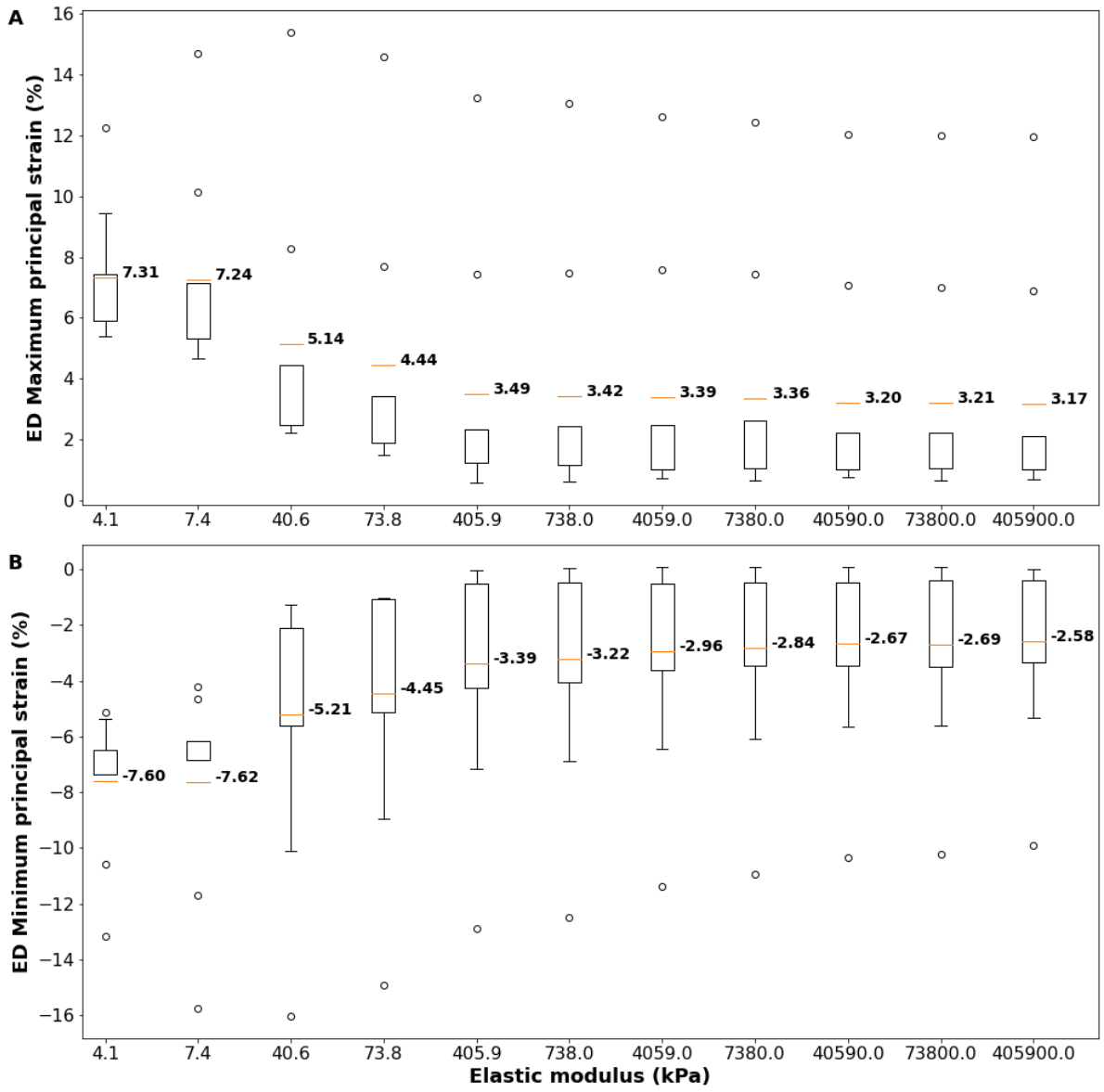

App Figure 1. End-diastolic cell deformation: Volume average maximum principal strain (A) and volume average minimum principal strain (B) in the cells for different injectate stiffnesses. Each boxplot displays the distribution of nine cells volume-averaged strain values (mean of membrane, cytoplasm, and nuclei volume averaged strain). The volume-averaged strain was calculated for each cell component. The mean was then calculated over the three cell components and the nine cells (the formula is provided in Eqn. (2.20)).

At end-systole, the group cell strain maximum principal strain decreased from 50.2% to 3.3% (App Figure 2 A), and the minimum principal strain decreased in magnitude from -40.2% to -3.7% (App Figure 2 B) from the lowest to the highest injectate stiffness.

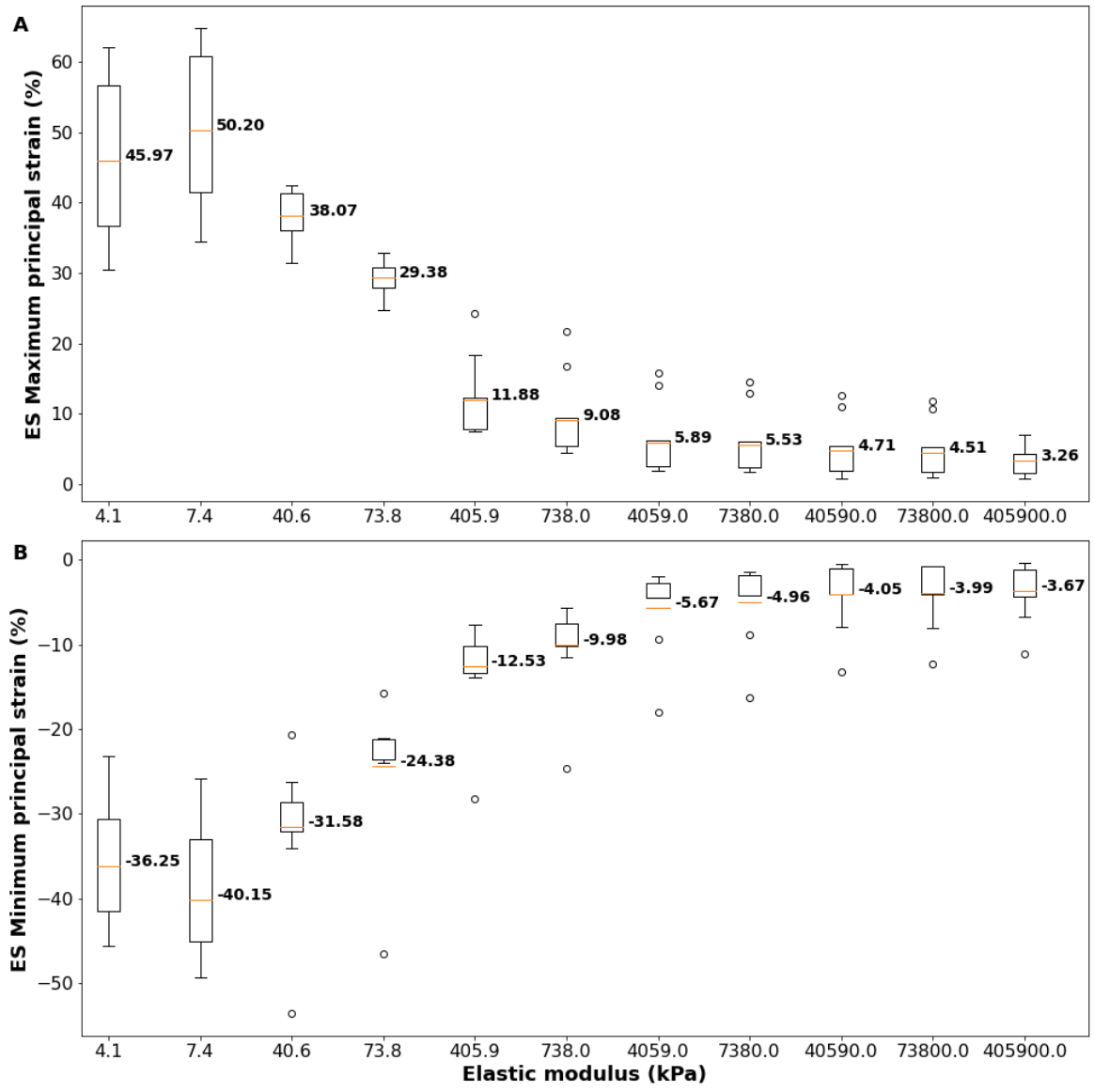

App Figure 2. End-systolic cell deformation: maximum (A) and minimum (B) principal strain in the cells for different injectate stiffnesses. Each boxplot displays the distribution of nine cells' volume-averaged strain values (mean of membrane, cytoplasm, and nuclei volume averaged strain). The volume-averaged strain was calculated for each cell component. The mean was then calculated over the three cell components and the nine cells (the formula is provided in Eqn. (2.20)).

Deformation in cytoplasm

The distribution of the volume-averaged strain in the cytoplasms is presented in boxplots with the mean of the nine cytoplasms strain displayed with an orange line. The mean end-diastole maximum principal strain value in the cytoplasms decreased from 4.3% to 2.0% for an increasing injectate stiffness (App Figure 3 A). The mean end-diastolic minimum principal strain increased from -4.6% to -1.6% for an increasing injectate stiffness (App Figure 3 B). The end-systolic maximum and minimum principal strain decreased from 30.4% to 2.0% (App Figure 4 A) and increased from -25.2% to -2.3% (App Figure 4 B), respectively.

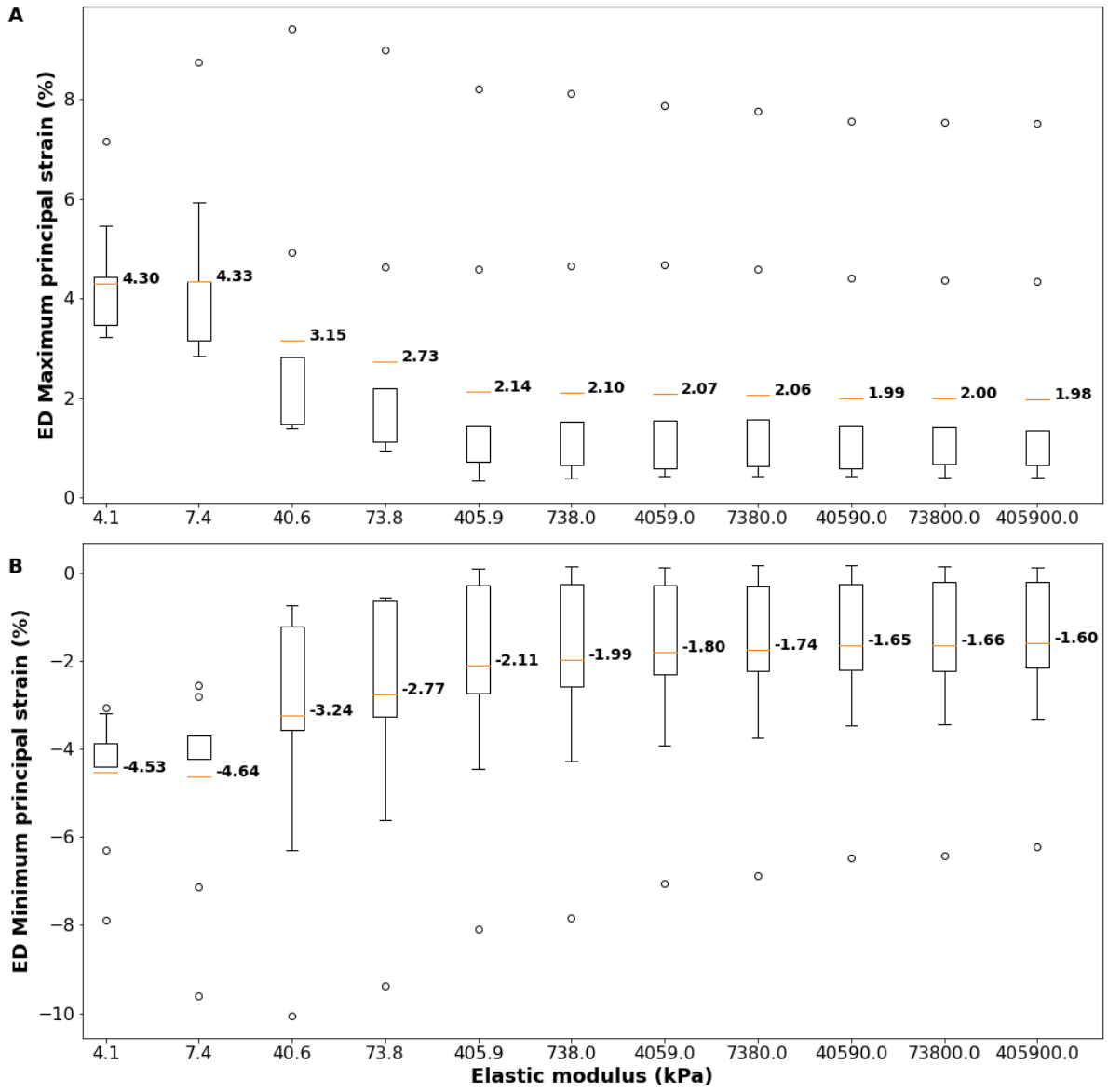

App Figure 3. End-diastolic cytoplasmic deformation: maximum (A) and minimum (B) principal strain in the cytoplasm for different injectate stiffnesses (from 4.1 kPa to 405,900.0 kPa). For each value of injectate stiffness, a boxplot is presented to display the distribution of averaged strain values from different cells (nine cytoplasms volume-averaged strain in this graph). The orange line in the box indicates the mean value overs all nine cells.

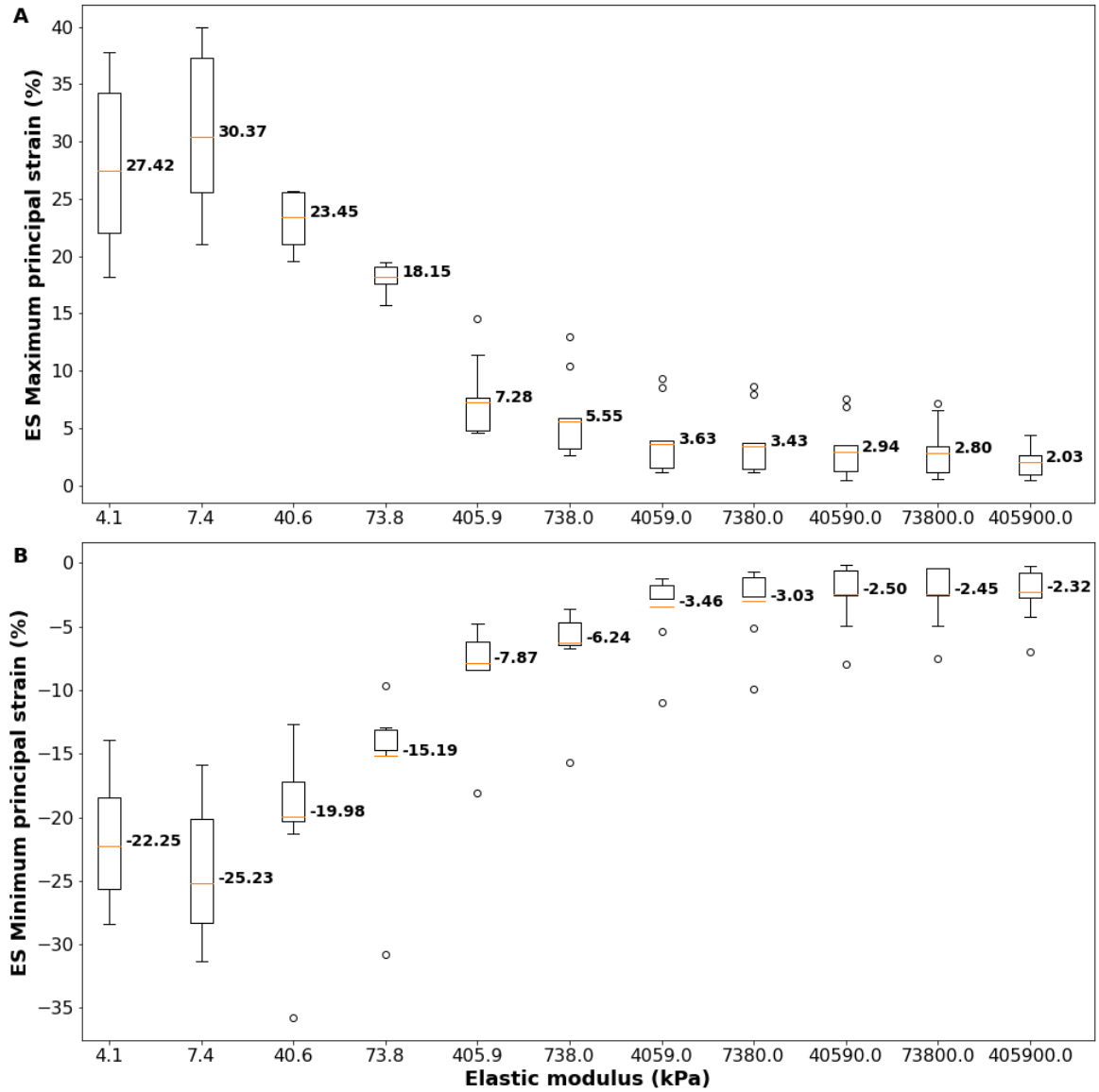

App Figure 4. End-systole cytoplasmic deformation: maximum (A) and minimum (B) principal strain in the cytoplasm for different injectate stiffnesses (from 4.1 kPa to 405,900.0 kPa). For each value of injectate stiffness, a boxplot is presented to display the distribution of averaged strain values from different cells (nine cytoplasms volume-averaged strain in this graph). The orange line in the box indicates the mean value overs all nine cells.

Deformation in cell membrane

The distribution of volume-averaged strain in all nine cells was shown in boxplots for eleven injectate stiffness values in the membranes. The variation of the mean (the mean shown with an orange line in the box) was reported. The end-diastole maximum and minimum principal strain decreased from 11.9% to 4.7% (App Figure 5 A) and increased from -11.9% to -3.6% (App Figure 5 B), respectively. The end-systole mean maximum and minimum principal strain decreased from 81.8% to 4.8% (App Figure 6 A) and increased from -59.8% to -5.2% (App Figure 6 B), respectively.

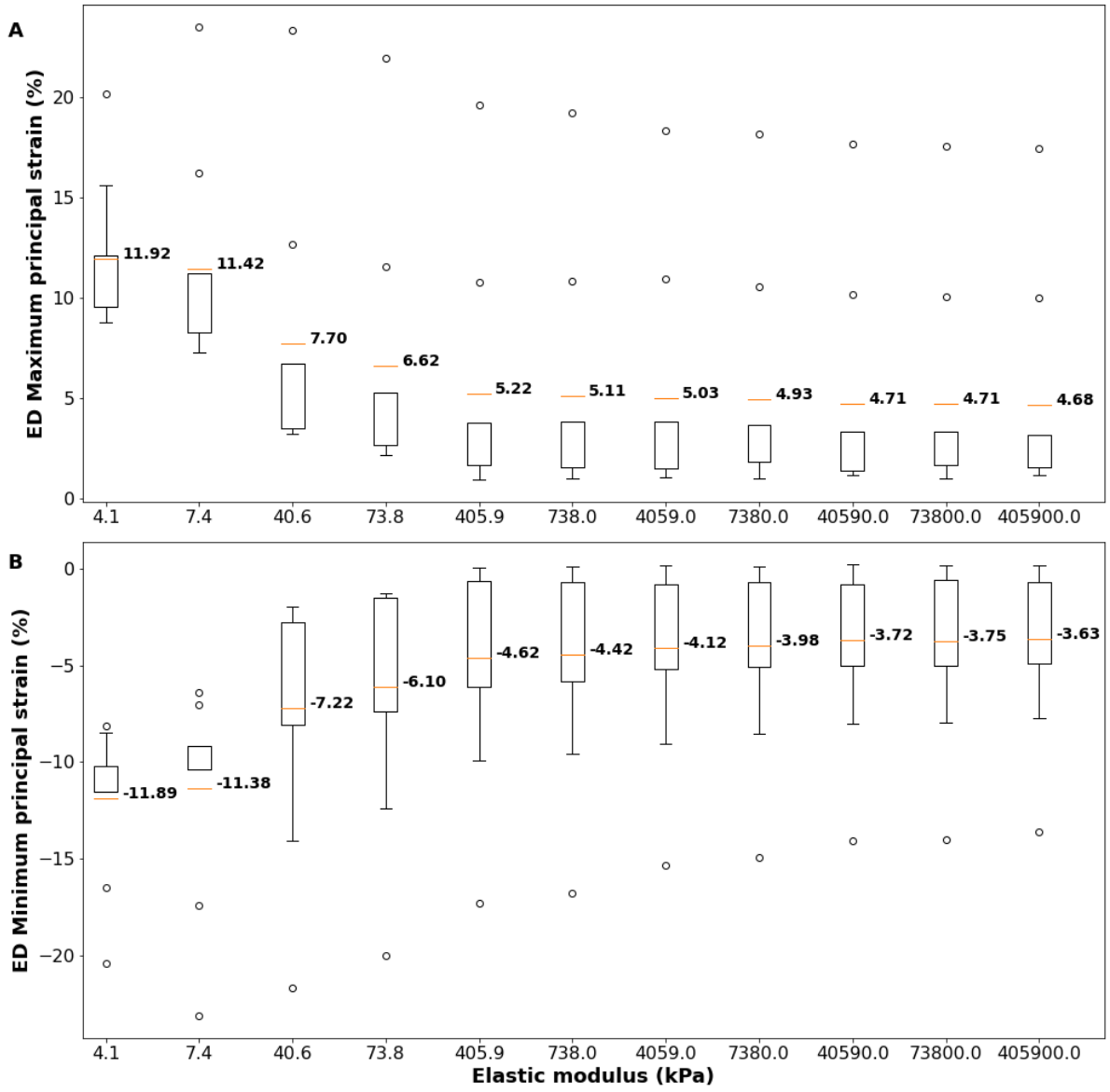

App Figure 5. End-diastolic membrane deformation: maximum (A) and minimum (B) principal strain in the cellular membrane for different injectate stiffnesses (from 4.1 kPa to 405,900.0 kPa). For each value of injectate stiffness, a boxplot is presented to display the distribution of averaged strain values from different cells (nine membranes volume-averaged strain in this graph). The orange line in the box indicates the mean value overs all nine cells.

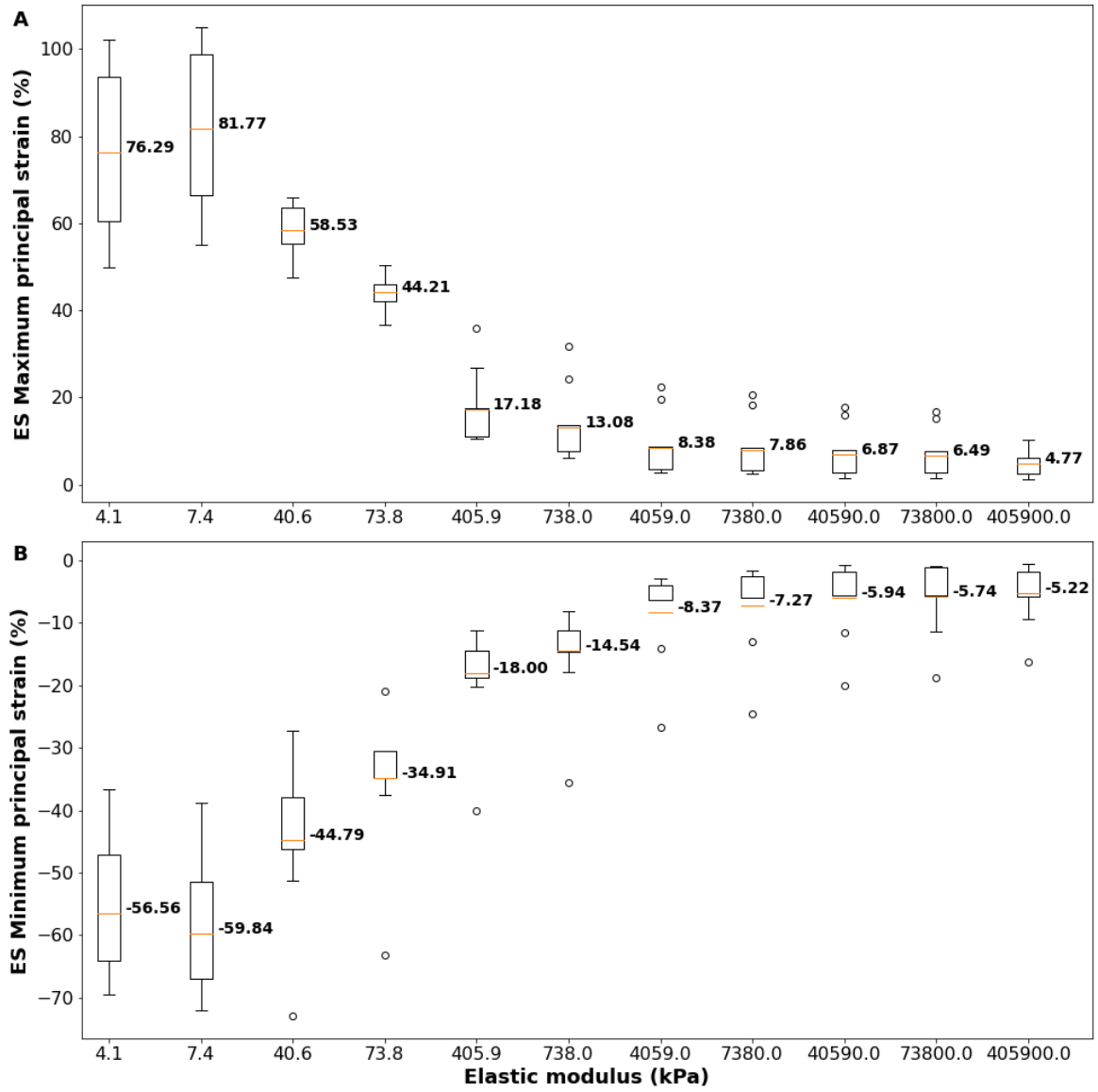

App Figure 6. End-systole membrane deformation: maximum (A) and minimum (B) principal strain in the cellular membrane for different injectate stiffnesses (from 4.1 kPa to 405,900.0 kPa). For each value of injectate stiffness, a boxplot is presented to display the distribution of averaged strain values from different cells (nine membranes volume-averaged strain in this graph). The orange line in the box indicates the mean value overs all nine cells.

Deformation in nucleus

The distribution of volume-averaged strain in nine cells was shown in boxplots for eleven injectate stiffness values in the nucleus. The maximum and minimum principal strain values decreased from 5.9% to 2.8% (App Figure 7 A) and increased from -6.8% to -2.5%, respectively (App Figure 7 B). The end-systolic mean value of the maximum and minimum principal strain in nuclei decreased from 38.5% to 3.0% (App Figure 8 A) and increased from -35.4% to -3.5% (App Figure 8 B), respectively.

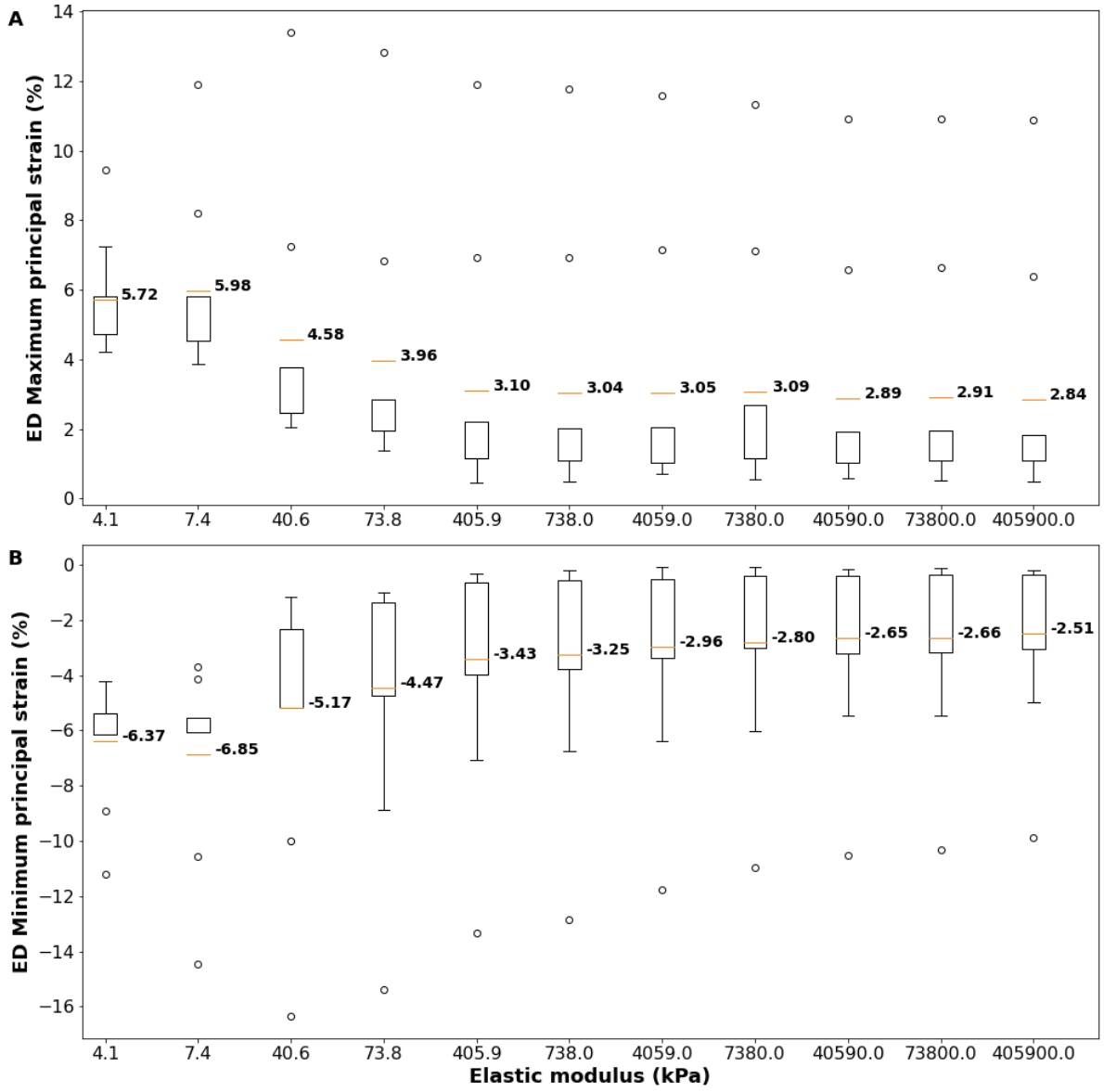

App Figure 7. End-diastolic nuclear deformation: maximum (A) and minimum (B) principal strain in the cell nucleus for different injectate stiffnesses (from 4..1 kPa to 405,900.0 kPa). For each value of injectate stiffness, a boxplot is presented to display the distribution of averaged strain values from different cells (nine nuclei volume-averaged strain in this graph). The orange line in the box indicates the mean value overs all nine cells.

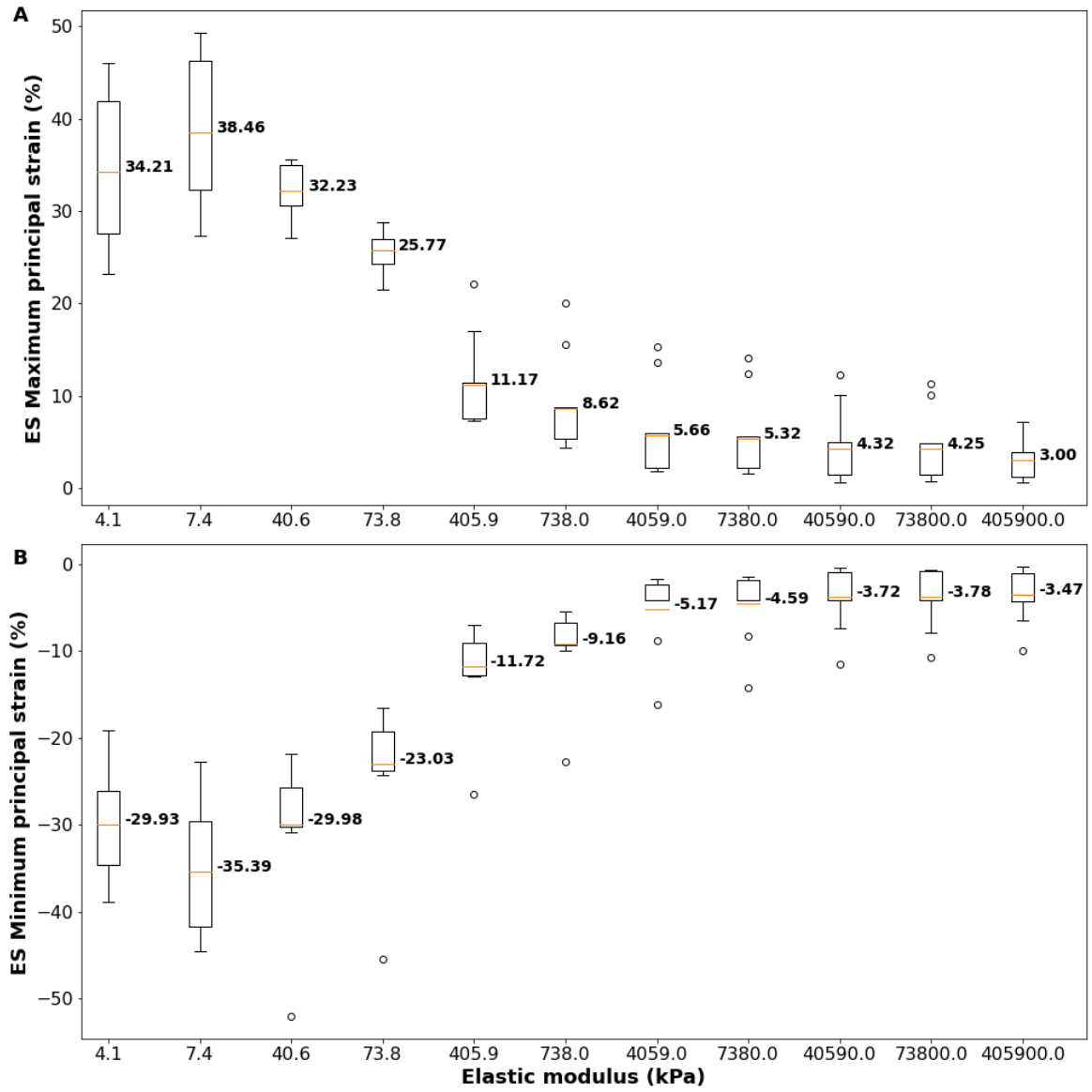

App Figure 8. End-systole nuclear deformation: maximum (A) and minimum (B) principal strain in the cell nucleus for different injectate stiffnesses (from 4.1 kPa to 405,900.0 kPa) in nuclei. For each value of injectate stiffness, a boxplot is presented to display the distribution of averaged strain values from different cells (nine nuclei volume-averaged strain in this graph). The orange line in the box indicates the mean value overs all nine cells.

App Table 9. Statistical analysis for cell components.

Parameters	**ED maximum principal strain**	**ED minimum principal strain**	**ES maximum principal strain**	**ES minimum principal strain**
Cytoplasm				
κ	24.73	25.37	78.73	77.69
p	0.0059	0.0047	8.92×10^{-13}	1.42×10^{-12}
Membrane				
κ	27.38	29.11	79.17	78.51
p	0.0022	0.0012	7.28×10^{-13}	9.81×10^{-13}
Nucleus				
κ	25.35	24.05	78.45	77.16
p	0.0047	0.0074	1.01×10^{-12}	1.85×10^{-12}

κ = chi-square value quantifying how different group of data are, p = p-value